UNIVERSITÁ DEGLI STUDI DI PALERMO

DIPARTIMENTO DI MECCANICA

MAPPING MULTIPLE RESIDUAL STRESS COMPONENTS USING THE CONTOUR METHOD AND SUPERPOSITION

Ph.D. thesis of:

PIERLUIGI PAGLIARO

February 2008

Scientific-disciplinary field: ING-IND/14

DOTTORATO DI RICERCA IN PROGETTAZIONE MECCANICA

XIX° CICLO - ANNO ACCADEMICO 2006-2007

UNIVERSITÁ DEGLI STUDI DI PALERMO

DIPARTIMENTO DI MECCANICA

MAPPING MULTIPLE RESIDUAL STRESS COMPONENTS USING THE CONTOUR METHOD AND SUPERPOSITION

by

PIERLUIGI PAGLIARO

Scientific-disciplinary field: ING-IND/14

A DISSERTATION SUBMITTED IN TOTAL FULFILMENT
OF THE REQUIREMENTS FOR THE DEGREE OF
DOCTOR OF PHILOSOPHY IN MECHANICAL DESIGN
XIX° CYCLE - ACADEMIC YEAR 2006-2007

PHD COORDINATOR:

Prof. Gabriele Virzì Mariotti

ADIVISORS:

Prof. Bernardo Zuccarello

Dr. Michael B. Prime

...To my Parents and my brother

Abstract

The Contour Method is a technique for measuring macroscopic residual stresses in engineering materials. In details, a body is carefully cut in two using wire electric discharge machining (EDM). The contours of the cut surfaces are then measured and used to calculate the original residual stress normal to the cut plane using a simple finite element calculation. In this study, two new theoretical developments of the contour method are presented which allows the measurement of multiple stress components respectively by applying different techniques and by making multiple cuts.

In order to to validate these new developments, a residual stress test specimen was designed, fabricated and then tested with different experimental techniques. A 60 mm diameter 10 mm thick disk was plastically compressed through the thickness with a 15 mm diameter indenter in the center of the disk to provide a unique biaxial stress state that is ideal for testing the theories. Two different materials were used for the specimens: a 316L stainless steel and an aluminium 2024-T351. The stresses in the 316L stainless steel specimen were first mapped using time-of-flight neutron diffraction. Next, the hoop stresses in both material disks were mapped on a cross-section using the classical contour method and furthermore measured with the slitting method, and the agreement with the neutron diffraction measurements and the FE prediction was excellent.

In order to validate the multiple techniques theory, an initial attempt to measure the in-plane stresses disk using x-ray diffraction was unsuccessful because of the large grain size of the 316L stainless steel. Then, several experimental tests on the 316L stainless steel and aluminium 2024-T351 indented disks were executed using the ESPI hole-drilling method.

The multiple cuts theory was demonstrated first by means of 3D FE simulations and then by an experimental test carried out on a quenched plate of HSLA-100 steel and on the 316L stainless steel disk. The surface superposition theory was demonstrated by using the ESPI hole drilling tests carried out on the 316L stainless steel and aluminium 2024-T351 indented disks.

Acknowledgements

I would like to thank some people that gave a contribution and support for the development of this thesis. My very first thanks go to my two advisors: Prof. Bernardo Zuccarello, who introduced me to the fascinating world of research during the development of my master degree thesis and gave me the possibility to go at the Los Alamos National Laboratory (LANL); and Dr. Michael B. Prime without whom this thesis would not exist, gave me the possibility to work at the LANL under his supervision for eighteen months and taught me how to develop my work in a "dynamic and constructive way, like everything in life should". Further, I am also thankful to him for all the things that he taught me and the way how he stimulate my work and our collaboration. Then, he gave me a great help during my staying in Los Alamos.

Also I would like to thank the University of Palermo that supported my studies with a fellowship and the Los Alamos National Laboratory, that even though I am not U.S. citizen, allow me to stay there to develop my thesis.

I would like to thank also some other people at the Los Alamos National Laboratory. First, Dr. Michael Steinzig, that was my co-host at LANL, who helped me in executing the ESPI hole drilling tests at Hytec, Inc. in Los Alamos. Dr. Bjørn Clausen with who I executed the neutron diffraction experiment at the Los Alamos Neutron Science Center (LANSCE). Mr. Manuel Lovato who executed all the mechanical tests on my samples (compression, cyclic and indentation tests) at the MST Division. Mr. Hunter Swenson for the great help in scanning some contours with the laser scan machine.

I would also thank Prof. Gary S. Schajer who hosted me at the Department of Mechanical Engineering, University of British Columbia, Vancouver, Canada, helping me to execute some ESPI hole drilling experiments. Further, he also gave me very nice suggestions and advices for my future. I am thankful also to Dr. Thomas R. Watkins at the Oak Ridge National Laboratory, Oak Ridge, USA, together with I executed the x-ray diffraction experiments. Then, Prof. Michael R. Hill at University of California-Davis and John VanDalen for scanning some contours with the laser scan machine at the Hill Engineering, LCC.

Many thanks to my colleagues at the Department of Mechanics in Palermo,

from whom I received invaluable guidance, knowledge, good advices and friendship and made the DIMA a nice place to work: Andrea Russo, Dr. Davide Tumino, Dr. Antonino M. Siddiolo, Dr. Giuseppe Pitarresi, and Michele Scafidi. For the same reasons I would like to thank my colleagues at LANL: Dr. Bartlomiej Benedikt, David Mascarenas, Dr. Tim Wong and Tim Overly.

My friends have been a great source of strength and motivation. I thank Ignazio Bumbolo, Gerry Immordino, Andrea Vaiana and Amy Bartlett.

In particular, I am deeply grateful to my parents and my brother. They supported me in a great way and always trusted every decision I made. Without their support, my thesis and everything I made would not exist.

Table of Contents

List of Figures

List of Tables

List of Symbols

A_j	coefficient for jth term in series expansion of stresses matrix size $nx1$	MPa	FL^{-2}
C	Hardening modulus	MPa	FL^{-2}
$C_j(a_i)$	calibration coefficient at $a = a_i$ for P_j, matrix size mxn	MPa^{-1}	$F^{-1}L^2$
F	Yield function	MPa	FL^{-2}
$P_j(x_i)$	jth term of series expansion evaluated at $x_i = a_i$, matrix size mxn		
Q	hardening material parameters	MPa	FL^{-2}
S	deviatoric stress	MPa	FL^{-2}
$[B]$	matrix that multiplies measured strains to determine $\{A\}$, matrix size nxm	MPa	FL^{-2}
Ω	Angle		
Θ	Angle		
α	Back-stress	MPa	FL^{-2}
α^{dev}	deviatoric back-stress	MPa	FL^{-2}
χ	Angle		
$\dot{\bar{\varepsilon}}^{pl}$	equivalent plastic strain rate	s^{-1}	T^{-1}
$\dot{\varepsilon}^{pl}$	rate of the plastic flow	s^{-1}	T^{-1}
γ	hardening material parameter		
ϕ	Angle		
σ^0	Size of yield surface	MPa	FL^{-2}
$\sigma^{(A)}$	Original residual stress	MPa	FL^{-2}
$\sigma^{(B)}$	Residual Stress after the cut	MPa	FL^{-2}
$\sigma^{(C)}$	Stress obtained applying the opposite contour	MPa	FL^{-2}
σ_0	yield stress at zero plastic strain	MPa	FL^{-2}
σ_θ	hoop stress	MPa	FL^{-2}

σ_r	radial stress	MPa	FL^{-2}
σ_z	axial stress	MPa	FL^{-2}
a	lattice parameter of the fcc crystal structure	mm	L
a_i	slit depth i, matrix size $mx1$	mm	L
b	hardening material parameters		

Chapter 1

Classical Contour Method

1.1 INTRODUCTION

Residual stresses play a significant role in many material failure processes like fatigue, fracture, stress corrosion cracking, buckling and distortion. Residual stresses are the stresses present in a part free from any external load, and they are generated by virtually any manufacturing process. Because of their important contribution to failure and their almost universal presence, the knowledge of residual stress is crucial for prediction of the strength of any engineering structure. However, the prediction of residual stresses is a very complex problem. In fact, the development of residual stress generally involves nonlinear material behavior, phase transformation, coupled mechanical and thermal problems and/or varying mechanical properties throughout the material. Hence, the ability to accurately quantify residual stresses through measurement is an important engineering tool.

Recently, a new method for measuring residual stress, the contour method [1, 2,3,4], has been introduced. In the contour method, a part is carefully cut in two along a flat plane causing the residual stress normal to the cut plane to relax. The contour of each of the opposing surfaces created by the cut is then measured. The deviation of the surface contours from planarity is assumed to be caused by elastic relaxation of residual stresses and is therefore used to calculate the original residual stresses. One of the unique strengths of this method is that it provides a full cross-sectional (two-dimensional) map of the residual stress component normal to the cross section. The only common methods that can measure similar 2-D stress maps have significant limitations [5]. The neutron diffraction method is nondestructive but sensitive to micro-structural changes [6], time consuming, and limited in maximum specimen size, about 50 mm, and minimum spatial resolution, about 1 mm. Sectioning methods [5] are experimentally cumbersome, analytically complex, error prone, and have limited spatial resolution, about 1 cm. Other relaxation methods,

at least those that are commonly used, determine at most a one-dimensional depth profile [7], although some can measure multiple stress components [8]. A limitation of the contour method is that only one residual stress component is determined from the measurement.

In order to extend the capability of contour method to measure multiple residual stress components, two new theoretical developments are presented in this thesis to obtain the other stress components. The first proposed method involves making multiple cuts and the original residual stresses, prior to the first cut, are reconstructed on all cut planes. Experimental test to validate the theory are presented. Multiple cuts have been used previously to measure multiple stress components with the contour method [9], but instead of reconstructing the original stresses the results were compared to finite element simulations of the manufacturing process where the effect of the multiple cuts were also simulated. Another approach for measuring multiple components with the contour method involves making additional cuts at 45 degrees from the first cut, assuming a continually processed part, and calculating the full original stress tensor on the first cut plane [10]. The method proposed in this thesis provides a complementary option for determining multiple stress components.

The second proposed method involves the application of other residual stress measurements techniques on the cut surface (i.e. after cutting) in order to measure the remaining in-plane stresses relaxed by the execution of the cut. Then the original residual stresses are reconstructed on the cut plane. Experimental tests were carried out in order to validate the theory.

These improvements to the contour method that needs experimental validation motivated to produce a novel test specimen. In literature there are many residual stress measurement techniques. Each of them has its advantages and disadvantages, and its own accuracy. As originally presented, the contour method only measured the stress component normal to the cross-section of measurement. More recent extensions to the contour method [10,11] determine multiple components using multiple cuts. However, in theory one should be able to measure multiple components with a single cut if subsequent measurements are taken on the cut surface with other techniques. A test specimen with significant stresses in two directions that were also significantly different from each other would provide the most convincing validation of the new theory. Since both the new theory and the independent validation would require other measurement methods, the specimen would have to be possible to measure with multiple techniques.

In order to test these new theories, in this thesis will be presented the design, the fabrication, the FE model and the experimental validation of a test specimen.

Most common residual stress test specimens are not ideal for the required validation purposes. Various procedure for introducing residual stresses into a test specimen have been used. The most common is a beam plastically bent producing a typical zigzag residual stress distribution through the thickness. The shrink-fit ring and plug that produced that exhibits a biaxial compression residual stress field on the plug and a tension-compression state on the ring. Unfortunately this specimen can not be used for contour method because the plug will full apart after the cut. Then, recently the side-punching technique [12] was used to introduce residual stresses into a specimen in order to study the influence of residual stress on fracture behavior of materials. A specimen with stresses that could be easily predicted or modeled would provide the additional benefit of not requiring extensive independent measurements. In order to produce a bi-axial residual stress field with different sign in the test specimen, a technique similar to the side-punching [12], that will easily allow to predict by FE simulation the residual stress field, is presented.

In order to validate two theories for extending the contour method to multiple stress components, this thesis presents the design, fabrication, the material characterization and the FE prediction of the residual stresses of the specimen described in the earlier paragraph. Furthermore, in order to measure the residual stress field produced with this technique, a neutron diffraction experiment was executed on this specimen. Then also the contour method was applied to two different test specimens, that have virtually the same residual stress field, and it was also possible to verify its good repeatability.

1.2 THEORY

The contour method for measuring residual stresses is based on a variation of Bueckners superposition principle [13]. Figure 1.1 presents an illustration in 2-D for simplicity, although the principle applies equally in 3-D. In A, one starts with the undisturbed part containing the residual stresses to be determined. In B, the part has been cut in two and has deformed because of the residual stresses released by the cut. In C, the free surface created by the cut is forced back to its original shape. Superimposing the stress state in B with the change in stress from C gives the original residual stresses throughout the part. This superposition principle assumes that the material behaves elastically during the relaxation of residual stress and that the material removal process does not introduce stresses of sufficient magnitude to affect the measured displacements.

Proper application of this superposition principle allows one to experimentally determine the residual stresses along the plane of the cut. Experimentally, the

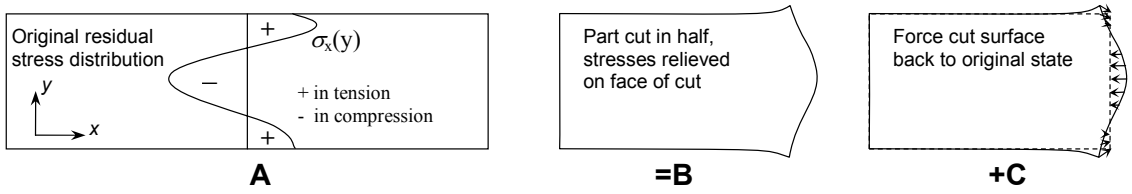

Figure 1.1 *– Superposition principle to calculate residual stresses from surface contour measured after cutting the part in two.*

contour of the free surface is measured after the cut. Analytically, the surface of a stress-free model is forced back to its original configuration as in step C. Because the stresses in B are unknown, one cannot obtain the original stresses throughout the body. However, the stresses normal to the free surfaces in B must be zero. Therefore, step C by itself will give the correct stresses along the plane of the cut.

The described superposition principle uniquely determines the original σ_x and τ_{xy} (and τ_{xz} in the 3-D case) residual stress distribution on the plane of the cut. The analytical solution, step C, specifies conditions on all boundaries of the body: displacements are specified on the cut plane, and the remaining boundaries are stress free. Also, the body forces are zero throughout the body. Therefore, by Kirchoffs boundary value theorem [14], the solution for the stress state in the elastic body is unique. Conversely, because Bueckners superposition principle tells us that the solution is correct, only one original distribution of σ_x, τ_{xy} and τ_{xz} cut plane can produce a given set of displacements on the boundaries. Bueckners superposition principle also tells us that the other residual stresses in the body away from the cut plane and the transverse stresses, σ_y, σ_z and τ_{yz}, on the cut plane will not change the deformations in the cut part, i.e., our measured contour in step B of Fig. 2.1. Therefore, these stresses will not cause errors in the contour method measurements, but the contour method will not uniquely determine these stresses. However, the analytical solution (step C Fig. 2.1) does uniquely and correctly determine the change in all the stresses throughout the part.

In practice, there is an arbitrary displacement in the contour measurement, i.e., the zero is arbitrary. There is also one arbitrary rotation in 2-D and two in 3-D. However, the apparently arbitrary motions can in fact be uniquely determined by the need for the residual stress distribution to satisfy force and moment equilibrium. Furthermore, an FE model used to solve for the stresses accounts for the arbitrary motions automatically, as will be demonstrated later.

1.2.1 Assumptions and approximations

The assumptions, mentioned above, that the relaxation of residual stresses occurs elastically and the cutting does not induce stresses are common to relaxation methods [15] and have been studied extensively [16,17]. However, the contour method requires one unfamiliar assumption: that the cut remove a constant width of material where the width is measured in the original undeformed material configuration, i.e. cutting method does not re-cut previously cut surfaces. Because the body will deform slightly as stresses are released during cutting, the validity of this assumption is not certain even if the cut is perfectly straight relative to a laboratory reference frame. In other words, the original plane of the cut may move during the cutting, and the cut may proceed on a different path. However, both the validation experiment and an FE simulation, which are discussed later, show that the flat cut assumption is reasonable if the specimen is constrained adequately during cutting. In fact, a symmetry argument shows that the plane will not move for a zero-width cut made in the center of a symmetrical clamping arrangement. For such a symmetric case, the only deviation from the flat cut assumption is caused by the finite width of the actual cut.

One approximation to the theory is made purely for convenience in the analysis: the deformed shape of the body is not modeled before analytically performing step C. The starting point for this step can be a flat surface because the deformations are quite small for engineering materials, and the analysis is linear. The results will be the same, and the analysis is simpler.

An important approximation limits the contour method to measurement of the normal stresses only and not the shear stresses. Measurement of the surface contour only provides information about the displacements in the normal (x) direction, not those in the transverse (y) direction. Therefore, the analytical approximation of step C will force the surface back to its original configuration in the x-direction only and the shear stress in the y-direction forced to zero on the cut plane. Elsewhere is free boundary ($\sigma = \tau = 0$). If the residual shear stresses were originally zero along the plane of the cut (τ_{xy} in Fig. , τ_{xz} also for the 3-D case), the approximation is exact: Poisson contractions will return the surface to its original y-position, and the calculated stresses will be correct.

In the general case when shear stresses are present on the cut plane, one need only average the contour measured on the two halves of the part to correctly determine the normal stress, σ_x. To explain this theoretically, recall that the deformations caused by the release of residual stresses can be evaluated by considering an equivalent surface traction on the cut plane. The normal traction T_x is symmetric with respect

to the cut plane, and the transverse traction T_y is antisymmetric. Therefore, because the problem is elastic and superposition holds, the average of the contours on the two surfaces will give the contour shape as if only the normal stresses were present.

Numerical simulations were executed in [1] to demonstrate that the above approximations are reasonable and that averaging correctly handles shear stresses.

1.3 EXPERIMENT

For the contour method, the ideal machining process for separating the part would make a precisely straight cut, would not remove any further material from already cut surfaces, and would not cause any plastic deformation. Wire electric discharge machining (wire EDM [18]) is probably the choice closest to the ideal. In wire EDM, a wire is electrically charged with respect to the workpiece, and spark erosion causes material removal. The cutting is non-contact, whereas conventional machining causes localized plastic deformation from the large contact forces. The part is submerged in temperature-controlled deionized water during cutting, which minimizes thermal deformations. The wire-control mechanisms can achieve positional precision of a fraction of a micrometer, especially for a straight cut. When the conditions are held constant during the cutting, wire EDM cuts with a constant overcut, which is also necessary to make a straight cut. Overcut means that the final slot is wider than the wire making the slot.

Usually a 100 μm diameter wire is used for contour method. Skim cut settings are used for better precision and a finer surface finish, and also to minimize any recast layer and cutting-induced stresses [18,19]. Including the overcut, the slot is about 150 μm wide.

As discussed in subsection 1.2.1, the original plane of the cut must be constrained from moving as stresses are relaxed during the cutting. Such constraint requires an unconventional clamping arrangement because usually only one side of the workpiece is clamped for wire EDM. Before clamping, the beam and all the clamps were allowed to come to thermal equilibrium in the water tank to assure that no thermal stresses would arise during the cutting.

After cutting, the part is removed from the clamps, and the contour of the cut surface are measured using a coordinate measuring machine (CMM) or a laser surface contouring. The CMM registers mechanical contact with a touch trigger probe. An optoelectric system using glass scales gives the probe location, which is combined with machine coordinates to locate the surface. Because the CMM uses a probe tip with a finite radius, surface roughness is at least partially filtered out from the measured contour. The laser scanning is a non-contact technique that allows

to acquire 3D objects as point clouds. It uses laser light to probe the environment. The laser beam shines on a surface and exploit a camera to look for the location of the laser dot. Depending on how far away the laser strikes a surface, the laser dot appears at different places in the cameras field of view. This technique is called triangulation because the laser dot, the camera and the laser emitter form a triangle. The length of one side of the triangle, the distance between the camera and the laser emitter is known. The angle of the laser emitter corner is also known. The angle of the camera corner can be determined by looking at the location of the laser dot in the cameras field of view. These three pieces of information fully determine the shape and size of the triangle and gives the location of the laser dot corner of the triangle. Usually the accuracy of laser scan is bigger than the CMM one.

The stresses that were originally present on the plane of the cut were calculated numerically by elastically deforming the cut surface into the opposite shape of the contour that was measured on the same surface. This was accomplished using a three-dimensional elastic finite element (FE) model. The contours must be measured on both halves of the part after cutting, and the results from the two sides should be averaged to minimize errors.

The contour method for measuring residual stress was experimentally validated several times. First using a bent beam specimen [1], then on a neutron diffraction scanned weld beam [2]. It was applied to a friction stir weld beam [20,21], a railroad rail [22] and to a LENS® component [23] and compared with neutron diffraction results Then it was also applied to an aluminum hand forging plate [9], to a quenched plate [24] and the same plate shot by a tungsten carbide sphere at high velocity [25].

In many ways, the contour method has the potential to surpass other measurement methods in both its ability to measure stresses and its ease of use:

1. The contour method can measure a full 2-D cross-sectional map of the residual stress component normal to the cross section.

2. The residual stress map can be obtained directly from the measured contour; no inverse procedure or assumptions about the stress variations are necessary.

3. The technique is relatively simple experimentally. No strain gages or other instrumentation are required during the testing. The necessary equipment is widely available in machine shops and inspection laboratories.

The contour method also has the potential to measure residual stress maps that are extremely difficult to measure with other techniques, if possible at all. One particularly promising application is welding residual stresses. Microstructural changes in the weld material make neutron diffraction measurements difficult but have relatively small effects on the macroscopic elastic properties that would affect contour

method measurements. Another exciting class of applications is parts with geometrically complex cross sections, like railroad rails, forging, I-beams, extrusions, and castings.

Chapter 2

Theory: Multiple Components

In this chapter two new theoretical developments that will allow the contour method to measure multiple stress components making different cuts or using different measurement techniques, are presented.

2.1 FIRST CUT: TRADITIONAL CONTOUR METHOD

Before introducing the new theory for multiple cuts, the original theory for the first cut is reviewed. The contour method [1,2] is based on a variation of Bueckner's superposition principle [13]. Figure 2.1 presents an illustration in 2-D for simplicity, although the principle applies equally in 3-D.

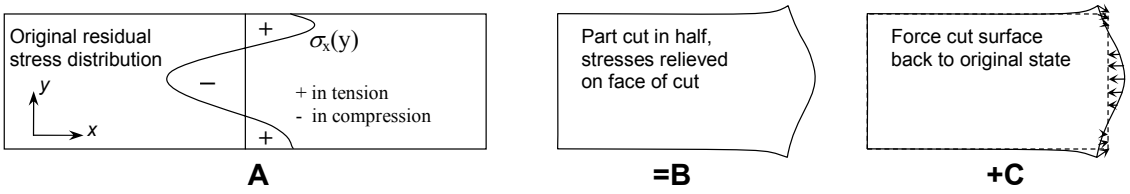

Figure 2.1 – *Superposition principle to calculate residual stresses from surface contour measured after cutting the part in two.*

In **A**, the part is in the undisturbed state containing the residual stress to be determined. In **B**, the part has been cut in two and has deformed because of the residual stresses released by the cut. In **C**, the free surface created by the cut is forced back to its original flat shape. Superimposing the stress state in **B** with the change in stress from **C** would give the original residual stress throughout the part, as shown by the following expression:

$$\sigma^{(A)} = \sigma^{(B)} + \sigma^{(C)} \tag{2.1}$$

This superposition principle assumes elastic relaxation of the material and that the cutting process does not introduce stress that could affect the measured contour.

With proper application of this principle it is possible to determine the residual stress over the plane of the cut. Experimentally, the contour of the free surface is measured after the cut and analytically the surface of a stress-free model is forced back to its original flat configuration by applying the opposite of the measured contour as displacements. Because the stresses in B are unknown, one cannot obtain the original stress throughout the body. However, the normal and shear stresses on the free surface in B must be zero (σ_x, τ_{xy} and τ_{xz}). Therefore, step C by itself will give the correct stresses along the plane of the cut:

$$\begin{aligned} \sigma_x^{(A)} &= \sigma_x^{(C)} \\ \tau_{xy}^{(A)} &= \tau_{xy}^{(C)} \quad at\ x = x\ cut\ surface \\ \tau_{xz}^{(A)} &= \tau_{xz}^{(C)} \end{aligned} \tag{2.2}$$

The described superposition principle uniquely determines the original σ_x, τ_{xy} and τ_{xz} residual stress distribution on the plane of the cut. In fact, the analytical solution (step C) specifies conditions on all boundaries of the body. In detail, displacements are specified on the cut plane, and the other surfaces are stress free. Therefore, by the Kirchoff's boundary value problem [14], the solution for the stress state in the elastic body is unique. Since the solution is unique and the application of the contour as boundary conditions gives us the original distribution of the σ_x, τ_{xy} and τ_{xz} on the cut plane, conversely the relaxed contour after the cut is only caused by the relaxation of the original σ_x, τ_{xy} and τ_{xz} on the cut plane. Stresses in the body away from the cut plane and the transverse stresses σ_y, σ_z and τ_{Yz} on the cut plane will not have any influence on the measured contour (step B). For this reason, step C does not determine the original value of these stresses throughout the body but only the change in all the stresses throughout the part.

In practice, only the normal stress component σ_x, can be experimentally determined. The experimental measurement of the contour only provides information about the displacements in the normal (x) direction, not those in the transverse (y) direction. Therefore, the surface is forced back to the original flat configuration (step C) in the x-direction only. The shear stresses τ_{xy} and τ_{xz} are constrained to zero in the solution. This stress-free constraint is automatically enforced in most implicit, structural, finite-element analyses if the transverse displacements are left unconstrained. Even if residual shear stresses were present on the cut plane, av-

eraging the contours measured on the two halves of part still lead to the correct determination of the normal stress σ_x [1].

A small convenience is taken in the data analysis by finite element modeling. Modeling the deformed shape of the part for step C in Figure 2.1 would be tedious. Instead, the surface is initially flat in the finite element model, and then the part is deformed into the shape opposite of the measured contour. Because the deformations are quite small, the same answer is obtained but with less effort.

2.2 SECOND CUTS

Once the original part has been cut in two and the original σ_x residual stress on the cut plane is obtained, it is also possible to evaluate the other original σ_z (or σ_y) residual stresses on a different plane by making additional cuts. The initial analysis of data from the additional cut provides a map of stresses after the first cut, which in the neighborhood of the first cut have changed from their original values. Fortunately, the same calculation that provides σ_x from the first cut also provides all the necessary information to reconstruct the original stresses on the plane of the second cut (before the first cut — step A in Figure 2.2).

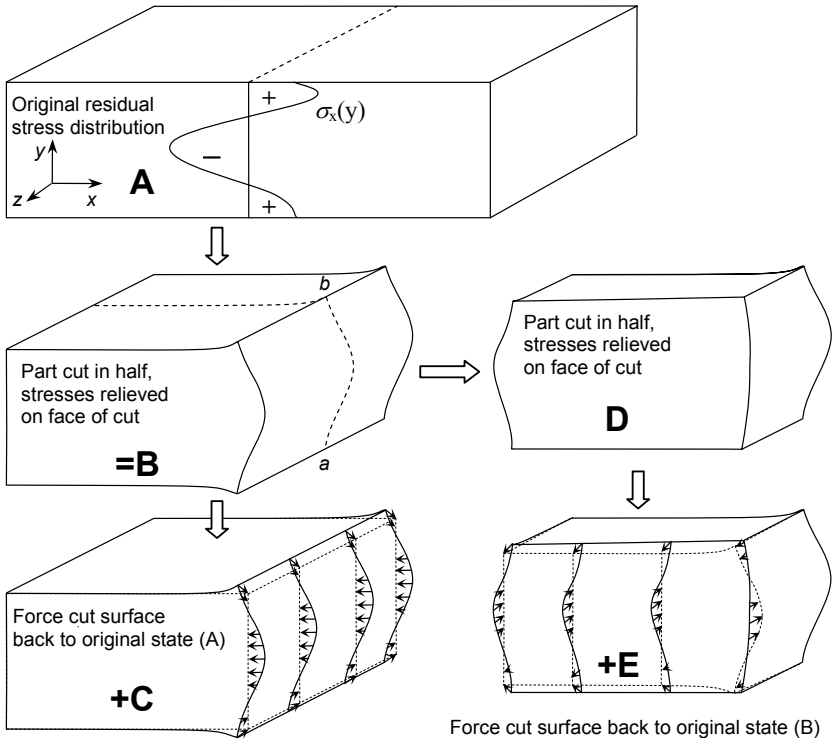

Figure 2.2 – *Multiple Stress-Component Superposition Principle.*

Figure 2.2 illustrates the theory for reconstructing the original residual stresses

on the plane of the second cut. The steps A, B and C are as described above for Figure 2.1. In D, the part has been cut another time in two along a plane perpendicular to the first cut plane and normal to the z-direction.

It has deformed because of the residual stresses released by the cut. In E, the free surface created by the second cut is forced back to the original shape before the second cut (step B). Since the stress state in B is given by superimposing the stress state in D with the change in stress from E (as described for the first cut), the original residual stress throughout the part in A, is given by the sum of the stress state in D, E and C, as shown by the following expression:

$$\sigma^{(A)} = \sigma^{(B)} + \sigma^{(C)} = \sigma^{(D)} + \sigma^{(E)} + \sigma^{(C)} \tag{2.3}$$

Because the stresses in D are unknown, for the same reason described above, one cannot obtain the original stress throughout the body. However, the normal and shear stresses on the free surface in D must be zero (σ_z, τ_{zx} and τ_{zy}). Therefore, the sum of step E, (equal to step B on the cut surface) and step C will give the correct stresses along the plane of the second cut:

$$\begin{aligned} \sigma_z^{(A)} &= \sigma_z^{(E)} + \sigma_z^{(C)} \\ \tau_{zx}^{(A)} &= \tau_{zx}^{(E)} + \tau_{zx}^{(C)} \\ \tau_{zy}^{(A)} &= \tau_{zy}^{(E)} + \tau_{zy}^{(C)} \end{aligned} \tag{2.4}$$

Obviously, as described before, the solution is unique, but only the normal stress component σ_z can be experimentally determined.

With this superposition principle, it possible to evaluate the σ_x and σ_z residual stresses respectively along two different cut planes. Since these two planes have a line in common ($a - b$ line in Figure 2.2), along this line the σ_x and σ_z stress distributions are both determined. Unfortunately, stresses on the edge of the cut are the most uncertain for the contour method, so this is not the best location to get accurate results.

The same procedure can be applied to obtain the σ_y component, if the cut was made along a plane normal to the y-direction instead to the z-direction, or it is also possible to cut in two the part in D and then apply another time the same superposition principle. In this way, it is possible to obtain the σ_x, σ_z and σ_y maps respectively along three perpendicular planes. Since these planes have one point in common, only at this point (the geometrical center of the plate) the three normal stress components σ_x, σ_z and σ_y are all determined.

2.2.1 Numerical verification

This section will demonstrate numerically that the multiple cuts correction can correctly determine the original stresses after multiple cuts. It will also check an important assumption about shear stresses. For the single cut contour method, averaging the two measured contours on the opposing surfaces created by the cut removes any shear stress errors in calculating normal stresses [1]. With multiple cuts, the other stress components calculated after the first cut are also used, and shear stresses may cause errors in those.

FE simulations were used to demonstrate the validity of multiple component theory from multiple cuts for the contour method. A 2 x 2 x 1 plate was modeled using the ABAQUS® commercial FE code [26] and 32 x 32 x 16 mesh of 20-noded quadratic shape function elements (C3D20), see Figure 2.3. The material behavior was isotropic and linear elastic with Poisson's ratio of 0.3. For residual stress normalized to give a peak value of unity, the elastic modulus was taken as 1000 to give $\sigma_{MAX}/E = 1000\ \mu\epsilon$, which is a typical magnitude for structural metals. Residual stresses were initialized using the user FORTRAN subroutine SIGINI (see Appendix A.1), and then one FE analysis step was performed to ensure initial equilibrium. To simulate cutting the part in two (step B in Figure 2.2), a second analysis step removed the elements on either half of the plate. To simulate the second cut (step D in Figure 2.2), a third analysis step removed the elements on either half of the remaining portion of the plate. All of these simulations were repeated removing the opposite elements in order to get the deformations on both surfaces created by each cut.

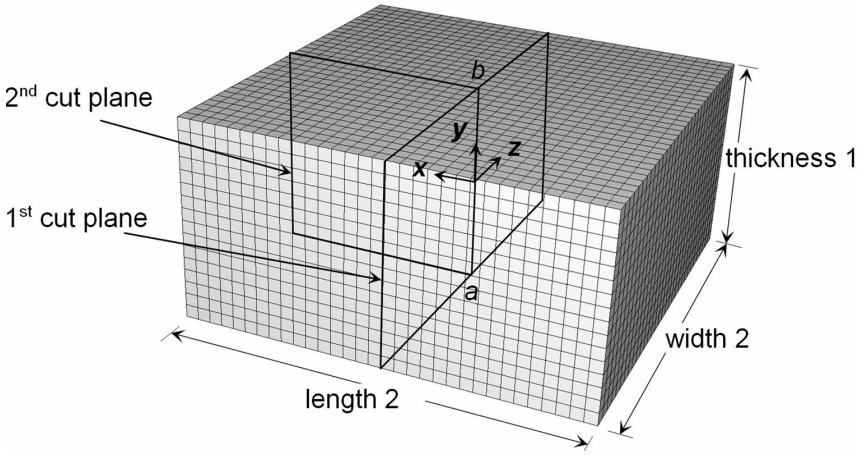

Figure 2.3 *– FE model of the plate used in the simulations of the multiple cut theory.*

The first simulation considered a plate having no shear stresses along the plane

of the first cut. The axial residual stress σ_x in the central 50 percent of the length of the plate were given by a simple parabolic distribution that satisfied equilibrium:

$$\sigma_x(y) = 6y^2 - 6y + 1 \tag{2.5}$$

where the plate thickness goes from $y = 0$ to 1. The stresses in the outer 25 percent of plate length on both ends differed from Eq. 2.5, and the stress σ_y, τ_{xy} are present in order to satisfy equilibrium and free boundary conditions. The normal stresses σ_z are zero everywhere, so it means that we have a plane stress state. This residual stress state is shown in Figure 2.4(a).

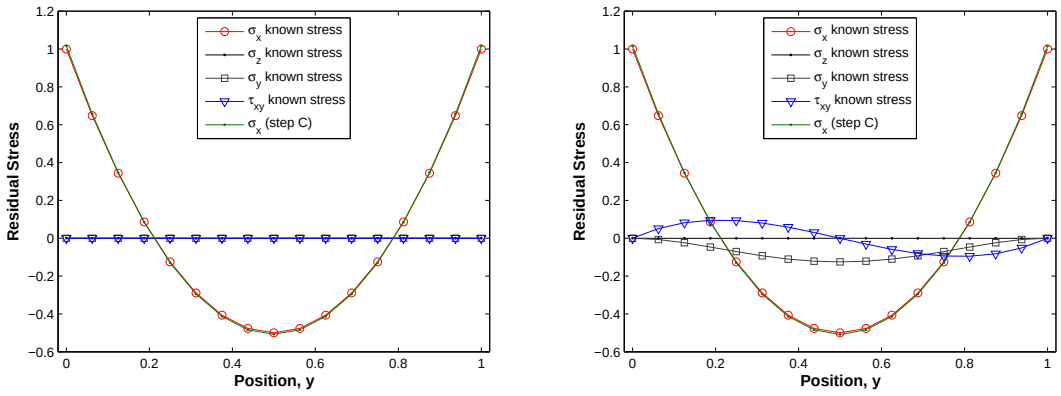

Figure 2.4 – *Simulated residual stress distribution along the first cut plane and comparison with the simulated contour measured x: (a) with no shear stresses and (b) with shear stresses on the first cut plane.*

To apply the superposition principle, a model of the undeformed and unstressed half of the plate was taken from the full mesh. The opposite of the average of the two contours of the relaxed surface created by the first cut (from the second step of the previous analysis) was applied as displacement boundary condition to the nodes along the first cut surface (step C in Figure 2.2). In a second step analysis, only a quarter of the original plate was considered (by removing the elements) and the opposite of the average of the two contours of the relaxed surface created by the second cut (from the third step of the previous analysis) was applied as displacement boundary condition to the nodes along the second cut surface (step E in Figure 2.2). The first step provided as results the original residual stress component σ_x on the first cut surface and also the changes in the other components (σ_z, σ_y, τ_{xy}, τ_{xz} and τ_{yz}) (step C in Figure 2.2). The second step provided the post-relaxation residual stress component σ_z (relaxed by the first cut) on the second cut surface (step E in Figure 2.2). A simple summation of the change of σ_z and the post-relaxation σ_z

gives the original residual stress component σ_z on the second cut plane, as described by Eq. 2.4.

Figure 2.4(a) shows the first cut results on line $a-b$ in Figure 2.3 for case of no shear stresses on the first cut plane. Figure 2.4(b) shows the results with shear stresses, which will be detailed later in this section. As previously shown [1], the normal stresses σ_x are correctly determined in either case.

Figure 2.5 shows the result of the multiple cuts contour method simulation for no shear stresses on the first cut plane. Figure 2.5(a) shows the stress along the through-thickness direction on the center of the plate (line $a-b$ in Figure 2.3). The reconstructed stresses (red line) match with the original residual stress (black line). Figure 2.5(b) shows the stress along the mid-thickness line on the second cut plane. Also in this case the reconstructed and the original stress match very well. This first simulation confirmed that the multiple cuts theory for multiple components is correct in the case of absence of shear stresses in the first cut plane. Since in this case no shear stress are present, the change of the σ_z obtained from the step C in Figure 2.2 is only related to the relaxation of the σ_x, so the FE simulation gives the right reconstructed stresses.

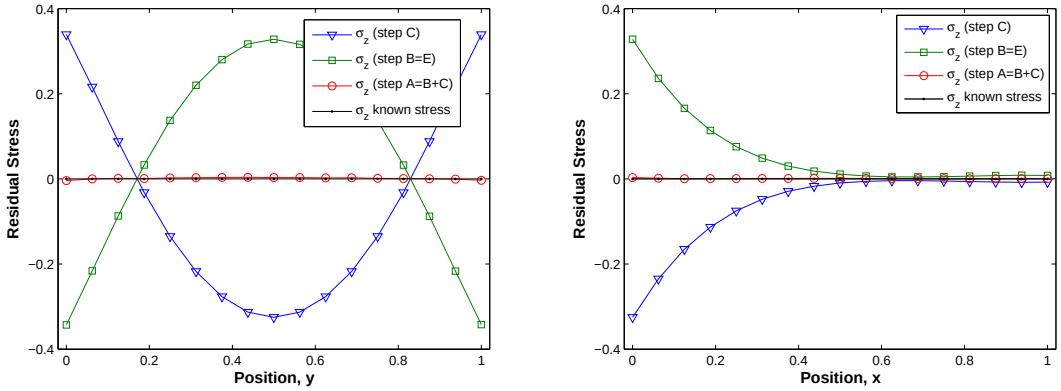

(a) (b)

Figure 2.5 – *Simulated multiple cuts contour method results for plate with no shear stress on the first cut plane: (a) residual stress reconstruction along the through-thickness direction (line $a-b$ in Figure 2.3); (b) reconstruction along the mid-thickness line ($x=0$ center of the plane).*

The second simulation considered a plate with both shear and normal stresses along the plane of the first cut. The normal stresses σ_x along the plane of the first cut were still given by Eq. 2.5, while the shear stresses τ_{xy} and the normal stresses σ_y, that satisfy the equilibrium equations, are given by:

$$\tau_{xy}(y) = 2y^3 - 3y^2 + y \tag{2.6}$$

$$\sigma_y(y) = -\frac{y^4}{2} + y^3 - \frac{y^2}{2} \tag{2.7}$$

The residual stress distribution on the first cut plane is shown in Figure 2.4(b). As before, we have a plane stress state.

Figure 2.6 shows the results of the simulated multiple cuts contour method with shear stress on the first cut plane. Figure 2.6(a) and Figure 2.6(b) show respectively the stress along the through-thickness direction on the center of the plate (line $a-b$ in Figure 2.3) and along the mid-thickness line on the second cut plane. In this case the reconstructed stresses (red line) do not match with the original residual stress (black line). The errors are relatively small, peaking about about 6% of the peak stresses in the problem. In the presence of shear stress on the first cut plane, the multiple cuts contour method gives small errors because the calculated change in σ_z along the second cut plane obtained from step C (blue line in Figure 2.6(a)) are only related to the relaxation of the σ_x on the first cut plane and not to the shear stresses τ_{xy} that also relaxed on that surface. To overcome this limitation, it would be necessary to apply the transverse displacements as BC's, but it is currently no experimentally possible to measure them. Going far from the first cut plane ($x > 0.4$ in Figure 2.6(b)) the mismatch become smaller until the reconstructed and the known stresses match exactly because those stresses were not changed significantly by the first cut.

The presence of shear stresses on the second cut plane before executing the second cut does not affect the result because the contour of the resulting cut surfaces are averaged and their effect is eliminated, as described in the Section 2.1.

2.3 SURFACE SUPERPOSITION

Once the part has been cut in two and the original σ_x residual stress on the cut plane is obtained, it is also possible to determine the other original residual stresses on same cut plane ($\sigma_y^{(A)}$, $\sigma_z^{(A)}$ and $\tau_{yz}^{(A)}$). The same finite element calculation that determines the original $\sigma_x^{(C)}$ residual stress in the cut plane also determines how much the in-plane stress components on the cut plane were changed by the relaxation from the cut, $\sigma_y^{(C)}$, $\sigma_z^{(C)}$ and $\tau_{yz}^{(C)}$. After the cut, the post-relaxation in-plane stresses ($\sigma_y^{(B)}$, $\sigma_z^{(B)}$ and $\tau_{yz}^{(B)}$) can be measured by a surface technique such as x-ray diffraction or hole drilling, see Figure 2.2, after electrochemical removal of material affected by the cut process (EDM affected layer [27]). A simple summation with the results of the

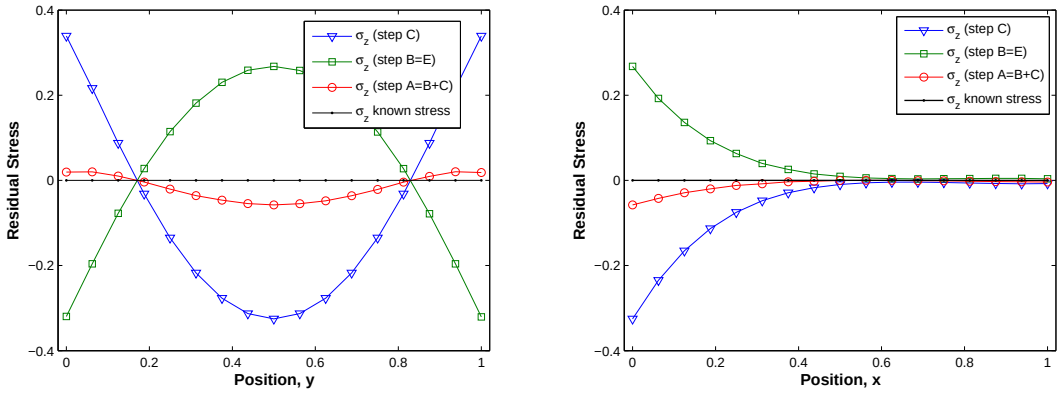

(a) (b)

Figure 2.6 – *Simulated multiple cuts contour method results for plate with shear stress on the first cut plane: (a) residual stress reconstruction along the through-thickness direction (line $a - b$ in Figure 2.3); (b) reconstruction along the mid-thickness line ($x = 0$ center of the plane).*

previous finite element calculation (Eq. 2.1) then provides the original components of the residual stress on the plane that was cut.

$$\begin{aligned} \sigma_y^{(A)} &= \sigma_y^{(B)} + \sigma_y^{(C)} \\ \sigma_z^{(A)} &= \sigma_z^{(B)} + \sigma_z^{(C)} \\ \tau_{yz}^{(A)} &= \tau_{yz}^{(B)} + \tau_{yz}^{(C)} \end{aligned} \tag{2.8}$$

This theory work only in case of no shear stress in the plane of the cut. In fact, the execution of the cut produce the total relaxation of the stresses, σ_x, τ_{xy} and τ_{xz}, on the cut plane. The change in the other stress components is affected by all these stress relaxations. In order to overcome this limitation, it is needed to measure the stresses on both halves of the part after the cut and averaging them. then the surface superposition can be applied considering the average stress for the step B. In this way the correct result will be obtained.

2.3.1 Numerical verification

This section will demonstrate numerically that the surface superposition can correctly determine the other original stress components by applying different techniques.

The same FE simulations described in Subsection 2.2.1 were used to demonstrate the validity of surface superposition theory for the contour method and its limitations. Both case, no shear stress and with shear stress on the cut plane, were

considered. After the second step analysis the residual stresses normal to the cut plane are relaxed by the cut (first cut plane on Figure 2.3). Because of that the other stress components, σ_z, σ_y, τ_{xy}, τ_{xz} and τ_{yz}, change in order to satisfy the equilibrium equations near the cut plane. Those stress components that are not equal to zero on the cut plane, i.e. σ_z, σ_y and τ_{yz}, can be measured on the cut plane by a surface technique as x-ray diffraction or hole-drilling method. By superimposing these stress components with the change of the same stress components obtained by the half plate simulation, i.e. the simulation of the contour method, the original residual stress components σ_z, σ_y and τ_{yz} are obtained.

Figure 2.7 shows the result of the surface superposition with no shear stresses on the cut plane. Figure 2.7(a) and 2.7(b) show the σ_z and σ_y stress component respectively along the through-thickness direction on the center of the plate (line $a-b$ in Figure 2.3). The reconstructed stresses (red lines) match with the original residual stresses (black lines). The shear stress τ_{yz} are not plotted because they are always zero. So, this results confirmed that the surface superposition theory is correct in the case of absence of shear stresses in the cut plane. Since in this case no shear stress are present, the change of the σ_z and σ_y obtained from the step C in Figure 2.2 is only related to the relaxation of the σ_x, so the FE simulation gives the right reconstructed stresses.

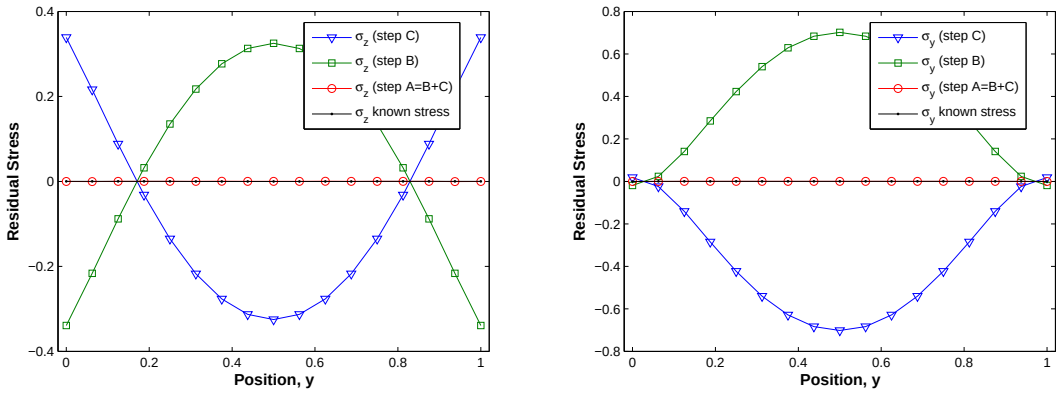

(a) (b)

Figure 2.7 – *Simulated surface superposition results for plate with no shear stress on the cut plane: reconstruction along the through-thickness direction (line $a-b$ in Figure 2.3) of the (a) σ_z and (b) σ_y respectively.*

Figure 2.8 shows the results of the simulated surface superposition theory with shear stress on the cut plane. Figure 2.8(a) and Figure 2.8(b) show the σ_z and σ_y stresses respectively along the through-thickness direction on the center of the plate (line $a-b$ in Figure 2.3). The shear stresses τ_{yz} are not plotted because are always zero. In this case the reconstructed stresses (red lines) do not match with the original

residual stresses (black lines). By averaging the remaining stresses obtained from the two halves of the plate and superimposing with the change of the same stress component obtained from the contour method simulation (Step C) it is possible to obtain the right answer (brown lines).

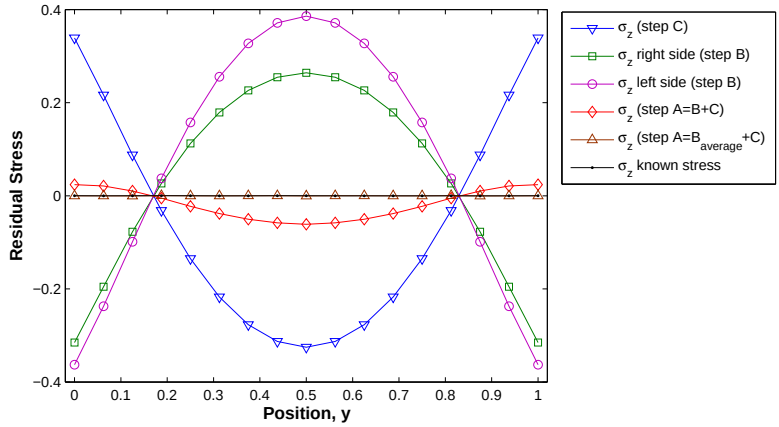

(a)

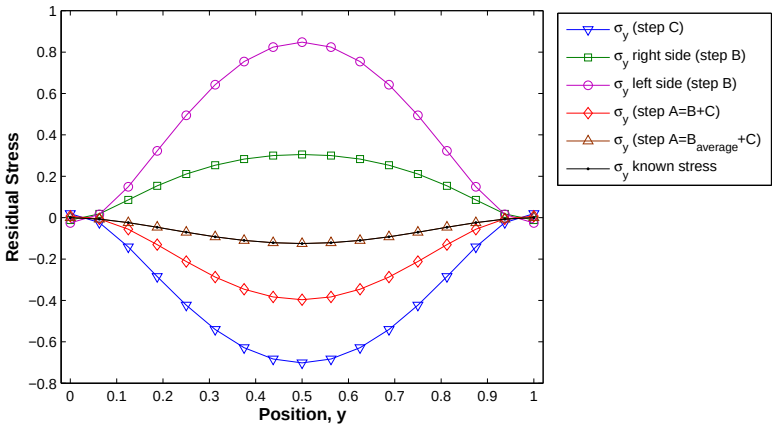

(b)

Figure 2.8 – *Simulated surface superposition results for plate with shear stress on the cut plane: reconstruction along the through-thickness direction (line $a - b$ in Figure 2.3) of the (a) σ_z and (b) σ_y respectively.*

Chapter 3

Residual Stress Specimen

3.1 INTRODUCTION

In order to validate the theoretical development, a test specimen was designed to provide a residual stress distribution particularly well suited for this purpose. It was desired to test the contour method on different stress states where the two significant normal stress components were approximately equal (i.e., equi-biaxial) and, conversely, of opposite sign. Such a stress state can be produced in a shrink-fit ring and plug, in which the expansion of a cooled, oversized plug is constrained by a surrounding ring resulting in biaxial compressive residual stresses in the plug. The ring experiences compressive radial stresses under the forces from the plug, but the hoop stresses are tensile. However, since a real ring and plug would fall apart during contour method cutting, an alternative configuration to produce a similar residual stress distribution was used.

3.2 DESIGN

A circular disk was plastically compressed through the thickness by two cylindrical indenters of smaller diameter [12], see Figure 3.1(a). The compressed region between the two indenters yields and wants to expand in the radial direction due to the Poisson effect. Under the constraint of the surrounding material, analogous to the ring in the example of a shrink-fit ring and plug, a biaxial (hoop and radial) compressive residual stress state is produced in the central region, while in the outer region there will be a tensile and compressive residual stress state for hoop and radial stresses, respectively (see Figure 3.1(b)).

The geometry of the specimen was then designed considering the constitutive behavior and experimental limitations. A 60 mm diameter 10 mm thick disk was chosen with the indenters 15 mm in diameter, see Figure 3.2. The thickness was chosen based on the limited penetration of neutrons through steel, while the di-

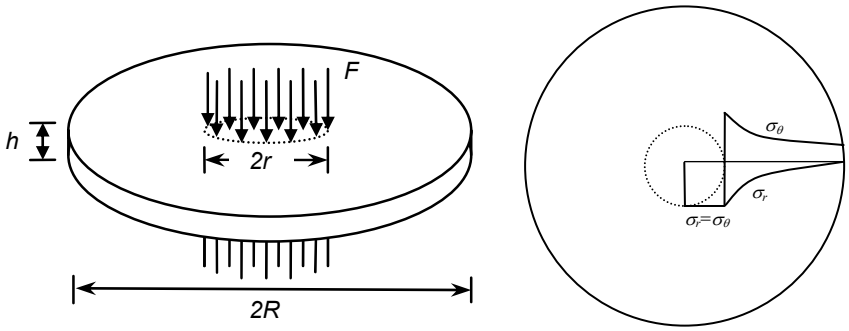

(a) (b)

Figure 3.1 *– Schematic diagram illustrating (a) the indentation process, (b) the ideal residual stress distribution obtained.*

ameters of the disk and the indenters were chosen to obtain stress gradients that could be resolved using reasonable neutron sampling volumes, to obtain a relaxed contour of at least 20 μm (peak-to-valley) and also considering the maximum load of the test machine. The indenters were also designed by means of several finite element simulations in order to minimize the stress concentrations, since there are some fillet radii. The indenter material used was an A2 tool steel, characterized by a high hardness (64 HRC) and a high yield stress (about 1300 MPa). The Young modulus of A2 tool is 204 GPa with a Poisson's ratio of 0.3. In order to center the two indenters with respect to the disk, two PMMA rings were designed (see Figure 3.2), which are moved out of the way prior to indentation.

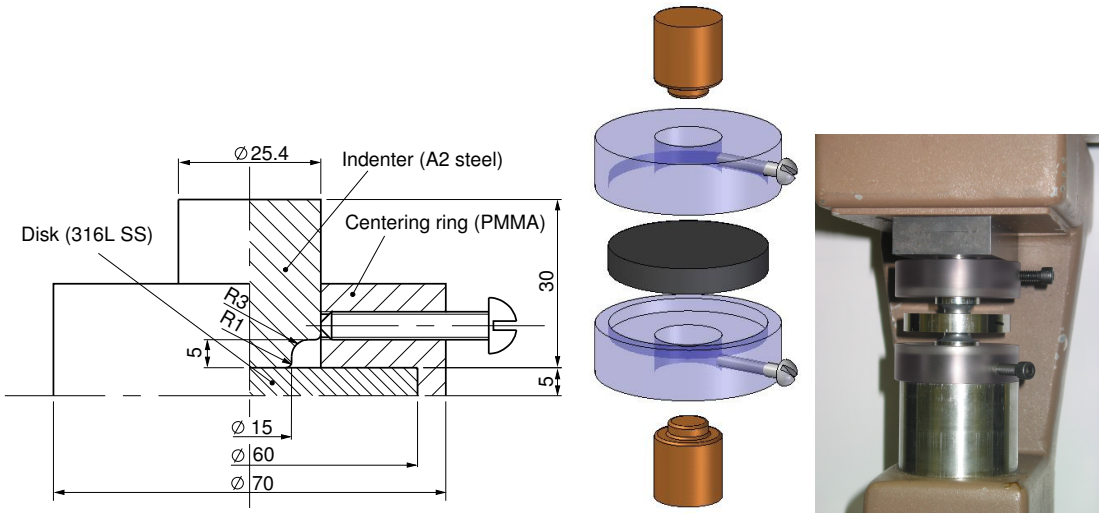

(a) (b) (c)

Figure 3.2 *– Design of the indentation fixture and photo of the indentation fixture and specimen in the load frame.*

3.3 MATERIALS

3.3.1 316L Stainless Steel

A 316L stainless steel was chosen for the material as the best compromise among the ideal materials for the different measurement methods that will be required to validate the multiple stress component theories. For the contour method, hole drilling, and other relaxation methods, it is generally better to have a material with high S_y/E in order to obtain a more relaxation. In general, the material yield strength, S_y, limits the residual stress magnitudes. An aluminum alloy would be a good choice (S_y/E can easily exceed 4000 $\mu\varepsilon$), but unfortunately, it is not as good for x-ray diffraction measurements. Austenitic steel has a lower S_y/E ($\approx$ 950 $\mu\varepsilon$), which means lower relaxed strains, but it is very good for neutron diffraction and x-ray diffraction. 316L stainless steel was chosen based on previous successful diffraction measurements and industrial importance. The disk was machined from a hot cross-rolled plate (457 mm x 457 mm and 12.7 mm thickness) of 316L stainless steel. The chemical composition of the 316L stainless steel is in weight percent is shown in Table 3.1 (in accord with the ASTM A240 and ASME SA-240).

Table 3.1 – *Alloying elements of 316L stainless steel plate in weight-% in accord with the ASTM A240 and ASME SA-240*

C	Mn	P	S	Si	Ni	Cr	Mo	N	Fe
0.018	1.59	0.031	0.005	0.23	10.64	16.65	2.16	0.05	balance

To measure the residual stress produced only by indentation, the material must be stress-free. For this reason, the plate was annealed at 1050 °C for 30 minutes in vacuum and then cooled to room temperature in argon in order to remove any preexisting residual stresses. After annealing, a metallographic analysis was made on the plate to check the grain-size (see Figure 3.3), whose average is about 50-100 μm, with some smaller grains. The metallography also revealed the presence of about 0.5% of ferrite, seen as dark stringers, which is not enough to cause any multi-phase problems with the neutron diffraction measurements of residual strains. A small amount of ferrite is typical in 316L stainless.

3.3.1.1 Stress-Strain curve

Constitutive data was required in order to model the material response during the indentation process. For this reason several compression tests, in accord with ASTM standard, were carried out in order to test the mechanical behavior of the material in the through-thickness direction and in the two in-plane directions. Cylindrical

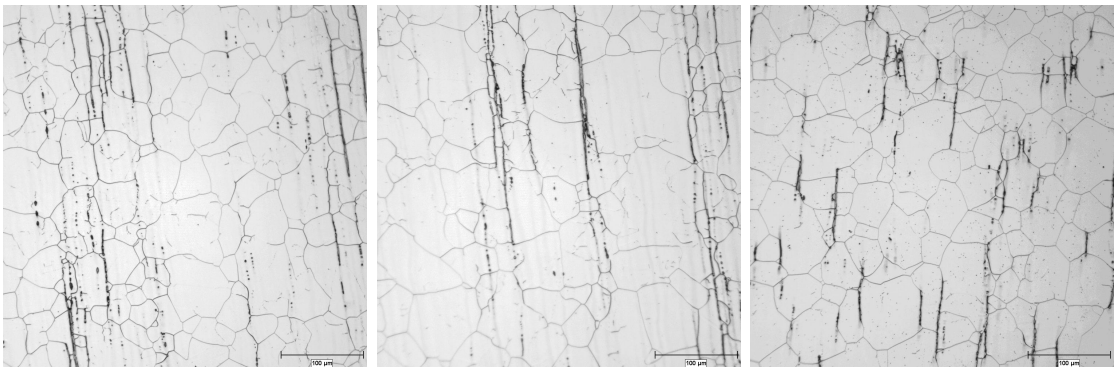

(a) (b) (c)

Figure 3.3 – *Metallography of the 316L plate after annealing. The scale bar is 100 μm long.*

specimens, 9.5 mm in diameter and 12.7 mm height, were extracted from the plate. Displacement-control compression tests with a crosshead speed of 0.046 mm/min were executed until ∼20% of engineering strain and then unloaded. The rate was chosen to give approximately the same strain rate as the one expected during the specimen indentation ($\dot{\varepsilon} = 5 \cdot 10^{-5}$ sec^{-1} after correcting for machine compliance). Figure 3.4 shows the true stress - true strain curves for the three tested material directions. The three curves are very close. Considering that except for very localized regions at the indenter edge, the plastic strains from indentation are less than 2%, the material is taken as behaving isotropically. From the slope of the linear part (unloading) of these curves the Young's modulus, E, was found to be 193 GPa while the yield stress S_y is 208 MPa (0.2% offset yield strength). The linear part of the curve during loading gave a Young's modulus lower than the expected value for this steel. However, after few consecutive load-unload cycles in the elastic range, the linear loading curve rose to the expected value. Probably, the annealing process resulted is some plasticity at very low loads.

Although not originally planned, cyclic stress-strain curves were also measured in order to accurately model the specimens. Preliminary FE simulation of the indentation process showed that the predicted residual stress field is affected, besides by the plastic behavior during loading, also by the hardening model for unloading. In fact, the 316L stainless steel exhibits a strong Bauschinger effect [28,29], and, furthermore, the indentation process produces some reverse loading in the central region. So, in order to calibrate a hardening model for the FE simulation, cyclic compression and tension tests were performed. Two specimen were extracted from each in-plane material direction of the 316L stainless steel plate. The specimens were 69.85 mm long, diameter of 5.08 mm and a gage length of 15.24 mm with

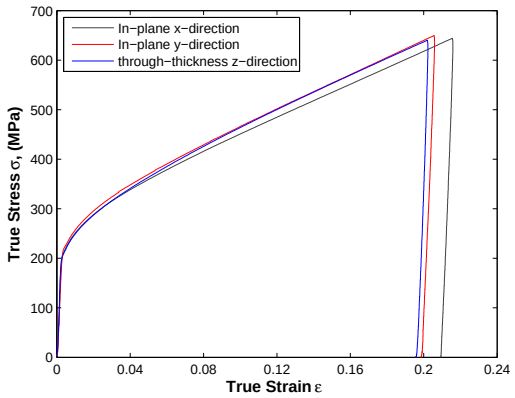

Figure 3.4 – *Stress - true strain curves of uniaxial compression tests for the 316L stainless steel.*

threaded ends. Because of the small plate thickness, no cyclic specimens were made in the through-thickness direction. Because of the small plate thickness, no cyclic specimens were made in the through-thickness direction. Since the preliminary FE simulations showed that the maximum equivalent plastic strain in the central region of the disk under the indenters was approximately of 2%, symmetric controlled strain cyclic tests were executed with a strain range, $\Delta\varepsilon$, of 4% (i.e. maximum strain of 2%). A strain rate of 4.5×10^{-5} sec^{-1} was used, that is the same that occurs in most part of the disk during the indentation. The true stress - true strain curve of one cyclic test is shown in Figure 3.5 together with the FE isotropic, kinematic and combined hardening model that were calibrated on this test and described in Chapter 4. There was no significant difference in the cyclic test in the other in-plane direction.

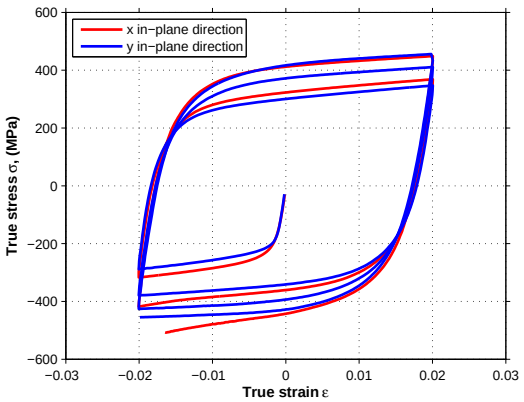

Figure 3.5 – *Cyclic behavior of the 316L in a uniaxial compression and tension test.*

3.3.1.2 Slitting test

In order to verify the absence of any preexisting residual stresses, a slitting method tests [30] was executed. A square specimen (60 mm x 60 mm x 12.7 mm) was extracted from the annealed plate and was instrumented with two strain gages type CEA-09-032UW-120, aligned along the rolling x-direction on the bottom surface. The cut was executed starting from the opposite surface (top) in 0.38 mm increments to a depth of 12.57 mm, using a EDM machine with a 250 μm brass wire (see Figure 3.6). The original residual stress were determined from the measured strains using the regularized pulse method [31]. The resulting stresses were lower than 10 MPa, confirming the effectiveness of the annealing process.

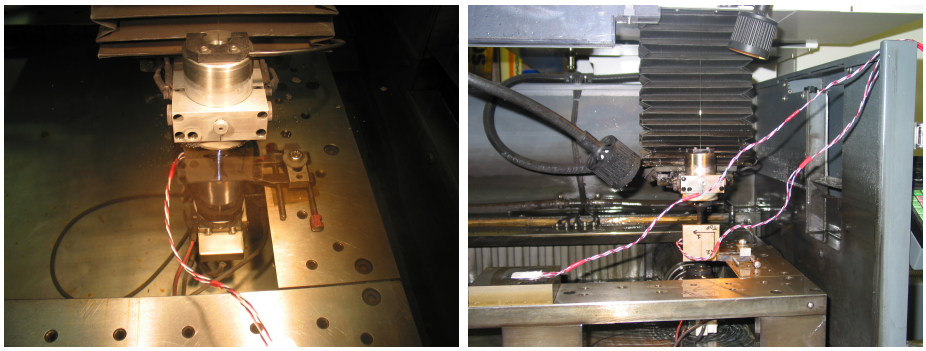

(a) (b)

Figure 3.6 – *Slitting test: (a) cutting process and (b) EDM machine and clamping fixture*

3.3.2 Aluminum 2024-T351

Since the execution of some ESPI hole-drilling tests were originally planned in order to validate the surface superposition theory, a material well suited for this purpose was chosen. In detail, an aluminum 2024-T351 was chosen for the high value of the ratio σ_y/E ($\approx$ 4300 $\mu\epsilon$), that means to have a high relaxation that it is a good advantage for the application of the contour method and hole-drilling method. Aluminum 2024-T351 is used for aircraft fittings, gears and shafts, bolts, pistons, rectifier parts, worm gears, fastening devices, veterinary and orthopedic equipment, structures.

Ten disks were machined from a rolled square plate (304.8 mm x 304.8 mm and 12.7 mm thickness) of 2024-T351 aluminium were machined ten disks. The chemical composition in weight percent of the aluminum 2024-T351 used in this study is showed in Table 3.2 (in accord with the ASME SB-211).

Table 3.2 – *Alloying elements of Aluminum 2024-T351 plate in weight-% in accord with the ASME SB-211*

Cr	Cu	Fe	Mg	Mn	Si	Ti	Zn	Al
0.1	3.8	0.5	1.2	0.3	0.5	0.15	0.25	balance

3.3.2.1 Stress-Strain curve

The same experimental program that was described before (see previous subsection) was carried out. The compression tests, in accord with ASTM standard, were carried out in order to test the mechanical behavior of the material in the through-thickness direction and in the two in-plane directions as described in the. Three cylindrical specimens, 9.5 mm in diameter and 12.7 mm height, were extracted from the plate. Displacement-control compression tests with a crosshead speed of 0.045 mm/min were executed until ∼20% of engineering strain and then unloaded. The rate was chosen to give approximately the same strain rate as was expected during the specimen indentation. Figure 3.7 shows the true stress - true strain curves for the three tested material directions. From the slope of the linear part (loading) of these curves the Young's modulus, E, was found to be 73.2 GPa while the yield stress σ_y is 328 MPa along the in-plane x-direction and the through thickness direction, while in along the in-plane y-direction σ_y was 282 MPa.

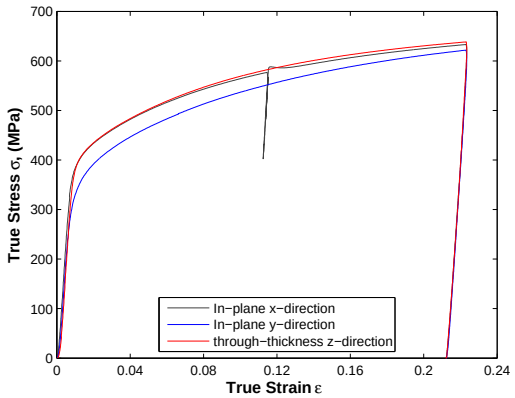

Figure 3.7 – *Stress - true strain curves of uniaxial compression tests for the aluminum 2024-T351.*

As described before, in order to calibrate a hardening model for the FE simulation, several cyclic uniaxial compression and tension test were executed. Two specimens were extracted from each in-plane material direction of the 316L stainless steel plate. The specimens were 69.85 mm long, diameter of 5.08 mm and a gage length of 15.24 mm with threaded ends. Since the preliminary FE simulations showed that the maximum equivalent strain in the central region of the disk was

approximately of 2%, symmetric controlled strain cyclic tests were executed with a strain range, $\Delta\epsilon$, of 4% (i.e. maximum strain of 2%). A strain rate of 4.5×10^{-5} sec^{-1} was used, that is the same that occurs in most part of the disk during the indentation. The true stress - true strain curves of the cyclic tests executed are shown in Figure 3.8.

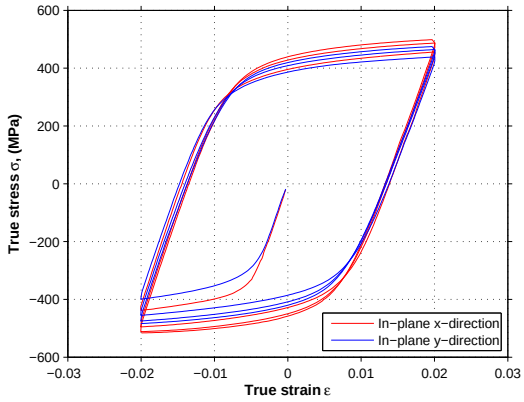

Figure 3.8 – *Cyclic behavior of the aluminum 2024-T351 in a uniaxial compression and tension test in the two in-plane directions.*

3.3.2.2 Slitting test

Two slitting method tests [30] were executed to measure the as received stresses in both in-plane directions for the 2024-T351 Aluminum plate. Two square specimens (60 mm x 60 mm x 12.7 mm) were extracted from the plate and each were instrumented with two strain gages type CEA-13-062UW-350, aligned along the in-plane x-direction and the in-plane y-direction respectively, both on the bottom surface. The cut was executed starting from the opposite surface (top) in 0.254 mm increments to a depth of 9.652 mm, using a EDM machine with a 250 μm brass wire (see Figure 3.6). The resulting stresses were lower than 10 MPa in both directions.

3.4 INDENTATION TESTS

Several disks of both, the 316L stainless steel and the 2024-T351 aluminium, were indented in the same experimental condition in order to virtually get the same residual stress field. The details of the various tests are reported in subsequent sections.

3.4.1 316L SS disks

The specimen was indented to a peak load of 90 kN under displacement control using a crosshead speed of 0.15 mm/min. A MOLYCOTE® anti-friction coating was applied on the contact surfaces of the two indenters. Since the displacement measurement (blue curve in Figure 3.10) is affected by the compliance of the specimen, the indenters, the lubricant and part of the test machine, due to the position of the sensor (see Figure 3.9), three preliminary tests without any specimen (indenter versus indenter) were executed to the same maximum load to measure the in series compliance of the indenters-lubricant-test machine (green curve in Figure 3.10) and also to eliminate some hysteresis effect. Then the indentation of two disk were executed and a footprint in both side of the disks was produced with a thickness reduction of -0.85%. Another indenter-indenter test was executed after the indentation of the two disks in order to check possible changes. By subtracting the measured displacements of the two tests, the displacements at the indenter-specimen interface were obtained (red curve in Figure 3.10). In the Figure it is also plotted the FE prediction of the indentation process that will be described in the next Section.

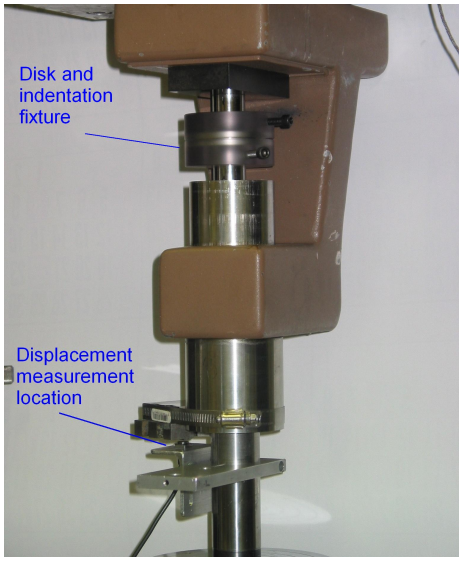

Figure 3.9 – *Indentation fixture and displacement measurement location*

3.4.2 Aluminum 2024-T351 disks

The specimen was indented to a peak load of 99.6 kN under displacement control using a crosshead speed of 0.14 mm/min. A MOLYCOTE® anti-friction coating was applied on the contact surfaces of the two indenters. Since the displacement measurement (blue curve in Figure 3.11) is affected by the compliance of the speci-

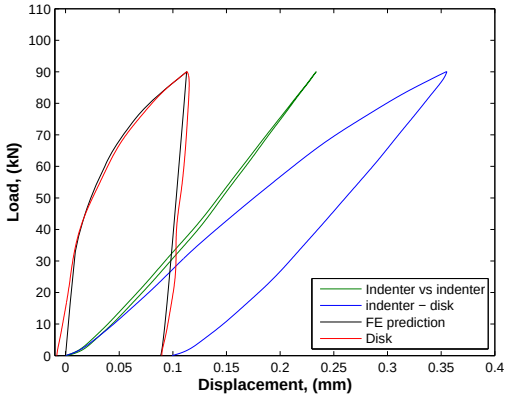

Figure 3.10 – *Load - displacement curves of the indentation process and FE prediction for the 316L SS disk.*

men, the indenters, the lubricant and part of the test machine, due to the position of the sensor (see Figure 3.9), three preliminary tests without any specimen (indenter versus indenter) were executed to the same maximum load to measure the in series compliance of the indenters-lubricant-test machine (green curve in Figure 3.11) and also to eliminate some hysteresis effect. Then the indentation of two disk were executed and a footprint in both side of the disks was produced with a thickness reduction of -0.44%. Another indenter-indenter test was executed after the indentation of the two disks in order to check possible changes. By subtracting the measured displacements of the two tests, the displacements at the indenter-specimen interface were obtained (red curve in Figure 3.11). In the Figure it is also plotted the FE prediction of the indentation process that will be described in the next Section.

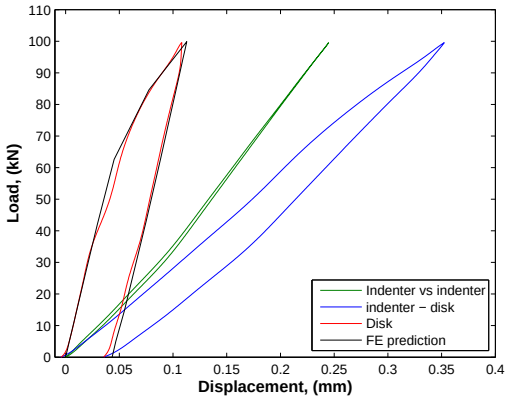

Figure 3.11 – *Load - displacement curves of the indentation process and FE prediction for the aluminum 2024-T351 disk.*

Chapter 4

Modeling

In order to evaluate the residual stress field produced by the indentation process, a FE simulation was executed. So the predicted residual stress can be compared with the results of the experimental tests executed in this study, and in the future can be compared with other residual stress measurement techniques.

4.1 FEM PREDICTION OF THE 316L SS DISK

The residual stress field produced by the indentation was simulated using the ABAQUS® finite element code [26]. A half-symmetry axi-symmetric model of the specimen was built using 15,000 four-node quadrilateral elements (CAX4R) with reduced integration. Square elements 0.1 mm on a side gave a 50 x 300 mesh in the disk. The indenter was modeled using the same element type but with a coarser mesh of 8,725 elements approximately 0.2 mm on a side. Figure 4.1 shows the FE model. The contact behavior between the indenter (master surface) and the disk (slave surface) was assumed frictionless because the lubricant was used during the experimental test, and a surface-to-surface contact algorithm was used. Axi-symmetric boundary conditions were imposed along the axis of the indenter and the specimen, while symmetric boundary conditions were imposed on the middle plane of the specimen. A displacement of -0.09 mm in the z-direction was applied at the upper face of the indenter (the actual cross-head displacement is the double due to the symmetry) in order to achieve the applied load of -90 kN, which is in agreement with the experimentally applied load.

In order to better predict the residual stress produced by indentation, it is needed to use in the FE analysis a very accurate model of the hardening behavior of the material. Thus, the behavior of 316L stainless steel first was modeled using an isotropic and a kinematic hardening model, both initially calibrated on the compression-only experimental data. The load-displacement curves obtained from the FE analysis for both isotropic and kinematic hardening do not exhibit any noticeable differ-

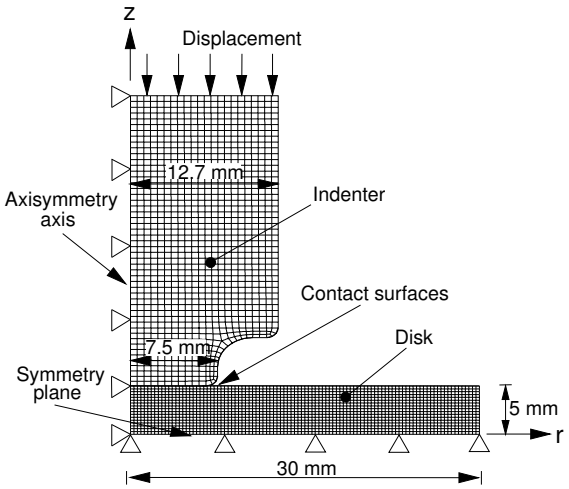

Figure 4.1 – *Details of the axial-symmetric finite element model used showing the planes of symmetry.*

ence, except a little difference during the unload for less than 10 kN. This is due to Baushinger effect. However both models gave a wrong response in case of reverse loading. These models were calibrated running FE analysis on a simple one element model, subjected to a uniaxial compression of -2% of true strain in the first step, followed by a tensile strain of 2% in the second step. As response, the isotropic hardening predict higher tensile stress than the experimental data after reverse loading (see Figure 4.2), while the kinematic model gave lower stress. The predicted residual stress obtained using these two hardening models are showed in Figure 4.3. It is evident that the different hardening model affects the residual stress because reverse loading happens.

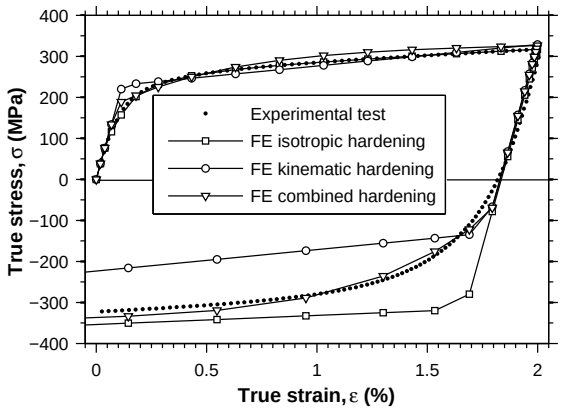

Figure 4.2 – *Hardening behavior of the 316L in a uniaxial compression and tension together with the FE combined hardening model.*

Since the experimental data from the cyclic test are in between the isotropic and

kinematic hardening models (see Figure 4.2), a combined hardening model, that involves a kinematic term and an isotropic one in its formulation, was used. In detail, the combined hardening model provided by ABAQUS® [32] was used. This hardening model is based on the work of Lemaitre and Chaboche [28]. The pressure independent yield surface is defined by

$$F = f(\boldsymbol{\sigma} - \boldsymbol{\alpha}) - \sigma^0 = 0 \tag{4.1}$$

where σ^0 is the size of yield surface and $f(\boldsymbol{\sigma} - \boldsymbol{\alpha})$ is the equivalent Mises stress with respect to the back-stress tensor $\boldsymbol{\alpha}$, that is defined by

$$f(\boldsymbol{\sigma} - \boldsymbol{\alpha}) = \sqrt{\frac{3}{2}(\mathbf{S} - \boldsymbol{\alpha}^{\mathbf{dev}}) : (\mathbf{S} - \boldsymbol{\alpha}^{\mathbf{dev}})} \tag{4.2}$$

where $\mathbf{S}$ is the deviatoric stress tensor, $\boldsymbol{\alpha}^{\mathbf{dev}}$ is the deviatoric part of the back-stress tensor and the symbol : is the double contracted product.

The isotropic hardening behavior of the model defines the evolution of the yield surface size, σ^0, as a function of the equivalent plastic strain, $\bar{\varepsilon}^{pl}$

$$\sigma^0 = \sigma_0 + Q(1 - e^{-b\bar{\varepsilon}^{pl}}) \tag{4.3}$$

where σ_0 is the yield stress at zero plastic strain, Q and b are material parameters. The non-linear kinematic hardening component is defined by an additive combination of a linear term and a relaxation term, which introduces the non-linearity:

$$\dot{\boldsymbol{\alpha}} = \frac{C}{\sigma^0}(\boldsymbol{\sigma} - \boldsymbol{\alpha})\dot{\bar{\varepsilon}}^{pl} - \gamma\boldsymbol{\alpha}\dot{\bar{\varepsilon}}^{pl} \tag{4.4}$$

The parameters for this combined hardening model were calibrated from the cyclic test described before using the procedure described in [26] and their values are: $\sigma_0 = 185$ MPa, $C = 28722$ MPa, $\gamma = 230.7$, $Q = 100$ MPa and $b = 12$.

The indenter material (A2 tool steel) was modeled by assuming linear elastic behavior, since the stresses do not approach yield, that is more that 1350 MPa, during indentation.

The load-displacement curve obtained from the FE analysis considering the combined hardening model is showed in Figure 3.10. Figure 4.3 shows the comparison of the FE prediction of the hoop and radial stress due to indentation using the

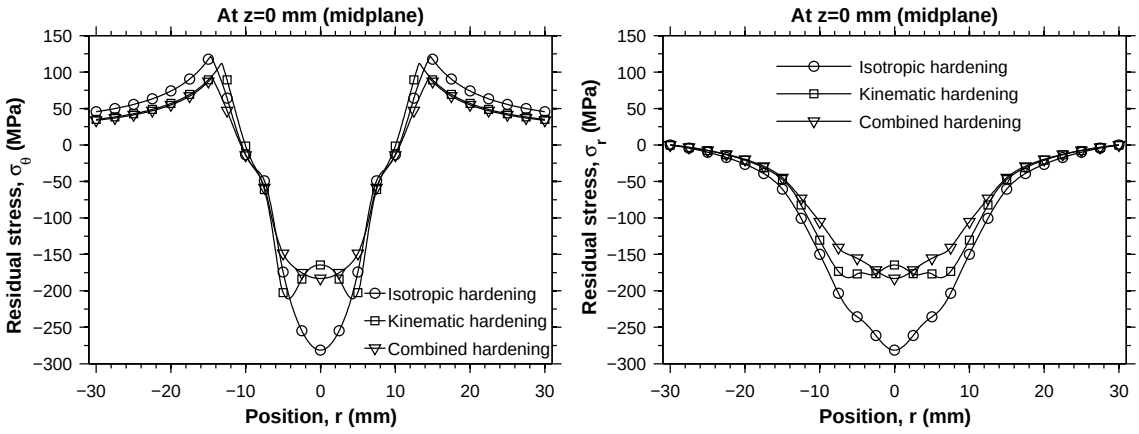

(a) (b)

Figure 4.3 – *FEM prediction of the hoop residual stresses along the diameter mid-thickness line using an isotropic, kinematic and combined hardening models of the 316L stainless steel respectively.*

isotropic, kinematic and combined hardening model respectively. The stresses under the indenter are quite sensitive to the hardening model because of significant reverse plasticity. Figure 4.4 shows the contour maps of the radial, hoop and axial residual stress predicted using the combined hardening model that better simulates the 316L stainless steel.

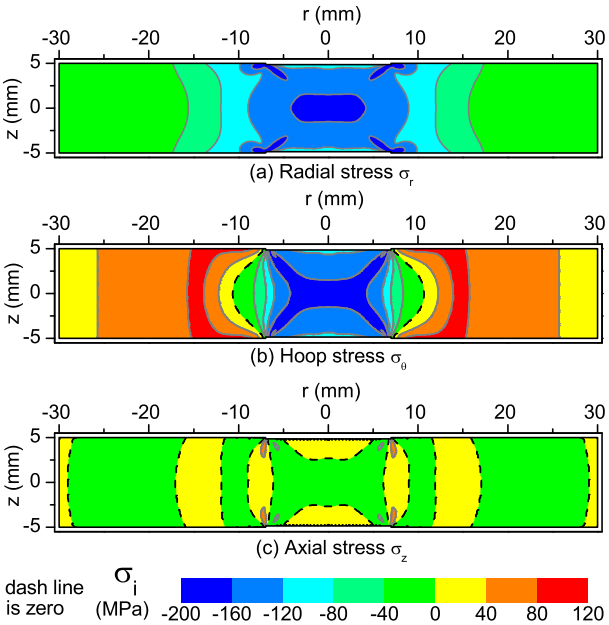

Figure 4.4 – *FEM prediction of the radial, hoop and axial residual stresses along the diameter plane using a combined hardening model of the 316L stainless steel.*

4.2 FEM PREDICTION OF THE ALUMINUM 2024-T351 DISK

The same FE simulation (see Section 4.1) was executed in order to predict the residual stress field produced by the indentation process on the aluminium 2024-T351 disk. The same FE model described before was used. However, a displacement of -0.11 mm in the z-direction was applied at the upper face of the indenter in order to achieve the applied load of -99.6 kN, which is in agreement with the experimentally applied loads. The elastic behavior of the aluminium 2024-T351 was modeled using a Young modulus of 73.2 GPa and a Poisson's ratio of 0.33. The hardening behavior was modeled using the same combined hardening model described by Eqs. 4.1-4.4, which parameters were calibrated from the cyclic test using the procedure described before and their values are: $\sigma_0 = 219.9$ MPa, $C = 67145$ MPa, $\gamma = 412$, $Q = 200$ MPa and $b = 7$, and shown in Figure 4.5 together with the experimental curve of the cyclic test.

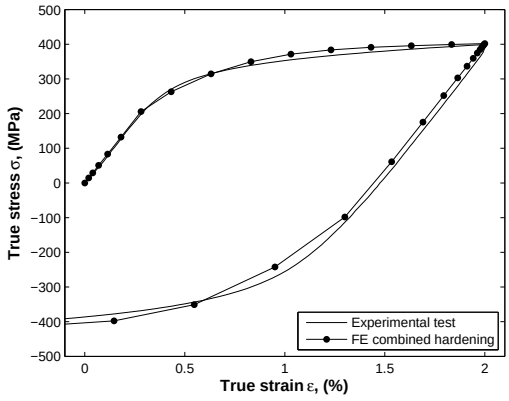

Figure 4.5 – *Hardening behavior of the aluminum 2024-T351 in a uniaxial compression and tension together with the FE combined hardening model.*

Figure 4.6 shows the FE prediction of the residual stress field (radial, hoop and axial stresses) on the aluminum 2024-T351 disk produced by the indentation process using the combined hardening model described by Eqs. 4.1-4.4, along the diameter plane.

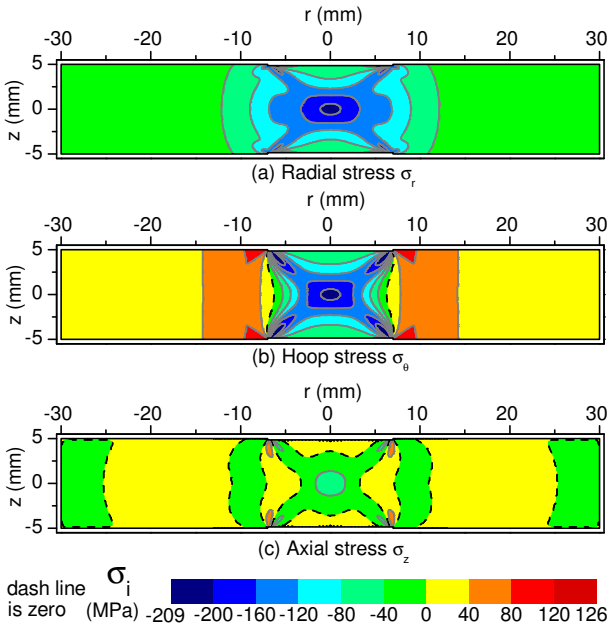

Figure 4.6 – *FEM prediction of the radial, hoop and axial residual stresses along the diameter plane using an isotropic hardening model of the aluminum 2024-T351.*

Chapter 5

Experiment: Neutron Diffraction

A neutron diffraction experiment was executed on the the 316L stainless steel disk in order to measure the residual stress field produced by the indentation process. This measurement will be useful to verify the FE prediction of the residual stress field and to compare with the other experimental measurement that were executed on the indented disks.

5.1 OVERVIEW

The physical principles of residual strain measurement by neutron and X-ray diffraction are identical. However, the deep penetration of thermal neutrons into engineering materials means that the experimental methods differ and that the strain information obtained nondestructively at depth complements, rather than supplants, the X-ray method. Thus, for example, the emphasis in neutron diffraction in on determination strain throughout the thickness of a steel component, whereas X-rays provide a measurement of the strain averaged over a few microns near the surface. A detailed description of the diffraction technique and its principle it is described in Chapter 8.

5.2 EXPERIMENTS

The neutron diffraction (ND) measurements were made using the SMARTS instrument (see Figure 5.1) at Los Alamos Neutron Science Center (LANSCE). LANSCE is a pulsed neutron source where the neutrons are generated by accelerating protons in a linear accelerator and bombarding them into a tungsten target.

Every time a proton pulse hits the target a burst of neutrons is generated by spallation. Each pulse of neutrons contains a spectrum of wavelengths and is moder-

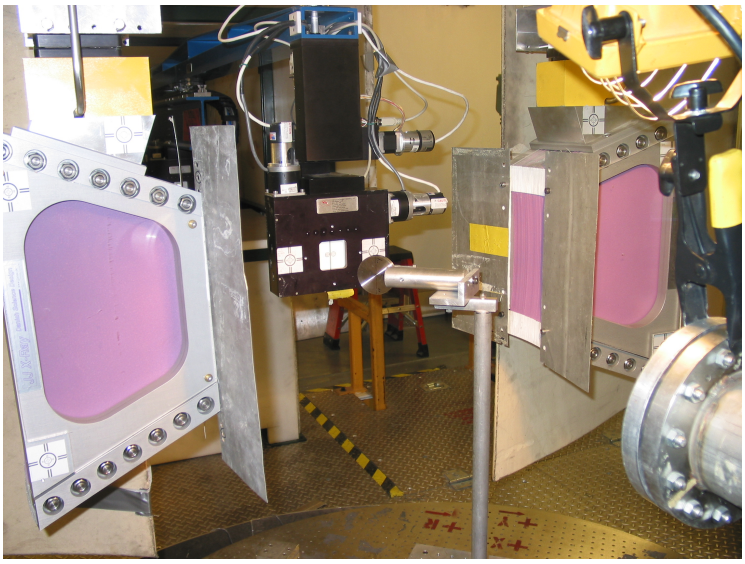

Figure 5.1 *– Experimental setup of the neutron diffraction test at SMARTS. The disk is in the center. The radial collimators are purple and the slit defining the width of the incident beam is in front of the disk.*

ated by passing through a chilled water moderator at 10 °C. The incident flight path on SMARTS is 31 meters, most of it in a neutron guide. SMARTS has two detector banks at plus and minus 90 degrees to the incident beam with a diffracted flight path length of about 1.5 m, see Figure 5.2(a). The total flight path, the scattering geometry and the 20 Hz repetition rate of the source dictates that the useable wavelength range on SMARTS is about 0.4 to 3.8 Å with maximum intensity between 0.5 to 1.5 Å.

A typical diffraction pattern for the 316L stainless steel from this study is shown in Figure 5.2(b). As seen in Figure 5.2(b), many peaks from the austenitic stainless steel are present enabling Rietveld full pattern analysis [33]. Being able to use multiple peaks in the refinement greatly improves the statistics, and using the GSAS software [34] we can determine the lattice parameter, a, of the fcc crystal structure with a relative accuracy of about 50×10^{-6}, or 50 microstrain ($\mu\varepsilon$), using count times on the order of 20 minutes. The incident slits were set to 2×2 mm^2, and a set of radial collimators limited the gauge volume to 2 mm along the incident beam path. An indented disk (disk A) was positioned so that the scattering vector for the +90 degrees bank, Q_1, was along the axial (z) direction, and the scattering vector for the -90 degrees bank, Q_2, was along the radial (r) direction of the disk. A series of measurements were made on a diameter plane by first scanning along the direction of $Q_2 = r$ (see Figure 5.2(a) and 5.3). Then the disk was rotated 90 degrees around the axial z direction, and another scan was performed in the vertical

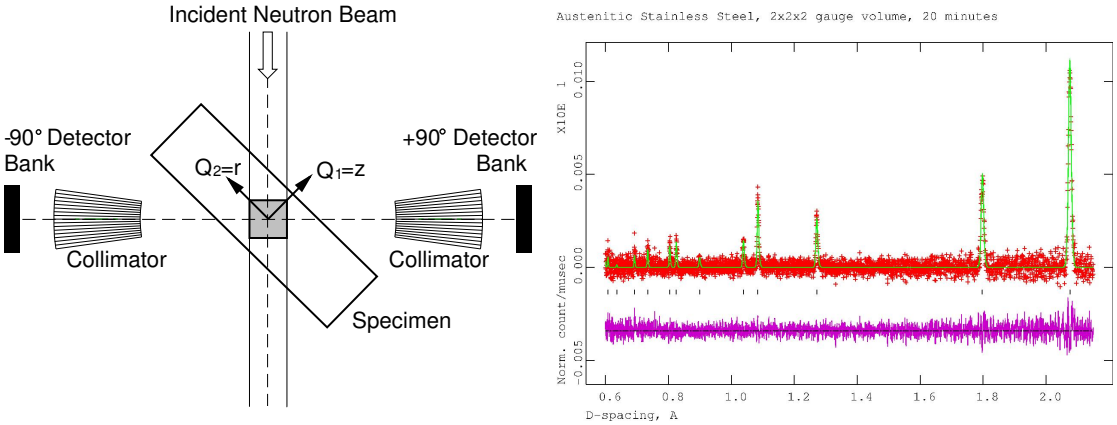

(a) (b)

Figure 5.2 – *(a) Schematic setup of SMARTS for spatially resolved measurements, and (b) Typical diffraction pattern. The red crosses are the data, the green line is the Rietveld refinement and the magenta line is the difference curve. The black tick-marks indicate the positions of the face-centered cubic peaks.*

direction (out of the plane of the paper in Figure 5.2(a)). Hence the first and second scans were made in the same physical positions within the disk, but in the first scan the radial strains,ε_r, were measured in the -90 degrees bank, and in the second scan the hoop strains, ε_θ, were measured in the -90 degrees bank. In both scans the axial strains, ε_z, were measured in the +90 degrees bank. Further measurements were also executed on an un-indented disk (disk C), so supposed stress free because of the annealing process, also verified by slitting test.

The lattice strains are calculated based upon a stress-free reference measurement. In this case the average stress-free lattice parameters from a series of measurements on three small cubes (5 mm × 5 mm × 5 mm) were determined. Then the residual strains can be calculated as follows:

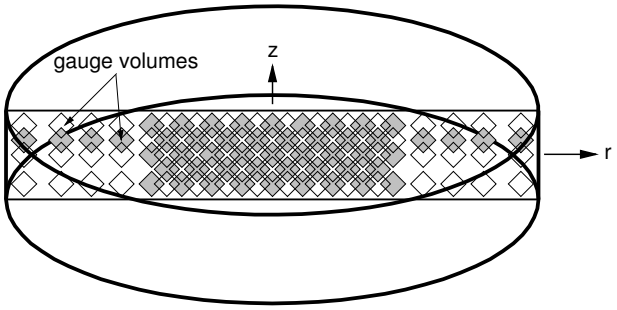

Figure 5.3 – *Location of gauge volumes (2 mm x 2 mm x 2 mm) for the neutron measurements. Some gage volumes are colored gray in order to distinguish overlapping volumes.*

$$\varepsilon_i = \frac{a_i}{a_i^0} - 1 \qquad i = r, \theta, z \tag{5.1}$$

where a_i and a_i^0 are the stresses and unstressed lattice parameters, respectively, in the test specimen and in the stress-free cubes along the different directions (r, θ and z). Then the residual stress components were evaluated using Hooke's law:

$$\sigma_i = \frac{E(1-\nu)}{(1+\nu)(1-2\nu)}[\varepsilon_i + \frac{\nu}{1+\nu}(\varepsilon_j + \varepsilon_k)] \qquad i, j, k = r, \theta, z \tag{5.2}$$

where E is the elastic modulus, and ν is Poisson's ratio.

5.3 RESULT

Figure 5.4 shows the residual stress components measured calculated with Eq. 5.2 from the neutron diffraction measured elastic strains. The maps are very similar to the one of the FE prediction shown in Figure 4.4 for the 316L stainless steel indented disk. The finer features of the prediction are not resolved because of experimental limits on both stress and spatial resolution.

Figure 5.5 shows the radial and the axial residual stresses measured by neutron diffraction along the mid-thickness line of the disk together with the FE predictions. The hoop residual stresses measured by neutron diffraction are showed in Figure 7.21 at pag. 64 together with the contour method results. The agreement between the neutron measurements and the FE prediction in excellent for all three residual stress components and it confirms the precision and effectiveness of the indentation process to introduce well known residual stress into samples.

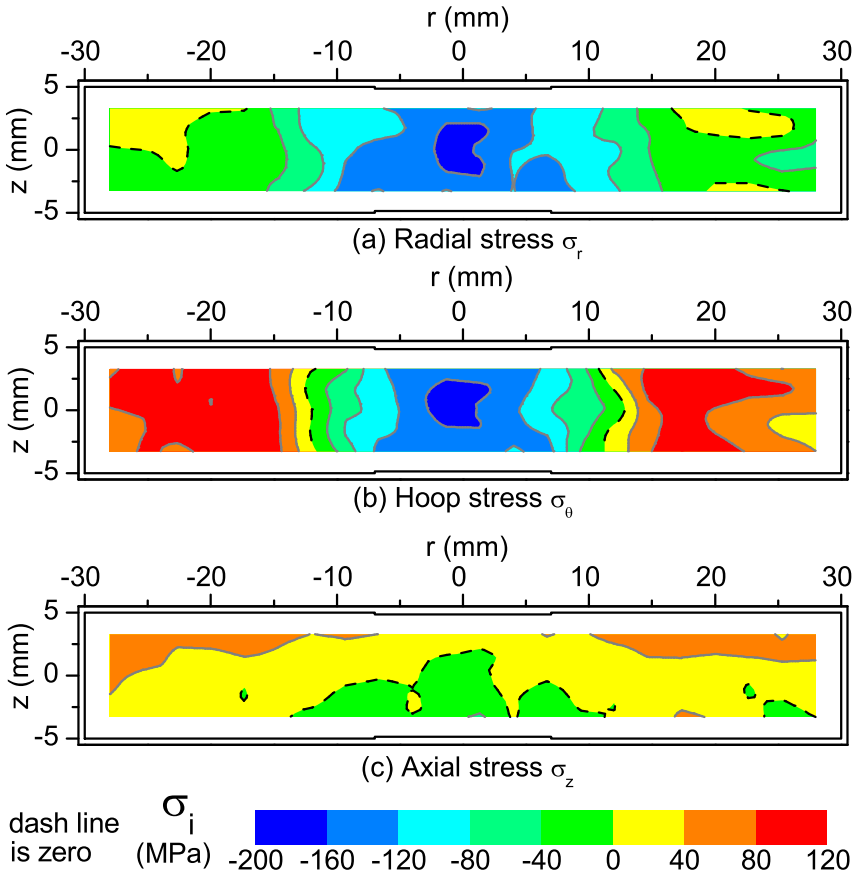

Figure 5.4 – *Maps of (a) radial, (b) hoop and (c) axial residual stresses measured with neutron diffraction on the diametrical plane.*

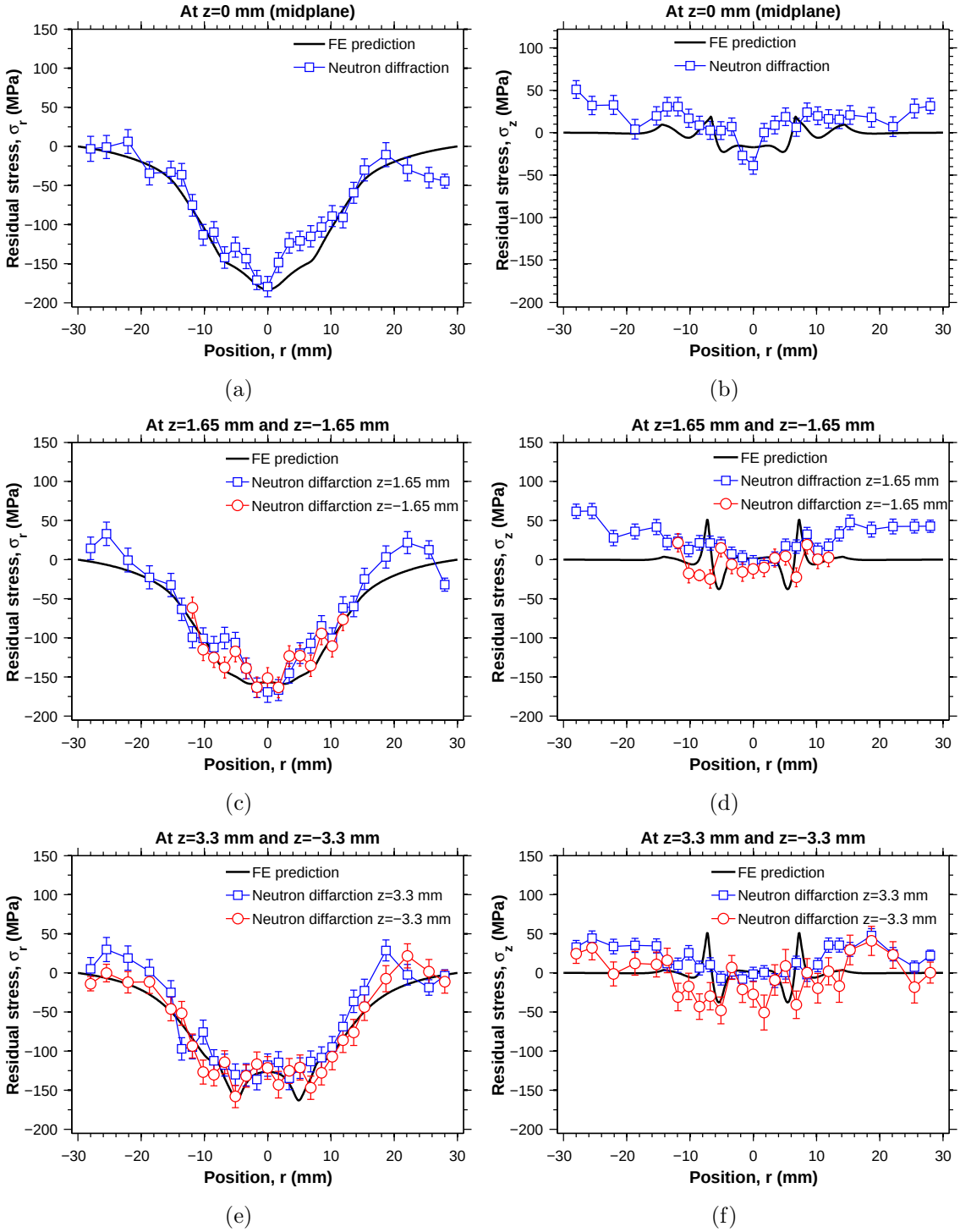

Figure 5.5 – *Radial and axial residual stresses measured with neutron diffraction plotted with the FE prediction along the mid-thickness line (z=0 mm), for* $z = \pm 1.65$ *mm and for* $z = \pm 3.3$ *mm respectively. (hoop stress are showed at pag. 64 together with the contour results)*

Chapter 6

Experiment: Slitting Method

In order to further validate the FE prediction of the residual stress, two slitting tests were executed on the the 316L stainless steel and aluminum 2024-T352 indented disks respectively, in order to measure the residual hoop stress, σ_θ, by the indentation process. This measurement will be useful also to compare the accuracy of this method with the other experimental techniques used in this study. Because the slitting method assumes a 1-D stress variation and there are 2-D variations in the disks, the slitting results are not expected to be as accurate.

6.1 INTRODUCTION TO SLITTING METHOD

In the slitting method (crack compliance) [30,35], see Figure 6.1, a narrow slit is incrementally cut into a part containing residual stresses. Stresses are relaxed and the part deforms, which is assumed to occur elastically. At an appropriate location strains are measured at discrete slit depths, a,

$$\varepsilon(a_i) = \varepsilon_i \tag{6.1}$$

where there are m slit depths $i = 1, m$, also called "number of cuts."

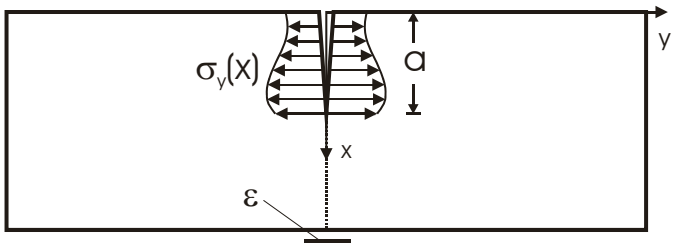

Figure 6.1 – *The incremental slitting method for measuring residual stress.*

Assuming that the stresses do not vary in the z-direction, the strain measured

at an arbitrary cut depth is related to the residual stresses that originally existed on the plane of the cut by a Volterra equation of the first kind,

$$\varepsilon(a) = \int_0^a c(a,x)\sigma_y(x)dx \tag{6.2}$$

where c is a function of the geometry and the material elastic constants. Since a closed-form inverse solution for $\sigma_y(x)$ is not available, it is assumed that the stress can be approximated as a series expansion in analytic basis functions

$$\sigma_y(x_i) = \sigma_i = \sum_{j=1}^{n} A_j P_j(x_i) = [P]\{A\} \tag{6.3}$$

The second equality introduces matrix notation for convenience; $[P]$ has rows corresponding to spatial positions x_i and columns corresponding to terms j in the series expansion. The solution for σ now requires choosing an expansion order n and determining the basis function amplitudes A_j. The solution strategy requires determining the strain release $C_j(a_i)$ that would occur at $a = a_i$ if $\sigma_y(x)$ were exactly given by $P_j(x)$. Using elastic superposition, the strain that would be measured for the $\sigma_y(x)$ from Eq. 6.3 is then given by

$$\varepsilon_f(a_i) = \varepsilon_{f,i} = \sum_{j=1}^{n} A_j C_j(a_i) = [C]\{A\} \tag{6.4}$$

where the subscript f refers to these calculated strains being determined by a least squares fit minimizing the difference between the measured strains, ε, and calculated strains:

$$\{A\} = [([C]^T[C])^{-1}[C]^T]\{\varepsilon_{measured}\} = [B]\{\varepsilon\} \tag{6.5}$$

6.2 EXPERIMENTS

Experiments were performed on a 316L stainless steel indented disk and an aluminum 2024-T351 indented disk. The disks, as said before, were 60 mm in diameter and 10 mm thick. the slitting method was applied in order to measure the hoop stresses along the diameter plane. A cut was made incrementally, and the hoop stress component normal to the cut plane is determined. For each specimen, one strain gage was placed very close to the cut on the surface where the cut begins (top),

and another is placed centered on the cut plane on the opposite surface (bottom) (see Figure 6.2). The gages used were Micro-measurements CEA-09-032UW-120 and CEA-09-062-UW-350 gages respectively on the top and bottom surfaces of the 316L stainless steel disk. Instead for the aluminum 2024-T351 were used a CEA-13-032UW-120 gage on the top surface and a CEA-13-062UW-350 on the bottom surface.

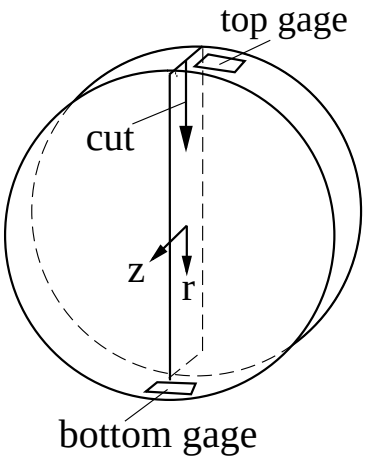

(a)

Figure 6.2 *– (a) Test procedure and strain gage layout; (b) EDM cut of the disk.*

The cuts were executed along the diameter plane as showed in Figure 6.2 using wire electrical discharge machining (EDM) with a 250 μm diameter brass wire. The machine was set to "skim cut 2" setting to minimize the stress induced during cutting [19]. The slot was cut in 1.524 mm increments to a depth of 57.92 mm (38 cuts). After each increment, the gage readings were taken. During the test, at the first and third cut, there was a long break because of some problem with the EDM machine. So, before starting again the readings were taken another time and used to correct the data. The test on the aluminum 2024-T351 disk was performed under the same conditions as the previous test. Figure 6.3(a) and 6.3(b) show the strains measured during the cuts for the 316L stainless steel disk and for the aluminum 2024-T351 disk respectively.

The original residual hoop stresses, σ_θ, were determined from the measured strains using the series expansion approach [30,36], which is very tolerant of noise and errors in the measured strains [37]. It is first assumed that the unknown stress variation as a function of the through-thickness coordinate can be expressed as a series expansion, see Eq. 6.3. For this application, Legendre polynomials, $L_i(x)$, expanded over the thickness of the plates were chosen for the P_i because, by excluding

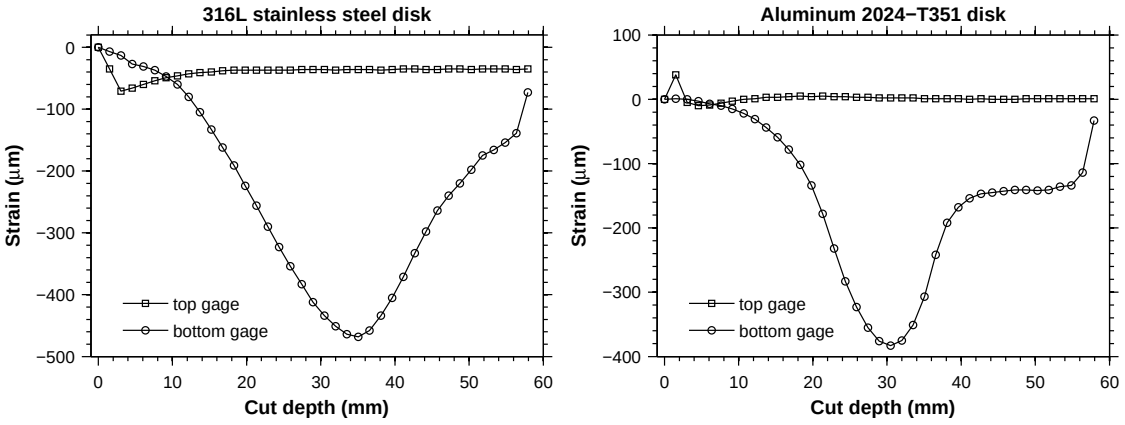

(a) (b)

Figure 6.3 *– Measured strains, (a) 316L stainless steel indented disk and (b) aluminum 2024-T351 indented disk.*

the 0th and 1st order polynomials, the resulting stress distribution is guaranteed to satisfy force and moment equilibrium. Thus the expansion in Eq. 6.3 starts with the 2nd order Legendre polynomial, $L_2(x)$.

The strains that would be measured at the cut depths a_j are calculated for each term in the series. These are called the compliance functions C_{ij}. Using superposition, the strains given by the series expansion can be written as Eq. 6.4. A least square fit to minimize the error between the strains given by Eq. 6.4 and the measured strains gives the A_i, and hence the stresses by Eq. 6.3, and can be written as Eq. 6.5.

A finite element (FE) model was used for calculating the compliance functions C_{ij}. The use of finite elements to determine calibration coefficients is commonplace and described in more detail elsewhere [30,38,39,40,41]. The calculations were carried out using the commercial code Abaqus® [26]. The calculations were executed using 2-D FE model of half disk. A 2-D plane stress mesh was used with quadratic shape function elements (CPS8) sized at about 1 mm. The elastic modulus was taken equal to 1 and Poissons ratio equal to 0. Only half of disk was meshed because of symmetry about the cut plane. Incremental cutting was simulated by incrementally removing symmetry displacement boundary conditions on the cut plane. The elements edges defining the exposed face of the slit were loaded with a nonuniform pressure distribution sequentially corresponding to $L_2(x)$ through $L_{16}(X)$, i.e. form 2nd to 16th order Legendre polynomials. The remaining surfaces were taken as traction free. The strains for the top strain gage in Figure 6.2 was then calculated by computing the relative displacement of the nodes corresponding to the begin and end of the strain gauge and dividing by initial length between the nodes. For the

gauge centered on the symmetry plane was only needed to consider the displacement of the nodes corresponding to the center and end of the strain gauge. Note that this FE model approximated the actual, finite-width slot ($\sim$ 0.29 mm) as a crack. For the gage positions in these tests, the error caused by this approximation is quite small [42]. Hence, the extra effort to mesh the actual slot width is not justified. Finally, the series expansion coefficients A_i were determined by least squares fit (Eq. 6.5) using the measured strains for the relevant gages and the FE-calculated compliance functions. The order of fit was chosen to minimize the uncertainty in the calculated stresses [38,43]. A Height term series (Legendre polynomial order 2 to 9) was sufficient for fitting the data for the 316L disk, instead for the aluminium disk test it was required 11 terms (Legendre polynomial order 2 to 12). The coefficients were multiplied for appropriate conversion factor in order to take account of the actual elastic modulus.

6.3 RESULTS

Figures 6.4(a) and 6.4(b) show the residual hoop stresses, σ_θ, measured along the diameter plane of the 316L stainless steel disk and the aluminum 2024-T351 disk, considering only the bottom gage (blue curves) and both gages (red curves). Figures 6.4(a) also shows the FE prediction averaged over the thickness (black curve) for the 316L stainless steel disk, because in this application of the slitting method the measured strain are affected by the relaxed stress over the thickness. So, this average is more reasonable to compare with the slitting result.

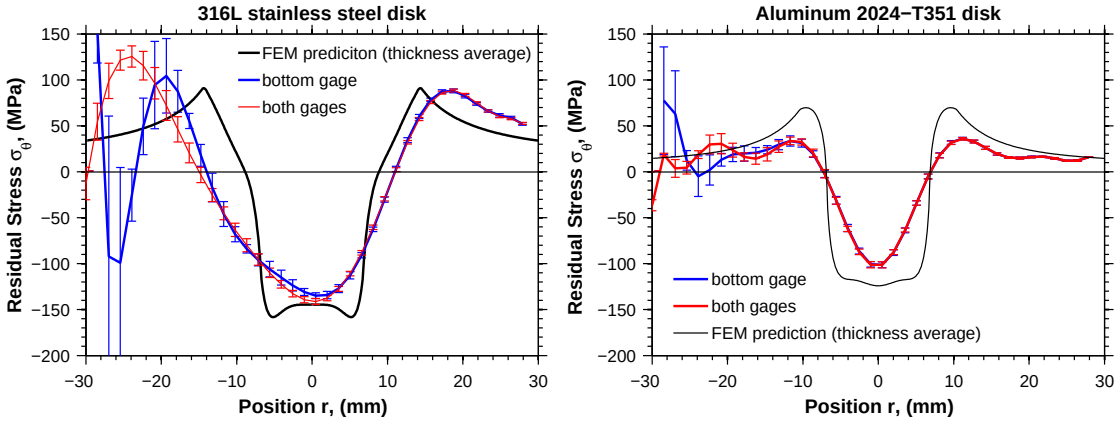

(a) (b)

Figure 6.4 – *Residual hoop stress, σ_θ, (a) 316L stainless steel indented disk and (b) aluminum 2024-T351 indented disk.*

For the 316L stainless steel disk, the residual stress distribution considering the bottom gage only does not look good, in fact it does not make sense for low depth

and are not symmetric, even though the strain fit is fairly stable and the strains are fitted well. Considering both gages in the calculation, the stresses (red curve in Figure 6.3(a)) look slightly better even thought is not possible to fit both gages well at the same time. Not fitting both gages at same time can be an indicator of 2D stresses over cross section in thick specimens. Then, the early strain readings on back gage also seem very un-physical, they are increasing in magnitude too fast. There may be EDM induced stress effects on the top gauge because of the large wire used.

For the aluminum 2024-T351, the residual stress distribution look better and of very good quality, even thought the top gage data do not seem quite right. For bottom gage only, the strain fit was very stable except near the front, which is expected since the strains are low, and the strain fit was good enough. Instead considering both gages, the strain fit are very good and the stresses are more stable. Then, the stress distribution is very symmetric, how it is supposed to be. The agreement with the FE prediction is not great in the center of the disk with difference up to 50 MPa.

The results for both test use plane stress calibration coefficients because of the small thickness compared to the diameter. However the stress results could be multiplied by $1/(1-\nu^2)$ to obtain the stress in case of plane strain.

For future similar test, it is needed to take smaller cut increments for low depth in order to have better top gage data.

Chapter 7

Experiment: Contour Method

This chapter presents traditional contour method measurements on the specimens used to validate the theories in Chapter 2. Before the steel and aluminum disks, results are presented from a preliminary study on a quenched steel plate. Results from second cuts on some specimens are presented, but the superposition results to evaluate the new theories are presented in later chapters.

7.1 HSLA-100 QUENCHED PLATE

In this section it is presented the application of the classical contour method to two cuts on a HSLA-100 quenched plate in order to eventually evaluate the residual stress components along the two in-plane directions and in order to validate the new theoretical development proposed in this thesis. In fact, the particular residual stress field of this quenched plate (equi-biaxial) is well suited to validate the theory.

7.1.1 Experiments

The plate material tested in this study was a low carbon, copper precipitation-hardened, High-Strength Low-Alloy steel: HSLA-100. This steel is used for naval ship hulls, armor, and containment vessels. The chemical composition is given in Table 7.1. The 60.75 mm thick plate material was prepared by hot cross-rolling. It was austenitized at 900 °C for 75 minutes and then water quenched. The plate was then tempered at 660 °C for 200 minutes followed by another water quench. The specification for this material does not allow thermal stress relief because of potential loss of strength. Therefore, the quenching stresses can be expected for all uses of this material. Mechanical testing gave yield strengths of 690 MPa in the final rolling direction and 685 MPa in the transverse direction, with corresponding ultimate strength of 813 MPa and 829 MPa, respectively. A section of plate measuring 151.6 mm and 301 mm long was saw cut from a larger plate for this measurement

of residual stress (see Figure 7.1).

Table 7.1 – *Alloying elements of HSLA-100 steel plate in weight-%*

C	Mn	P	S	Cu	Si	Ni	Cr	Mo	V	Ti	Al
0.06	0.85	0.005	0.002	1.56	0.26	3.45	0.56	0.58	0.003	0.001	0.025

The specimen was cut in half on the first measurement plane indicated in Figure 7.1 using wire electric discharge machining (EDM) and a 150 μm diameter brass wire. The part was submerged in temperature-controlled deionized water throughout the cutting process. "Skim cut" settings, which are normally used for better precision and a finer surface finish, were used because they also minimize any recast layer and cutting-induced stresses [35]. Because the part deforms during the cutting as stresses are relaxed, the cut could deviate from the original cut plane, which would cause errors in the measured stresses. Therefore, the part was constrained by clamping it on both sides of the cut to a steel plate, which was in turn clamped in the EDM machine (see Figure 7.2). To prevent any thermal stresses, the specimen and the fixture were allowed to come to thermal equilibrium in the water tank before clamping.

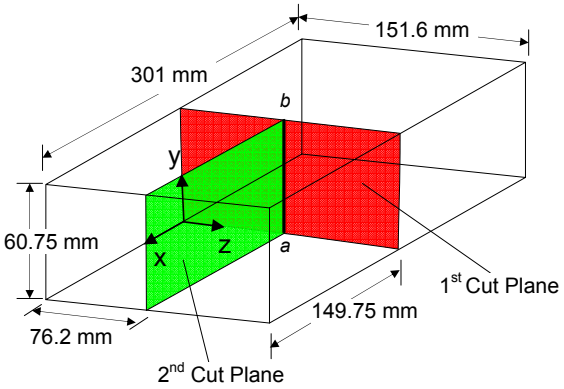

Figure 7.1 – *Dimension of the HSLA specimen and cut locations.*

After cutting, the plate was removed from the clamping fixture. The contours of both surfaces were measured using a MS Impact II coordinate measuring machine (CMM), an inspection tool that uses a touch probe. A 1 mm diameter spherical ruby tip was used on the probe. The cut surfaces were measured on a 0.5 mm spaced grid, giving about 36.500 points on each cut surface.

Figure 7.2 shows the front half of the specimen being cut in half another time along the second cut plane shown in Figure 7.1. The procedure, the machine and the working conditions were the same of the first cut. After cutting, the plate was removed from the clamping fixture. The contours of both surfaces were measured

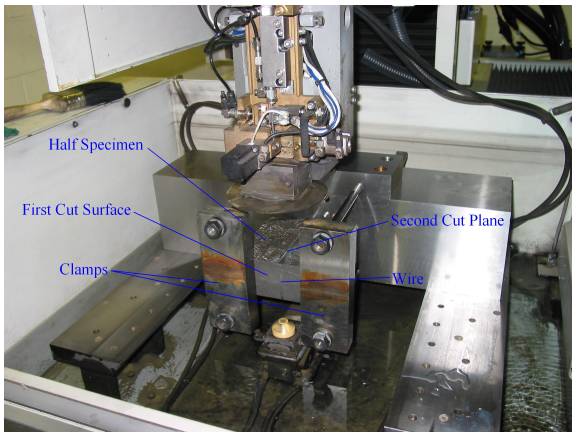

Figure 7.2 – *Half of the original specimen and the clamping fixture to execute the 2nd cut on the EDM machine.*

by a different CMM machine, this time using a non-contact probe (see Figure 7.3). The specimen was scanned using rows separated by 0.5 mm with data points within a row sampled every 0.095 mm, giving about 171.000 points on each cut surface.

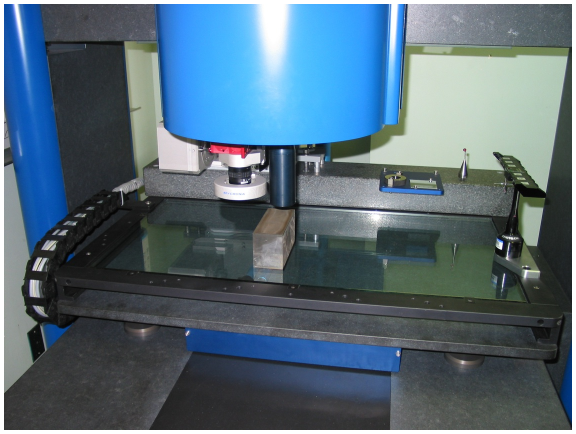

Figure 7.3 – *HSLA specimen being scanned in Coordinate Measuring Machine using non-contact probe.*

7.1.2 Calculations

The procedure for analyzing the data to calculate stresses is presented in more detail elsewhere [2]. The relevant details for this experiment are presented here.

Figure 7.4 shows the average of the contours measured on the two opposing surfaces created by the first cut (Figure 7.4(a)) and then smoothed by fitting the data to a surface using bivariate smoothing spline (Figure 7.4(b)) [2]. The peak-to-valley amplitude of the contour is about 50 μm. The primary shape of the contour is low in the mid-thickness of the plate and higher toward the top and bottom.

Figure 7.5 shows the same result for the second cut. The peak-to-valley amplitude of the contour is about 50 μm, very close to the first cut surface, but this time the rough contour (Figure 7.5(a)) is affected by more noisy due to the different measurement technique (non-contact probe).

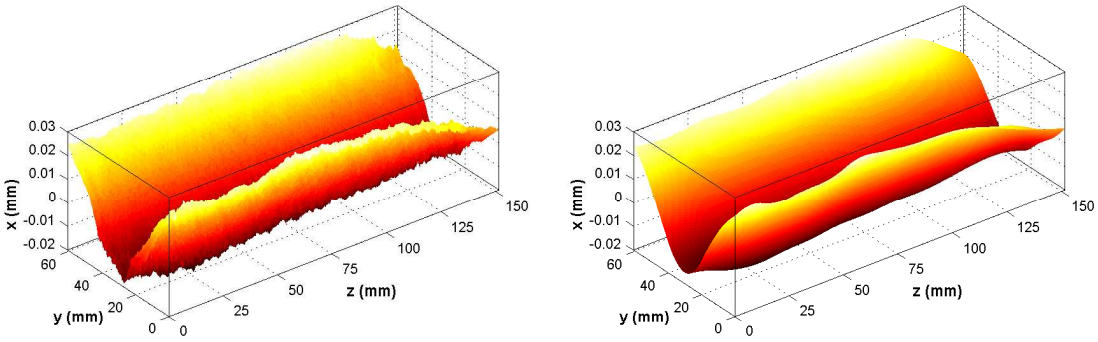

(a) (b)

Figure 7.4 – *Contour measured on the first cut surface: (a) rough data; (b) spline smoothed data.*

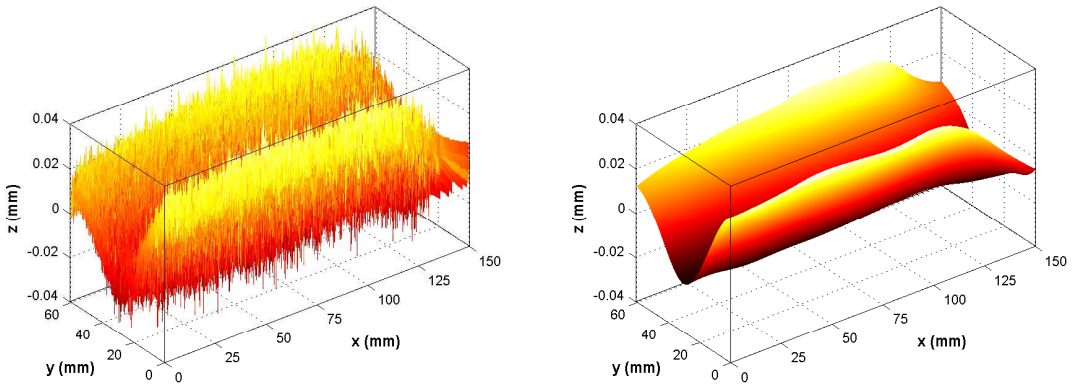

(a) (b)

Figure 7.5 – *Contour measured on the second cut surface: (a) rough data; (b) spline smoothed data.*

The σ_x stresses that were originally present on the plane of the first cut were calculated numerically by elastically deforming the cut surface into the opposite shape of contour that was measured at the same surface [1]. This was accomplished using the ABAQUS® 6.5 commercial FE code [26] and a 3-D elastic finite element model (see Figure 7.6(a)). A model was constructed of the front half of the specimen shown in Figure 3 (the condition after it had been cut in two). The mesh used 211.680 linear hexahedral (8 node) elements. The material behavior was isotropic elastic with

an elastic modulus of 197 GPa and a Poisson's ratio of 0.29. In order to smooth out noise in the measured surface data and to enable evaluation at arbitrary locations, the data were fitted to a bivariate smoothing spline. The bivariate smoothing spline fits to the measured contour data were evaluated at a grid corresponding to the FE nodes, averaged between the two cut surfaces deformed into the opposite of the measured contour.

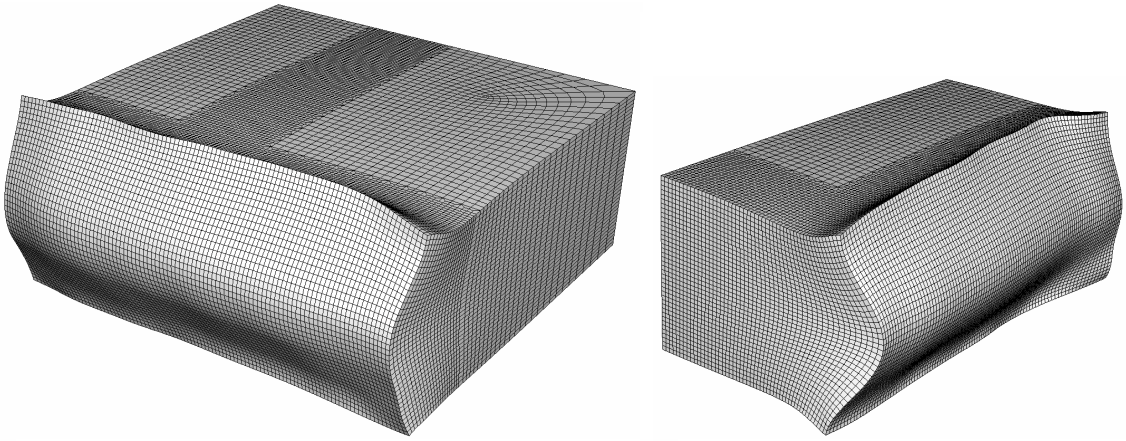

(a) (b)

Figure 7.6 – *FE model of HSLA-100 steel plate deformed into opposite of measured shape in order to calculate original residual stresses: (a) after the first cut and (b) after the second cut, Deformation magnified by 400. This mesh corresponds to the front half of the specimen in Figure 7.1.*

As described before, the σ_z stresses that were present on the second cut plane after the execution of the first cut (step B in Figure 2.2) were calculated numerically by elastically deforming the second cut surface into the opposite shape of contour that was measured on the same surface. This was accomplished using half of the previous 3-D FE model (see Figure 7.6(b)), by using the removing elements command in the second step of the previous FE analysis. The same fitting method was used to smooth the measured surface. This time was more noise in the data because of the probe used [2].

7.1.3 Results

Figure 7.7 shows the σ_x residual stresses on the first cut plane from Figure 7.1 (step A=C in Figure 2.2). Typical quenching stresses, tension in the center balanced by compression at the top and bottom, are evident. Within about 20 mm of the lateral edges, the stresses are noticeably different from those in the central region. Those edge effects are consistent with stress relaxation when the test specimen was removed

from a large quenched plate, as was demonstrated by a finite element simulation of the stress relaxation caused by removing the test specimen [24].

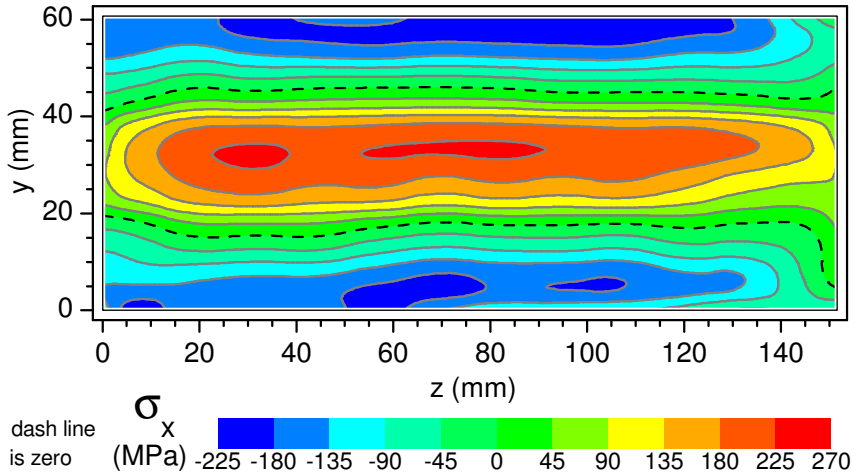

Figure 7.7 – *Original σ_x residual stresses (Step A in Figure 2.2) in HSLA-100 specimen measured by the contour method on the first cut plane.*

Figure 7.8 shows the σ_z residual stresses on the second cut plane from Figure 7.1 after the second step of FE analysis (step B=E in Figure 2.2). This stress map is very similar to the previous map (Figure 7.7), but in the left edge the effect of the first cut is evident (the right edge shows the effect or the original removal of the test specimen from a large quenched plate).

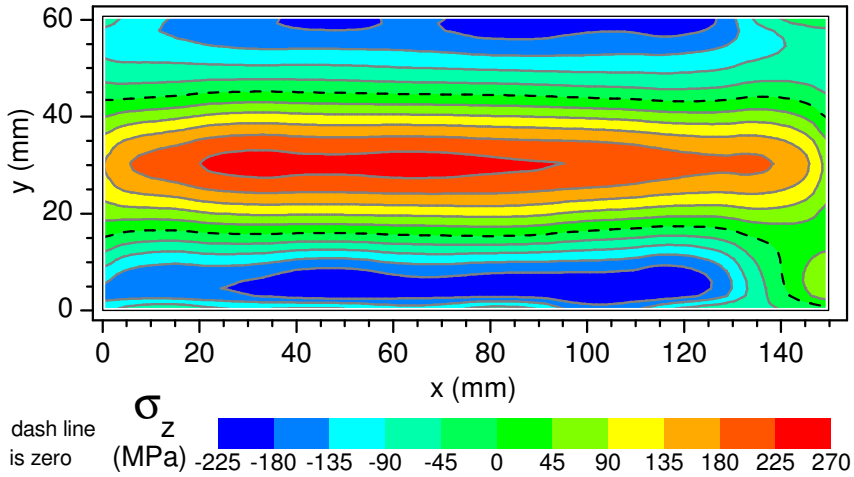

Figure 7.8 – *Residual stresses σ_z in HSLA-100 specimen after the second cut (step B=E in Figure 2.2) measured by the contour method on the second cut plane*

7.2 316L STAINLESS STEEL DISKS

In this section it is presented the application of the classical method to four 316L stainless steel disks (disks: A, B, C and D). In detail, disks A and B were indented in the same condition, so virtually they should have the same residual stress field. Disk C and D were not indented so they should not be subjected to significant residual stresses, because the 316L SS plate was annealed. The indented disk A and the blank one C were the same scanned by neutron diffraction. Furthermore, the indented disk B was cut another time along a plane normal to the first cut plane, in order to apply the multiple cut contour method.

7.2.1 Experiments

The contour method (CM) was applied to both the indented disks (disk A and B) and, as a control, to the unindented disk (disk C and D). The conventional contour method was applied to measure the hoop stress over a diametrical cross section. The intended disk A and a not-indented disk C were the same planes scanned by neutron diffraction (see Chapter 5).

The disks A and C were cut in half along the same planes scanned by neutron diffraction using a wire electric discharge machining (EDM) Mistsubishi SX-10 and a 50 μm diameter tungsten wire, and Epak 405 and "skim cut" settings were used. Instead, disks B and D were cut in half using the same EDM machine but with a 100 μm diameter brass wire (that is the usual size for contour cutting) and using Epak 432, skim cut 1 for 1/2 in. thick steel settings, and adaptive control were used for these cutting. All the parts were submerged in temperature-controlled deionized water throughout the cutting process. The parts were constrained by clamping on both sides of the cut to the work plate of the EDM machine (see Figure 7.9), known as the "bridge" clamping system [4]. To prevent any thermal stresses, the specimens and the fixture were allowed to come to thermal equilibrium in the water tank before clamping. As it is possible to see from Figure 7.9, the clamp directions were parallel to the wire axis and perpendicular to the cutting direction. Cut processes took about 12 hours for the indented disk A and the blank disk C, instead for the indented disk B and the blank one D it took about 2.5 hours. A test slit was cut on another not-indented disk (disk D) using the 50 μm tungsten wire and then the resulting cut width was measured with the microscope giving about 82 μm.

After cutting the disks, the contours of the resulting four surfaces of the disks A and C halves were measured using a Taylor-Hobson Talyscan 250 laser scanner [44]. A laser triangulation probe of 2 mm range and resolution of 0.1 μm was used. The cut surfaces were measured on a 0.1 mm spaced grid, giving about 60.000 points

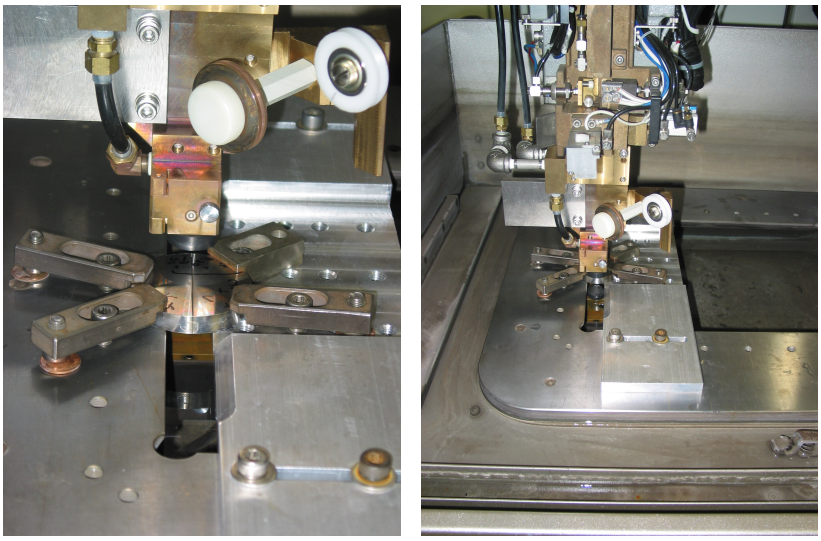

(a) (b)

Figure 7.9 *– 316L disk and the clamping fixture to execute the cut on the EDM machine.*

on each cut surface. As it is possible to see from Figure 7.10, the four disk halves were positioned on the work plane of the laser scan machine, aligning the axis of the halves, so the following data alignment and data reduction were easier.

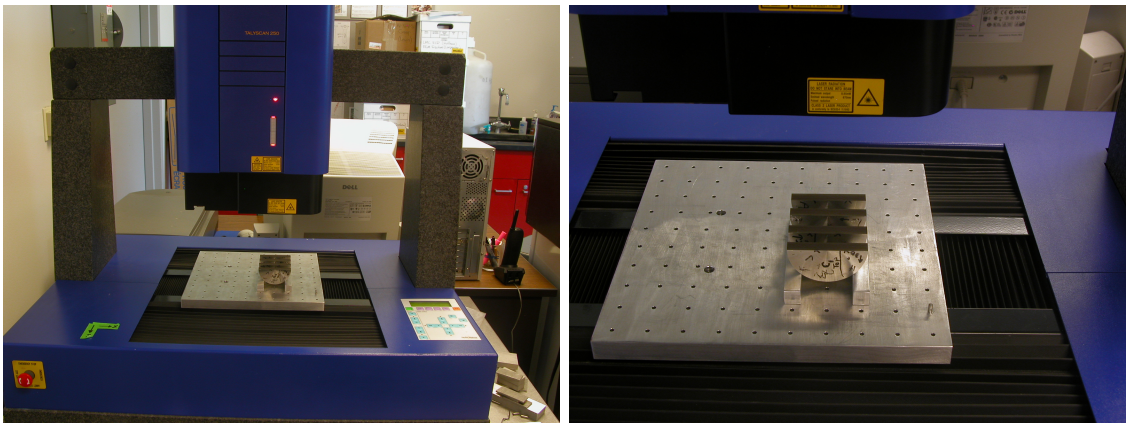

(a) (b)

Figure 7.10 *– 316L disks A and C being scanned using a Taylor-Hobson Talyscan 250 laser scanner.*

Instead, the contours of the resulting four surfaces of the disks B and D halves were measured using the laser scan machine described in [2] and shown in Figure 7.11. The cut surfaces were scanned using rows separated by 0.1 mm in the axial direction, z, with data points within a row sampled every 0.04 mm, giving about 113.000 points on each cut surface.

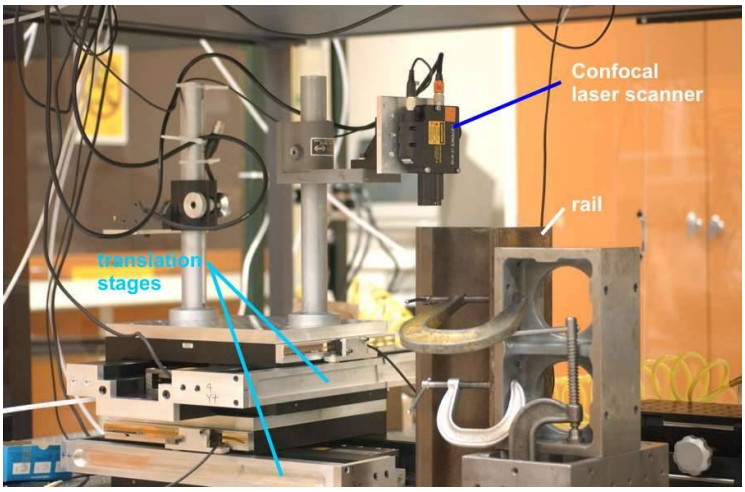

Figure 7.11 *– Laser scanner machine used to measure disk B and D.*

7.2.2 Calculations

The raw data was processed into a form suitable to calculate stresses using a procedure described in detail elsewhere [2]. Data points from when the probe was off of the surface were removed [1]. The two point clouds (the collection of x, y, z data-points that define each surface) for each specimen were aligned in a common coordinate system, mirroring one of the two clouds with respect to the axial direction. Since the data points do not extend completely to the part edges, an extrapolation was executed by means of Delaunay triangulation with a nearest point option that uses the value of the nearest point. Alternatively, a the linear interpolation option could be used, but in this case it doesn't work well because it makes a triangulation between points too far from each other. The data were interpolated in a common grid in order to average the clouds point by point to provide a single data set and also to minimize several potential error sources, as better described in [2]. Figure 7.12 shows the average of the contours measured on the two opposing surfaces created by the cut for the blank disk C (Figure 7.12(a)) and the indented disk A (Figure 7.12(b)) respectively. The peak-to-valley amplitude of the contour is about 8 μm for the blank disk C and 40 μm for the indented disk A.

The contour on the unindented disk C was used to correct the contour on the indented disk A. From Figure 7.12(a) it is evident that the measured contour of the blank specimen is not flat. Slitting test on the annealed 316L material (see Section 3.3) indicated that the post-annealing stresses were less than 10 MPa. The neutron results in the unindented disk C are consistent with these low stresses, although this low stress is difficult to measure precisely with neutrons. Therefore,

[1] using the MATLAB function cmm_clean.m written by Greg Johnson

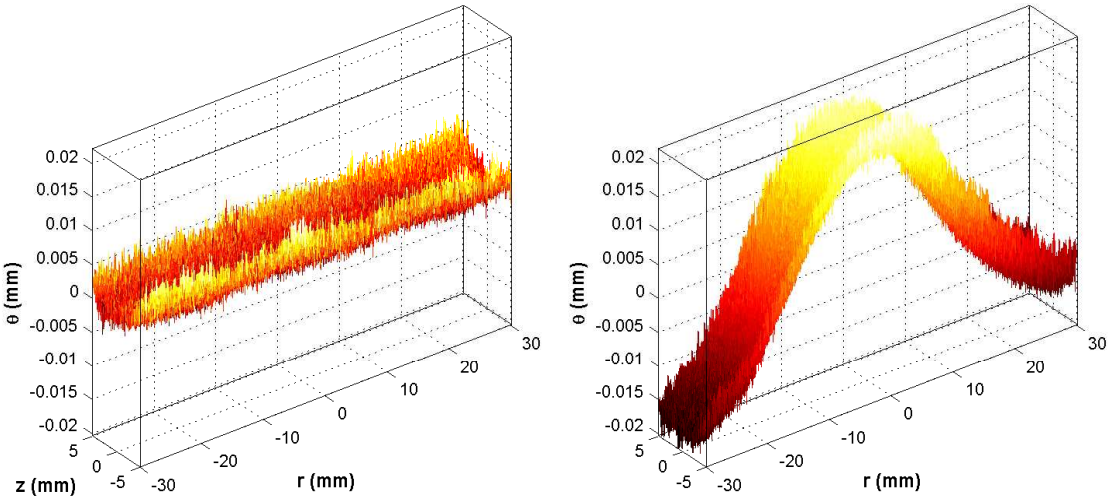

(a) (b)

Figure 7.12 – *Measured contour on the cut surface: (a) blank disk C and (b) indented disk A*

the contour on the unindented disk is probably caused by the EDM cutting and not by residual stress since it would require stresses over 100 MPa to produce such a contour. As described before, the wire used had half the diameter of the smallest wire previously used for contour measurements. A lower tension must be used with smaller wire, and it is affected by vibrational bending. So, to eliminate this effect in the indented disk, the blank disk contour was subtracted from the indented disk contour (see Figure 7.13).

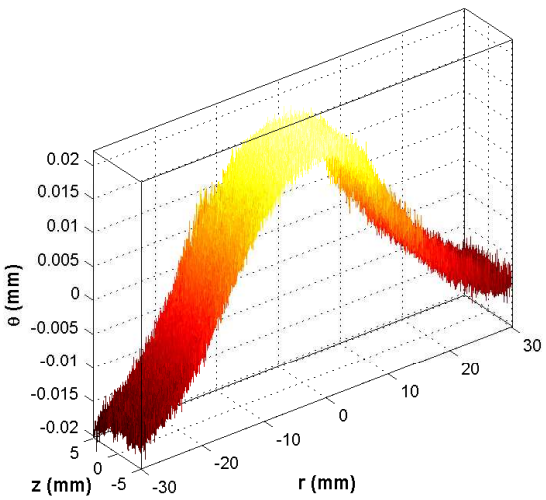

Figure 7.13 – *Contour of the indented disk A corrected with the contour of the blank disk C.*

In retrospect, since cutting the disks A and C with a 50 μm diameter wire gave

not very accurate result, the disks B and D were cut with a 100 μm diameter wire that is the usual size for contour cutting. Figure 7.14 shows the average of the contours measured on the two opposing surfaces created by the cut with 100 μm diameter wire for the blank disk D (Figure 7.14(a)) and the indented disk B (Figure 7.14(b)) respectively. The peak-to-valley amplitude of the contour is about 5 μm for the blank disk D, but it is only noisy, in fact the average value is zero. Instead, for the indented disk B the peak-to-valley amplitude is about 40 μm, as for the disk A.

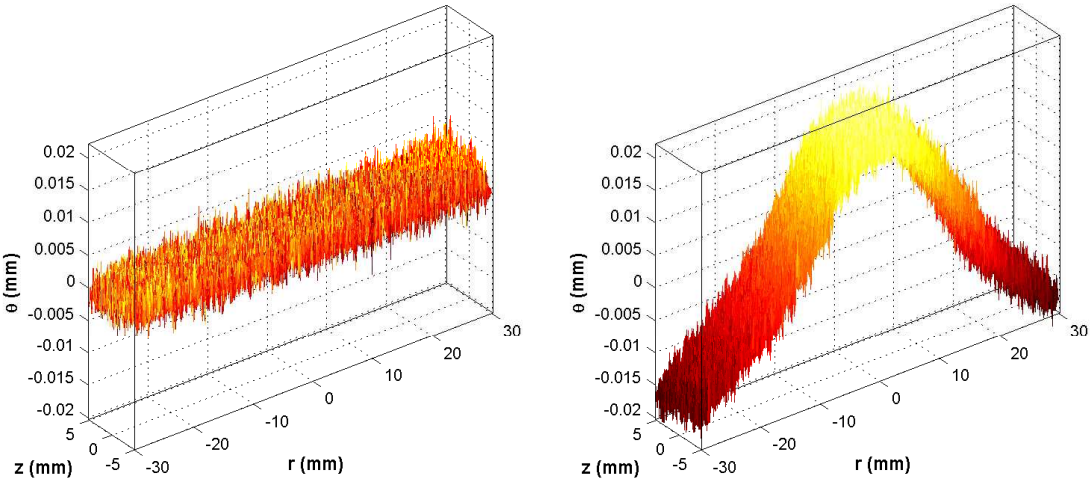

(a) (b)

Figure 7.14 – *Measured contour on the cut surface: (a) blank disk D and (b) indented disk B.*

The σ_θ stresses that were originally present on the cut plane were calculated numerically by elastically deforming the cut surface into the opposite shape of contour that was measured at the same surface [1]. This was accomplished using the ABAQUS® commercial FE code [26] and a 3-D elastic finite element model (see Figure 7.15(a)). A model of half of the disk specimen was constructed. The mesh used 51.920 linear hexahedral 8-node elements with reduced integration (C3D8R). The material behavior was considered elastically isotropic with an elastic modulus of 193 GPa and a Poisson's ratio of 0.3. In order to smooth out noise in the measured surface data and to enable evaluation at arbitrary locations, the data were fitted to a bivariate smoothing spline. The smoothing spline fits were evaluated at a grid corresponding to the FE nodes, and those values at the nodal locations were then used as displacement boundary conditions.

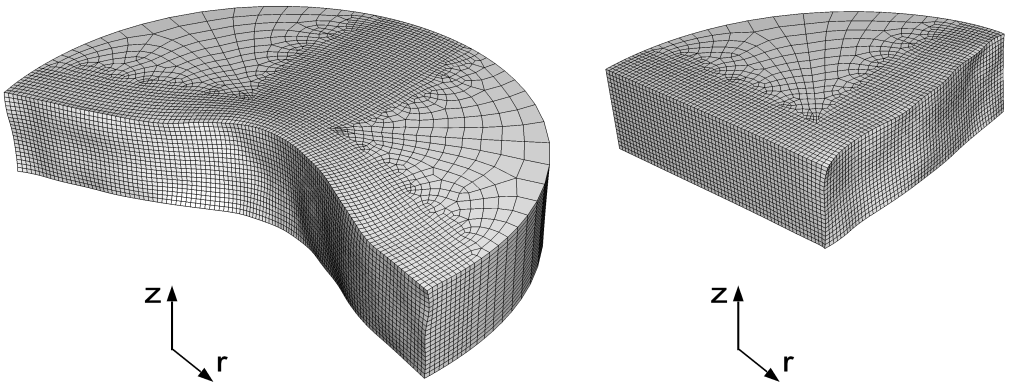

(a) (b)

Figure 7.15 *– FE model of 316L disk deformed into opposite of measured shape in order to calculate original residual stresses: (a) after the first cut and (b) after the second cut, Deformation magnified by 300.*

7.2.2.1 Second cut

After the first, one of the two halves of the indented disk B was cut another time in two using the same EDM machine and the same condition used for the first cut, as described before, along a plane normal to the first cut plane (see Figure 7.16).

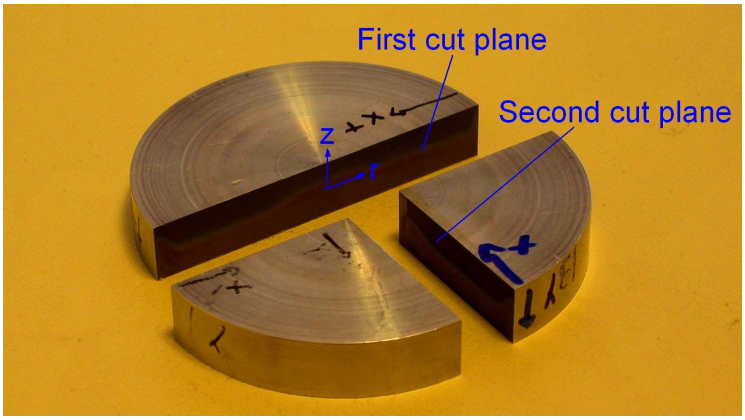

Figure 7.16 *– Indented disk B cut two times along the first cut plane and the second cut plane respective;y*

After cutting, the two quarter of the disk B were removed from the clamping fixture. The contours of both cut surfaces were measured by the same laser scan machine and setting used to scan the first cut surfaces (see Subsection 7.2.1). The specimen was scanned using rows separated by 0.1 mm in the z direction with data points within a row sampled every 0.05 mm, giving about 63.400 points on each cut surface.

The measured contours were processed using the same procedure described in Subsection 7.2.2. The resultant average contour is shown in Figure 7.17. The peak-to-valley amplitude is about 10 μm.

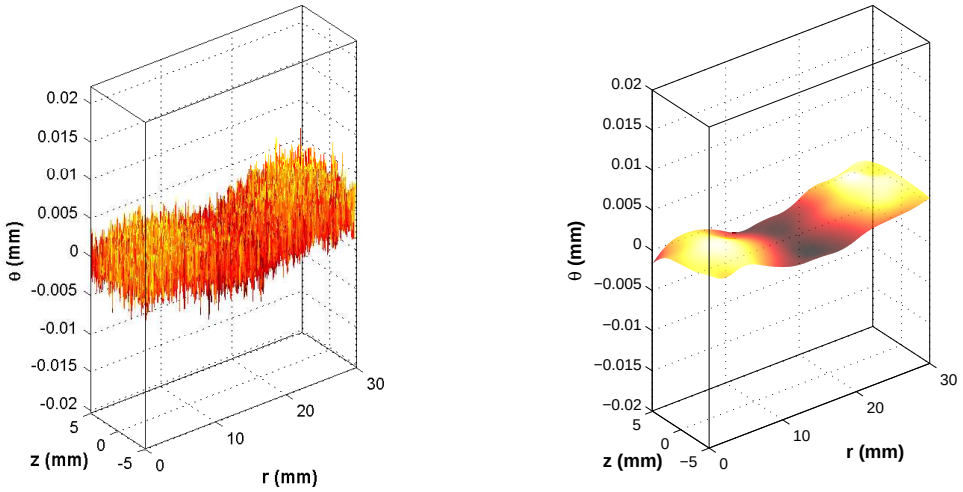

(a) (b)

Figure 7.17 – *(a) Average contour of the second cut surfaces in the indented disk B and (b) its spline fit.*

As described before, the σ_θ hoop stresses that were present on the second cut plane after the execution of the first cut (step B in Figure 2.2) were calculated numerically by elastically deforming the second cut surface into the opposite shape of contour that was measured on the same surface. This was accomplished using half of the 3-D FE model used in the previous analysis (see Figure 7.15(a)) and it is showed in Figure 7.15(b), by using the removing elements command in the second step of the previous FE analysis. The same fitting method was used to smooth the measured surface.

7.2.3 Results

In order to get the optimum amount of smoothing, an uncertainty estimation as the one described in [2] was carried out. The parameter that determines the amount of smoothing versus the amount of detail in the fit is the spacing between the knots in the splines, where the knots are the points where the piecewise polynomials are joined. The amount of smoothing was objectively chosen by minimizing an estimate of the uncertainty in the calculated stresses. It was expected that there would be an optimum amount of smoothing: an overly smooth fit (too coarse knot spacing) would fail to capture the features in the surfaces, and an overly detailed fit (too fine knot spacing) would unnecessarily capture noise in the data. Selecting the amount of

smoothing based on the data fit alone would be simpler because it does not require multiple FE calculations. However, minimizing uncertainty in the stresses could only be achieved by calculating the stresses for different data smoothing.

In this case, the approach to determine the optimum spline smoothing involves incrementally increasing the knot density and calculating the stresses for each increment. First, a single interval bounded by two knots, was used in the shortest dimension on the diametral section (z-direction). The knots in the ,r, radial direction are chosen to have an integral number of intervals giving the spacing closest to that in the z-direction. Using this knot distribution, the stress map is calculated with the FE model. This process was repeated with refined knot spacing by adding another interval in the z-direction and a proportional number in the r-direction, and the stress calculation was repeated with the new data fit. The uncertainty, $\partial\sigma$, in the calculated stresses at a given node was estimated by taking the standard deviation of the new stress and the stress from the previous, coarser fit. This standard deviation of two values is given by:

$$\partial\sigma(i,j) = \frac{1}{\sqrt{2}}|\sigma(i,j) - \sigma(i,j-1)| \tag{7.1}$$

The same uncertainty analysis was executed for all the contour method applications (disk A, B, C and D). Figure 7.18(a) shows the uncertainty estimate in the calculated stresses and data fit error only for the indented disk A ,for brevity.

Further confidence in selection of the optimal smoothing can be provided by examining the behavior of the interior extrema in the calculated stress map. Figure 7.18(b) shows how the peak compressive residual stress in the calculated stress maps varies with knot number for the indented disk A and B.

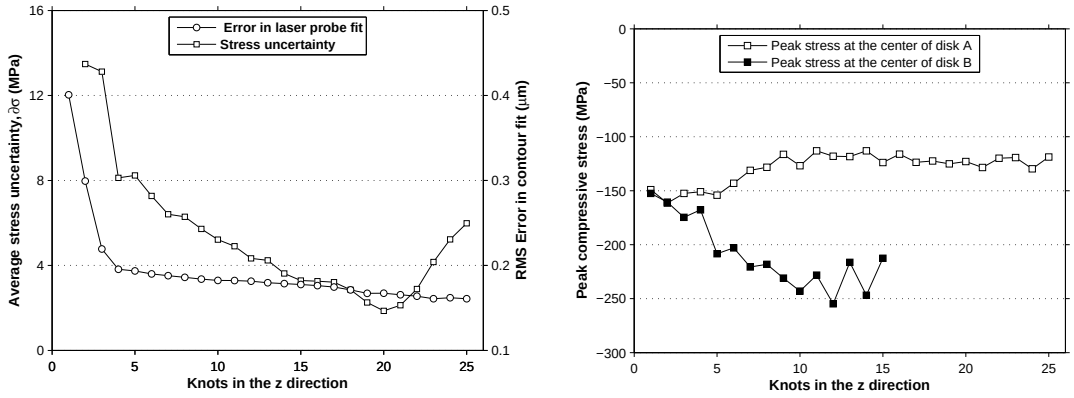

(a) (b)

Figure 7.18 *– (a)Uncertainty estimate in the calculated stresses and data fit error and (b) peak compressive stress for the indented disk A.*

After the uncertainty analysis, it was chosen as optimal smoothing four knot in z direction for the indented disk A and three for the indented disk B, both first and second cut contours. It was chosen the knot number corresponding with the elbow of the RMS error curve and because the uncertainty exhibits a local minimum for that value. The corresponding smoothed contours were applied as boundary conditions on the FE model described in the previous section. Figure 7.19(a) and Figure 7.19(b) show the maps of the residual hoop stresses along the diameter plane for the indented disk A and the indented disk B respectively.

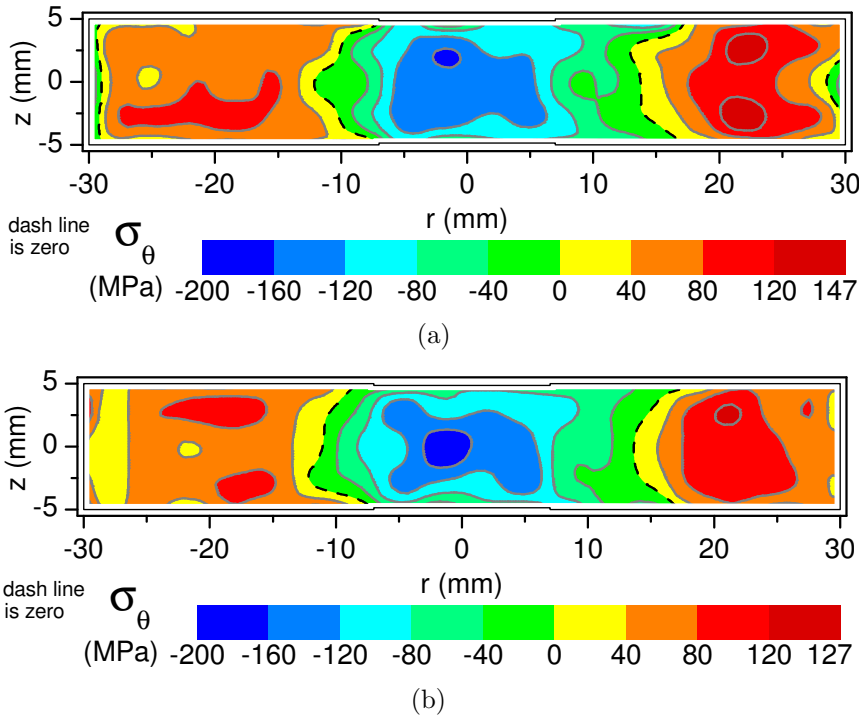

Figure 7.19 – *Maps of hoop residual stresses measured with the contour method: (a) on the indented disk A (cut executed with 50 μm diameter tungsten wire); (b) on the indented disk B (cut executed with 50 μm diameter tungsten wire).*

Figure 7.20 shows the the hoop residual stress along the second cut plane, that is normal to the first cut plane. These stresses are different from the stress measured on the first cut plane, becasue they are relaxed by the first cut. In order to obtain the original residual hoop stresses that are present in the disk before the execution of the first cut, it is needed to combine the this stresses with the stress variation on the second cut plane already calculated with the first cut contour application. The detail of this superposition and its results will be described later in Chapter 10.

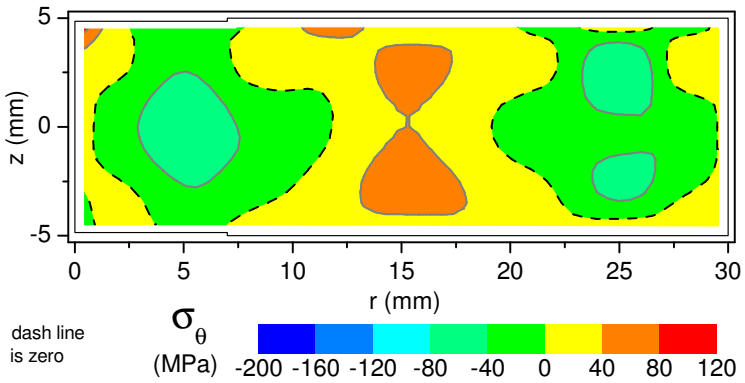

Figure 7.20 – *Residual stresses σ_θ in 316L disk B after the second cut (step B=E in Figure 2.2) measured by the contour method on the second cut plane.*

7.2.4 Comparison with FE prediction and Neutron Diffraction Results

Figure 7.21 compare the hoop residual stresses measured with contour method (CM) on both disk A and B with the ones measured by neutron diffraction (ND) on disk A for $z = \pm 1.65$ mm, $z = \pm 3.3$ mm and $z = 0$ mm (mid-thickness line) respectively. The agreement is excellent in spite of the fundamental differences in the measurement methods. The excellent agreement further confirms the ability of each method to map residual stresses and also the good repeatability of the contour method. In fact, the two contour method tests executed in two different indented disks, gave the same residual stress map, even though for the disk A a contour correction was needed, because of the 50 μm wire.

Then, there is an excellent agreement of both experimental results, contour and neutron, with the FE prediction, showed also by Figure 5.5 at pag. 41. So, in order to serve as an ideal test specimen, the stresses in the indented disk would be calculated to sufficient accuracy with the FE model and not require independent measurement.

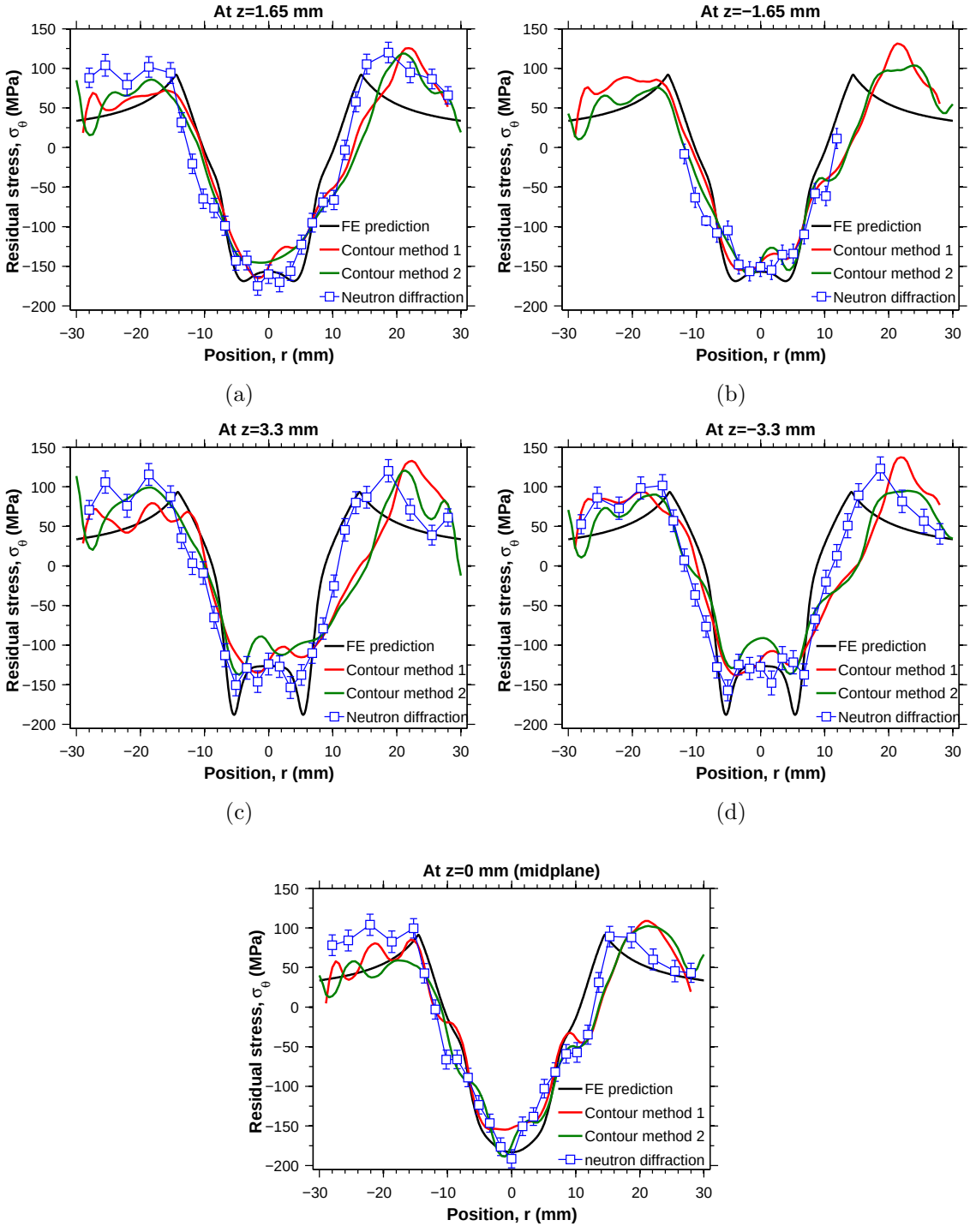

Figure 7.21 – *Hoop residual stresses, σ_θ, measured with contour method, in both steel disks A (1) and B (2), and neutron diffraction plotted with the FE prediction for $z = 0$ mm (mid-thickness line), for $z = \pm 1.65$ mm and for $z = \pm 3.3$ mm respectively.*

7.3 ALUMINUM 2024-T351 DISKS

In this section it is presented the application of the classical method to a aluminum 2024-T351 disk indented as described in Subsection 3.4.2.

7.3.1 Experiment

The contour method was applied to an indented disks and, as a control, to an unindented disk. The conventional contour method was applied to measure the hoop stress over a diametrical cross section.

The disks were cut in half along a diameter plane using the same EDM machine described before in Subsection 7.2.1. A 100 μm diameter brass wire, and Epak 413, skim cut 2 for 1/4 in. thick steel settings, and adaptive control were used for these cutting. Each 60 mm cut took about 3.5 hours. Both disks were cut submerged in temperature-controlled deionized water throughout the cutting process. The parts were constrained by clamping on both sides of the cut to the work plate of the EDM machine (see Figure 7.9), as described before.

After cutting the disks, the contours of the resulting four surfaces of the disk (indented and not-indented) halves were measured using the same laser machine (see Subsection 7.2.1) used to scan the 316L stainless steel disks B and D. The cut surfaces were measured using rows separated by 0.1 mm in the axial direction, z, with data points within a row sampled every 0.04 mm, giving about 113.000 points on each cut surface.

7.3.2 Calculation

The raw data was processed using the procedure described in Subsection 7.3.3. Figure 7.22 shows the average of the contours measured on the two opposing surfaces created by the cut for the blank disk (Figure 7.22(a)) and the indented disk (Figure 7.22(b)) respectively. The peak-to-valley amplitude of the contour is about 10 μm for the blank disk and 35 μm for the indented disk. In spite of the low elastic modulus of the aluminum, the contour is even smaller than the steel one, in term of peak-to-valley amplitude.

The σ_θ stresses that were originally present on the cut plane were calculated numerically by elastically deforming the cut surface into the opposite shape of contour that was measured at the same surface as described before (see Subsection 7.3.3). This was accomplished using the same 3-D elastic finite element model used before (see Figure 7.15(a)). The material behavior was considered elastically isotropic with an elastic modulus of 73.2 GPa and a Poisson's ratio of 0.33. Then the data were

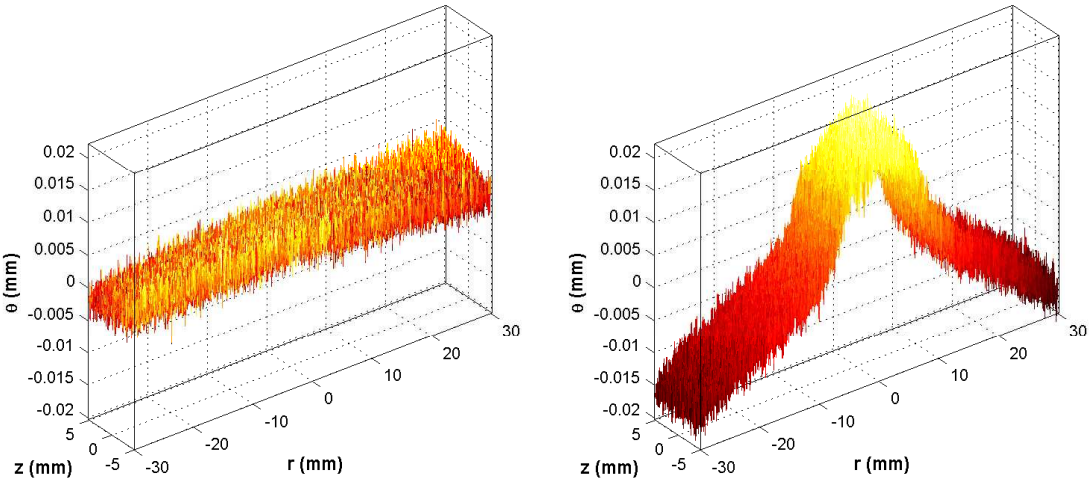

(a) (b)

Figure 7.22 – *Measured contour on the cut surface for the AA2024-T351: (a) blank disk; (b) indented disk.*

fitted using the same approach as before and were evaluated at a grid corresponding to the FE nodes, and those values at the nodal locations were then used as displacement boundary conditions.

7.3.3 Result

The same uncertainty analysis described before was executed (see Subsection 7.2.3). It was chosen as optimal smoothing three knots in z-direction for the indented disk. The corresponding smoothed contour was applied as boundary conditions on the FE model described in the previous section. Figure 7.23 shows the map of the residual hoop stresses along the diameter plane for the aluminum 2024-T351 indented disk.

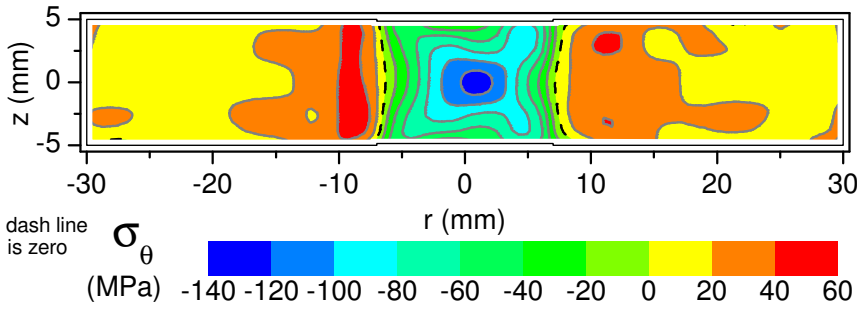

Figure 7.23 – *Maps of hoop residual stresses measured with the contour method on the AA 2024-T351 indented disk.*

Figure 7.24 shows the comparison between hoop stress measured with the contour method for $z = 0$ mm (mid-thickness line) compared with the FE prediction.

The trends of the measured and predicted stress are pretty similar, but there is a difference up to 75 MPa in the peak compressive stress on the center of the disk. The FE prediction is not very accurate. Since the hardening model was calibrated on the experimental curves of the in-plane directions, probably the hardening behavior in the through-thickness direction affects the residual stress distribution.

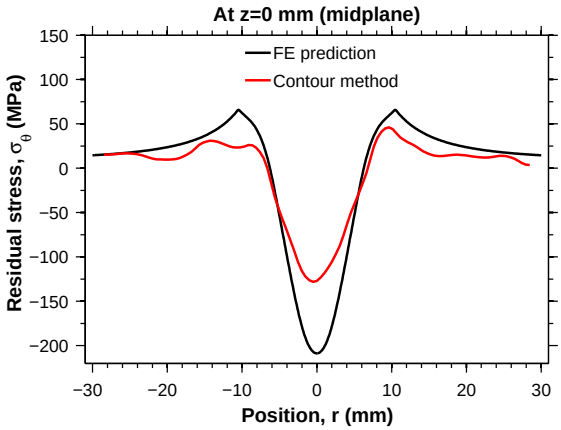

Figure 7.24 – *Hoop residual stresses, σ_θ, measured with contour method in the aluminum 2024-T351 plotted with the FE prediction for $z = 0$ mm (mid-thickness line).*

Chapter 8

Experiment: X-ray Diffraction

In order to validate the surface superposition principle the remaining in-plane stresses on the cut surface were measured after the application of the contour method on the 316L stainless steel disk, by means of a X-ray diffraction technique. But unfortunately this test was not successful because of the big grain size of the steel used.

8.1 PRINCIPLE OF X-RAY STRESS MEASUREMENT

When a monochromatic X-ray beam irradiates a solid material, it is scattered by the atoms composing the material. For a perfect crystalline material, atoms are packed regularly into a three-dimensional periodic lattice. The distance between crystallographic planes is perfectly defined and it is a characteristic of a material in a given environment. Because of the regular distribution of atoms, the scattered waves lead to interferences similar to visible light diffraction by an optical diffraction pattern. The intensities of scattered waves sum up into a constructive interference when the condition

$$2d \sin \Theta = n\lambda \tag{8.1}$$

is fulfilled (see Figure 8.1), where d is the distance between diffracting lattice planes, Θ is the angle between the incident beam and the diffracting planes, λ is the X-ray wavelength and n is an integer. If this condition, called *Bragg's Law*, is fulfilled, the diffracted beam and the incident beam are symmetrical in relation to the lattice planes normal. As can be seen in Figure 8.1, an infinity of crystallographic planes can be defined, however, for physical reasons, only several of them lead to a diffraction pattern with a detectable intensity.

When an X-ray beam irradiates the surface of a crystalline material, it is constructively scattered only if it meets lattice planes oriented to fulfill Bragg's law. If

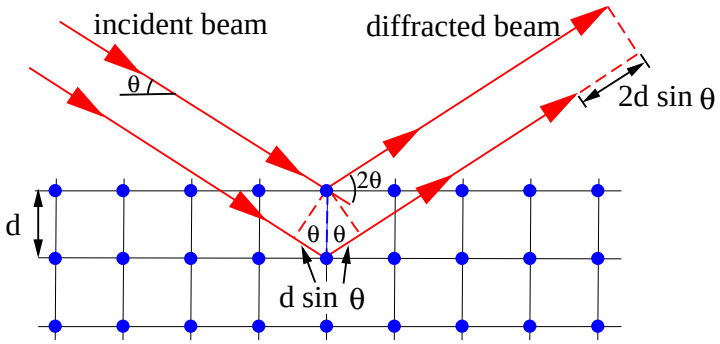

Figure 8.1 *– Bragg's Law – X-ray diffraction can be observed in θ-direction if $n\lambda = 2d \sin \Theta$.*

the material is composed of many grains (crystallites) randomly oriented, there is always a group of them suitably oriented to produce a diffracted beam. Because of the random distribution of crystallites has a rotational symmetry, several cones of diffracted beams with the incident beam as the axis can be observed, each of them corresponding to a specific lattice plane. Diffraction cones can also be observed but only on one side (back scattering pattern) because the specimen is massive and the penetration depth of X-rays usually used do not exceed 30 or 40 μm. The summit angles of these cones are:

$$\alpha_i = \pi - 2\Theta_i \tag{8.2}$$

where Θ_i are the diffraction angles related to the lattice spacing d through the Bragg's law. if these angles can be measured by an appropriate device, it is then possible to know the lattice spacing d of the analyzed crystallographic planes. This is only a brief introduction to diffraction phenomena and extensive information on theoretical and experimental aspect can be found in [45,46,47,48,49,50].

In a polycrystalline (metal or ceramic) part, with fine grain and stress-free, the lattice spacing d_0 for a given plane family does not vary with the orientation of these planes. If the specimen is stressed, due to elastic deformation, the lattice spacing varies according to the orientation of planes relatively to the stress direction. If a tensile stress is applied, the lattice spacing will increase for planes perpendicular to the stress direction and decrease for planes parallel to the stress direction (due to Poisson's ratio effect). The elastic strain of the crystal lattice can be inferred from the variation of the lattice spacing $d - d_0$, measured by the position of the diffraction peak (Bragg's law):

$$\varepsilon = \frac{d - d_0}{d_0} \tag{8.3}$$

Thus, the crystal lattice (crystallographic planes) is used as a strain gage which can be read by diffraction experiments. As in any extensometric method, the stress can be calculated from strains measured in several directions and the elasticity constants of the material.

A diffraction peak is the result of X-rays scattering by many atoms in many grains, so a change in the lattice spacing will result in a peak shift only if it is homogeneous over all these atoms and grains, i.e., over all the irradiated volume. Thus, the strain determined from peak shift measurement is representative of a macroscopic elastic strain (applied or residual). On the other hand, all the crystal defects (dislocations, vacancies, stacking faults etc.) lead to a local fluctuation of the lattice spacing which results in a peak broadening.

8.2 EXPERIMENTS

X-ray diffraction (XRD) measurements were made using two types of goniometers at the High Temperature Materials Laboratory, Oak Ridge National Laboratory. Table 8.1 lists the details of the experimental conditions for the x-ray measurements using the first unit. Briefly, a 4-axis (ϕ, χ, Ω, 2Θ) goniometer [51] was employed for the stress measurements using the "ψ-goniometer geometry" (see Figure 8.3(a)) [49]. The (220) and (311) reflections from the 316L austenitic steel were utilized for the strain measurement along the length of the samples using Cr K_α and K_β radiations, respectively. Measurements were restricted to a 4×4 mm area by using Pb tape for masking. Given the large grain size (50-100 μm), rocking scans were performed at each nominal tilt to locate four low intensity regions; that is, sample orientations where there is minimal contribution to the intensity from a large grain or grains. The detector scans were then performed at fixed ϕ, $\psi(=\chi)$ and Ω. Additional scans were made at each of the nominal ψ values, i.e., ψ at $\pm 0.2^\circ$ for a total of twelve scans per nominal ψ.

Specimen alignment was accomplished using a dial gauge probe which was accurate to ± 5 μm. Here, the relative distance to the center of rotation is known, and the diffracting surface is positioned accordingly. Goniometer alignment was ensured by examining LaB_6 powder on a zero background plate. The maximum observed peak shift for the (510) reflection of LaB_6 (141.7° 2Θ) was less than $0.01^\circ 2\Theta$ for Ψ tilting as described in Table 8.1.

The stresses were calculated using the Dölle-Hauk method [49], assuming a bi-

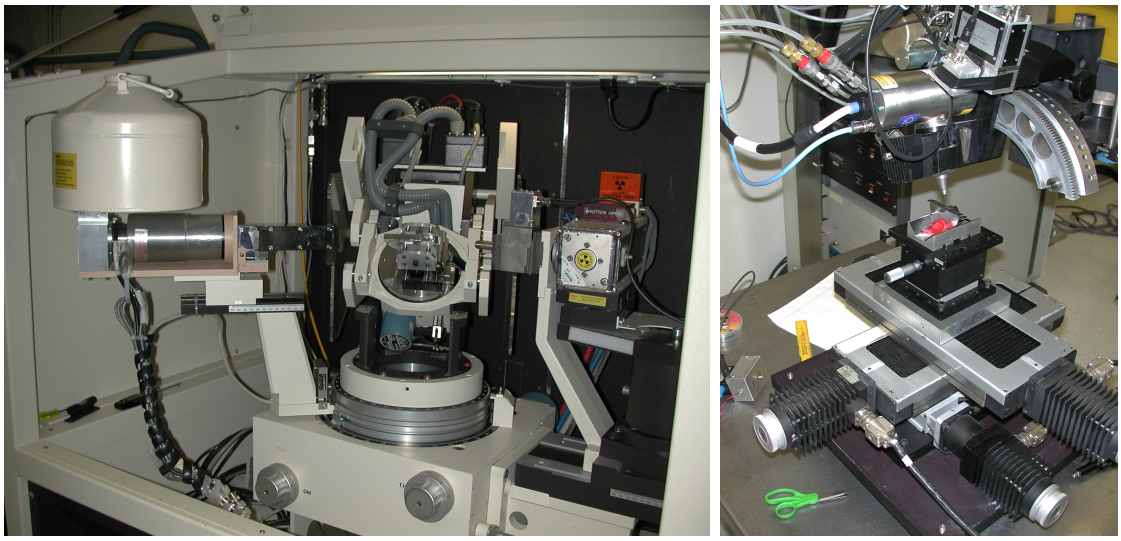

(a) (b)

Figure 8.2 *– (a) ψ-goniometer geometry and (b) Ω-goniometer geometry for residual stress measurements.*

axial stress state. For this stress state, the equation relating strain to stresses is:

$$\epsilon_{\phi\psi} = \frac{d_{\phi\psi} - d_0}{d_0} = \frac{1+\nu}{E}\sigma_\phi \sin^2\psi - \frac{\nu}{E}(\sigma_{11} + \sigma_{22}) \tag{8.4}$$

assuming $\sigma_{13} = \sigma_{23} = \sigma_{33} = \phi = 0$. ϵ, d, ν, E and are the strain, interplanar spacing, Poisson's ratio, Young's modulus and stress, respectively. Poisson's ratio and Young's modulus were taken as 0.3 and 193 GPa, respectively. The variables

Table 8.1 *– Experimental conditions of the x-ray measurements 4-axis (ϕ, χ, Ω, 2Θ) goniometer.*

Parameter	**Condition**
Equipment	Scintag PTS goniometer Spellman DF3 series 4.0 kW generator Scintag liquid N_2-cooled Ge detector
Power	1.44 kW; 40 kV, 36 mA
Radiation	Cr, λ $K_\alpha = 2.28970$ Å, $K_\beta = 2.08487$ Å
Incidence slit divergence	0.24°
Receiving slit acceptance	0.25°; radial divergence limiting (RDL) Soller slit
Source to specimen distance	290 mm
Specimen to back slit distance	290 mm
Mask and mapping locations	4×4 mm Pb mask, R=0 and 25 mm
Tilt axis and nominal tilt angles	Ω; 0°, ±28.2°, ±42°, ±55° (equal steps of $\sin^2\Psi$)
Scans	0.02°2Θ/step

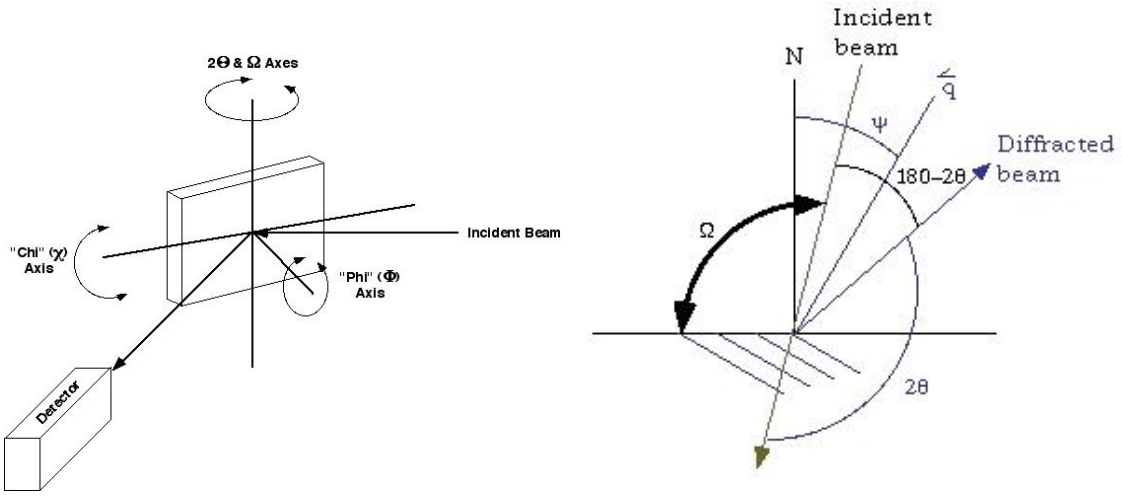

(a) (b)

Figure 8.3 *– (a) ψ-goniometer geometry and (b) Ω-goniometer geometry for residual stress measurements.*

and subscripts ϕ, ψ and 0 refer to the azimuthal angle, tilt angle and strain-free, respectively. $d_{\psi=0}$ was taken as the strain free interplanar spacing, d_0.

Table 8.2 lists the details of the experimental conditions for the x-ray measurements on a second unit. Briefly, a single axis (ψ) goniometer [52] was employed for the stress measurements using the "Ω-goniometer geometry" (see Figure 8.3(b)) [49]. The (311) reflection from the austenitic steel was utilized for the strain measurements. During scanning, the axis was oscillated $\pm 4^\circ$ to improve particle statistics. Specimen alignment was accomplished using a contact probe which was accurate to ± 0.25 mm. Goniometer alignment was ensured by examining a stress-free Fe powder pellet. The maximum observed peak shift for the (211) reflection of Fe (156° 2Θ) was less than 0.06° 2Θ for tilting as described in Table 8.2.

This data was analyzed with the RSA software [53], and the stresses were also calculated using the "$\sin^2\psi$" technique [49].

A typical peak profile of the 316L disk contained peaks from two or more grains or sets of grains (see Figure 8.4(a)). The blue and green curves in Figure 8.4(a) show the presence of two peaks for different 2θ). In an effort to avoid such peaks, the available diffracting grains were prescreened via the rocking curves described above. Scans from a particular Ω orientation and nominal ψ were then averaged and profile fit, reducing the 12 scans to four profile fit peak positions per nominal ψ. Any scans revealing any obvious "multi-grain" nature, as shown below, were excluded. The resulting ϵ versus $\sin^2\psi$ is shown in Figure 8.4(b). Despite our best efforts to average and minimize the influence of the large grains (see Figure 3.3), this typical $\sin^2\psi$ plot shows lots of scatter due to interaction strains or elastic incompatibility strains

Table 8.2 *– Experimental conditions of the x-ray measurements 4-axis (ϕ, χ, Ω, 2Θ) goniometer.*

Parameter	**Condition**
Equipment	TEC Model 1600 x-ray stress analyzer Position sensitive detector (PSD), 14° 2Θ range
Power	52.5 kW; 35 kV, 0.75 mA
Radiation	Cr, λ $K_\beta = 2.08487$ Å
Source to specimen distance	220 mm
Specimen to back slit distance	220 mm
Collimator	5 mm diameter
Mask and mapping locations	4×4 mm Pb mask, R=0 and 25 mm
Tilt axis and angles	Ω; ψ-value varied ±40° in equal steps of $\sin^2\Psi$)
Scans	0.06°2Θ/step from 142-156°2Θ; 180 sec/scan

between grains. While each individual strain measurement is valid and correct, the heterogeneity displayed indicates that it is not prudent to force the x-ray residual stress analysis further.

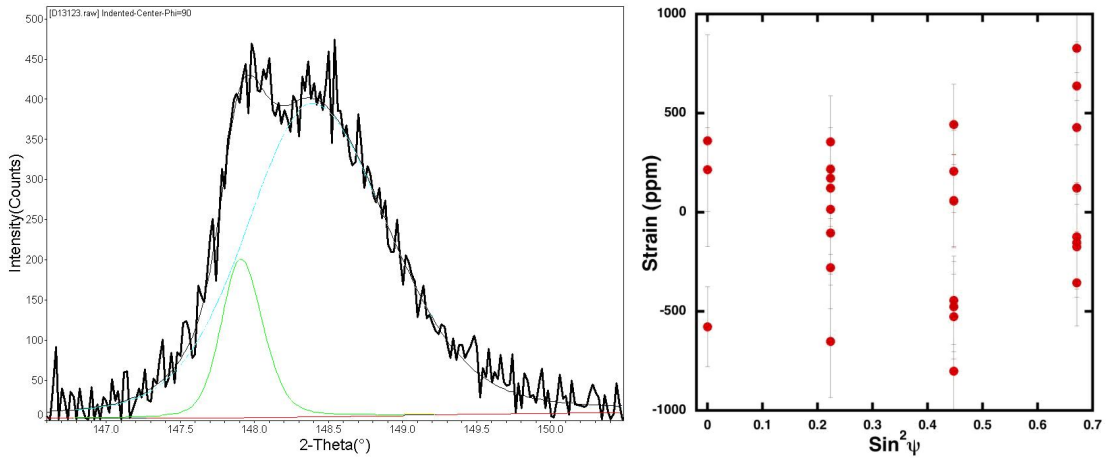

(a) (b)

Figure 8.4 *– (a) Typical (311) profile and (b) typical ϵ vs $\sin^2\psi$.*

Chapter 9

Experiment: ESPI Hole-drilling

In order to validate the surface superposition principle the remaining in-plane stresses on the cut surface were measured after the application of the contour method on the 316L stainless steel disk and the aluminum 2024-T351, by means of the ESPI hole drilling method.

9.1 INTRODUCTION TO ESPI HOLE DRILLING

The hole drilling technique for residual stress measurement was introduced in 1933 by Mathar [54], and is a common technique used today. It is by definition a *destructive* method, not because it necessarily destroys the part by drilling the hole, but because it removes material, therefore destroying the stress support.

In the hole drilling method, a specific amount of material is removed, and the resulting measured deformation (or strain) is used to determine the average stress. Extensions of this technique allow to drill the hole in several increments, thereby obtaining some information about the stress as a function of depth; these techniques are standardized in ASTM 837 [55]. The standard drilling method is to use an air turbine with speeds from 20-60.000 rpm, using bits of the order of 1.6 mm diameter. Other techniques for removing the material include particle erosion, laser annealing or scratching. The standard method for measuring the relieved strain is to use a strain gage. In the mid 1980s, Antonov [56] and McDonach [57] showed that optical techniques could be used for surface displacement measurements around drilled holes. In the mid-90s, Nelson [58] detailed his earlier results, and gave a general theory for capturing a deformation map using holographic interferometry. Another technique to measure the surface displacement produced by the hole drilling is to use ESPI to collect full field of view data and store it electronically, so the data analysis can be performed by a computer algorithm [59,60]. This process is rapid and can provide some statistics to help quantify the accuracy of the answer. In addition to a rapid, automated algorithm for deformation data acquisition and residual stress

calculation, a system has been developed that incorporates software for controlling the drilling equipment, resulting in a fully integrated residual stress measurement system, which is fully described by Steinzig et ali [61,62,63,64].

Electronic speckle pattern interferometry (ESPI) can produce data about displacements (shape changes) at the surface of an object by mathematically combining interferograms registered digitally before and after the deformation occurs. In a single beam ESPI system the object is illuminated with coherent light (a green laser in our case) and viewed by a CCD camera through a lens system and a prism that interferes the object light with a reference beam from the laser source (Figure 9.1).

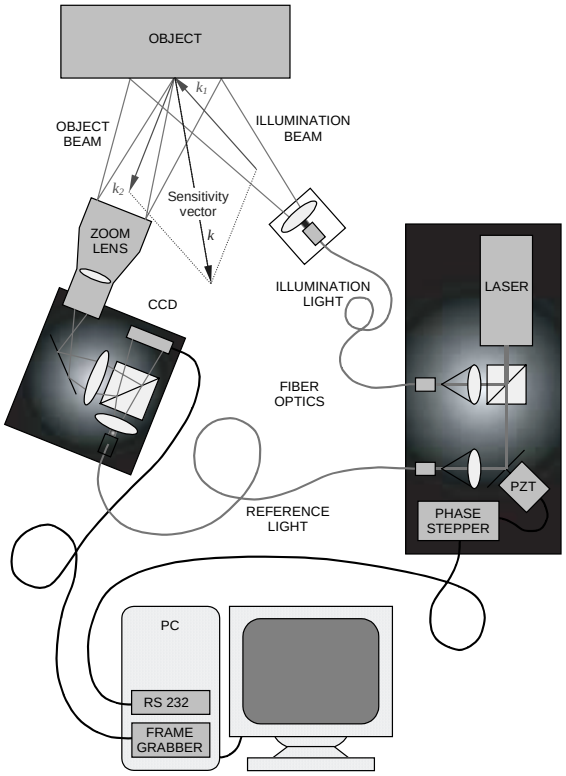

Figure 9.1 *– Schematic diagram of the ESPI setup (reproduced from Steinzig and Ponslet [61])*

The interference image is recorded by the CCD camera and stored in a computer for processing. A raw image by itself does not contain useful information, but rather exhibits a random-looking pattern of light and dark speckles, caused by the roughness of the sample and the optics, as shown in the first 8 images of Figure 9.2. To obtain quantitative information, images taken before and after a deformation event are stored in a computer and processed. There are several techniques available to perform this processing. In this case it is used a technique known as a four-bucket phase-stepped algorithm. It requires two sets of four images each. One set is taken

before the object is deformed (*reference set*), the other is taken after the deformation has occurred (*deformed set*). Within each set, the reference phase (reference beam) is stepped by a 1/4 wave (90 degrees) between one image and the next. This can be achieved in a number of ways. The system described here uses a small mirror bonded to a piezoelectric actuator and driven by electronic circuitry synchronized with the frame grabbing hardware.

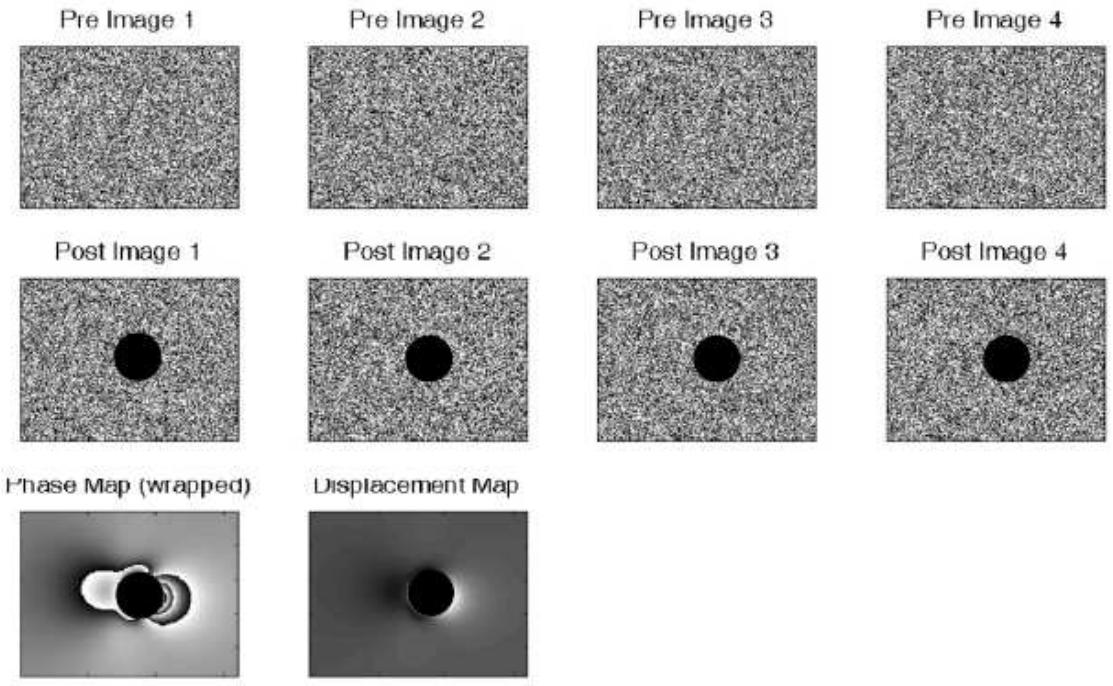

Figure 9.2 *– Set of four pre-hole and four post-hole raw images and the resulting phase (wrapped) and displacement (unwrapped)maps; the black disk shows the location of the hole.*

Once acquired, the reference set and the deformed set are used to calculate a phase image of the surface displacement projected along the sensitivity vector of the system. The phase image will generally exhibit a number of discontinuities resulting from the arc-tangent operation used in calculating the phase angle. These discontinuities can be removed using phase-unwrapping algorithms, for which a good source is the book by Ghiglia and Pritt [65].

The ESPI technique is well documented elsewhere [66,67,68,69] and will be only briefly summarized here. Figure 9.1 schematically shows a typical ESPI setup. The light from a laser source is split using a half-silvered mirror. One part passes through a piezoelectric actuator to provide a phase-stepped reference light to a CCD camera. The other part of the laser light (the *illumination beam*) is used to illuminate the

specimen, which is imaged (the *object beam*) through a zoom lens onto the CCD. The object beam interferes with the reference light to produce a speckle pattern on the CCD, the local phase of which varies with displacement of the specimen surface. By taking a series of phase-stepped images before and after surface deformation, it is possible to evaluate both the size and sign of the deformation at every pixel in the CCD image. The data at each pixel correspond to the component of the three-dimensional surface deformation in the direction of the *sensitivity vector*. This vector bisects the directions of the illumination and object beams. In the present application, the image contains the area around the drilled hole, and the measured deformations are those caused by hole drilling.

After processing the light intensity data from the CCD, the ESPI system returns a pixel map of the surface displacements along the sensitivity direction. The rest of the analysis consists of a least square fit of a linear combination of the uniaxial stress cases obtained from FE calculation [62] with the experimental data. Then the portion of the data covering the hole and an annular region around the hole is removed because that data have been corrupted by the drilling operation. Although the deformations are largest near the hole, we have found that the FFLSQ technique has inherently low sensitivity to noise so that masking large regions of high amplitude data has little effect on the final result.

Next, the code generates three basis functions for the particular h/D value of the test from the polynomial expansions available in the database (see [62]). This results in three maps of 3D data (x, y, and z deformation for each of the three uniaxial states of stress σ_{x0}, σ_{y0} and τ_{xy0}). The code then calculates the sensitivity direction of the actual test based on user-provided configuration data and projects the numerical displacement maps onto that direction. This reduces the amount of FE data to three square grid maps (one for each uniaxial state of stress) of 1-D data (deformation along the test sensitivity direction).

Those data are then scaled and interpolated onto the pixel grid that corresponds to the test data. The adjustments for hole diameter and Youngs modulus are then made [62]. This results in three projected displacement pixel maps of model data, one for each uniaxial stress case.

Finally, those data are arranged into least squares fit (or pseudo-inverse) formulation, which is solved to provide the best fit of stress components. Without rigid body correction (see Section [62]), the least squares calculation requires the pseudo-inversion of a system of up to 307.000 equations (640×480) with three unknowns (σ_x, σ_y and τ_{xy}). In practice however, with a 640×480 pixel image and a 200% mask around the hole, the size of the system is typically around 240.000 by 3.

9.2 EXPERIMENTS AND RESULTS

In order to measure the in-plane remaining radial and axial stresses, on the cut surface, i.e. relaxed by the execution of the cut, several ESPI hole drilling tests were executed on the 316L stainless steel and aluminum 2024-T351 indented and unindent disk halves using the the PRISM-RS system (see Figure 9.3) described by Steinzig and Ponslet [63] at the Hytec Incorporated, Los Alamos, New Mexico [70] . The cut surfaces of the disks were previously electro-polished in order to remove the EDM-affected layer of material where high residual stress are present.

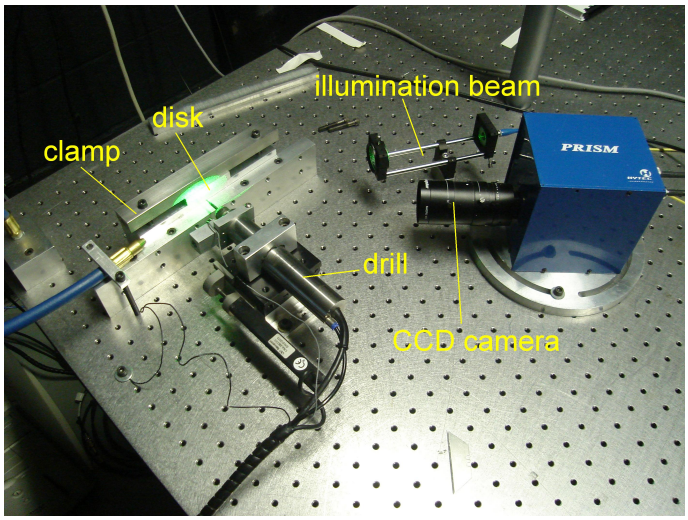

Figure 9.3 – *PRISM-RS setup: illumination beam, CCD camera, drill, disk and clamp.*

The system was set up to make measurements in the half disk cut surface along the mid-thickness line. The drilling and holography systems remained stationary during these tests, and the sample was translated in a clamping fixture. Using this setup, 9 measurements were made in the 316L stainless steel indented disk which distance from each other was of 6 mm along the mid-thickness line, using a 1.59 mm (1/16") diameter drill bit in four increments of 0.1 mm till a final depth of 0.4 mm. The first 4 holes, for $r > 0\ mm$, where executed at a rotational speed of 30.000 rpm , while for the last 5 holes, for $r \leq 0\ mm$, the rotational speed was 15.000 rpm.

The residual stress were evaluated using the incremental hole analysis [71,72] adapted for to the ESPI hole drilling.

Figure 9.4(a) and 9.4(b) show the radial and axial stresses respectively along the mid-thickness line plotted for each analysis increments. These stress values are not the average stresses over the incremental depth but they come from the incremental analysis. The figures show also for comparison the FE prediction of

these stresses after the relaxation caused by the cut. The first increment stresses are very high because the 0.1 mm layer is still affected by the EDM stresses or by the drilling process or by the surface resulting from the electro-polish. Instead the second increment (0.2 mm) and the others pretty similar to each other and very close to the FE prediction but only for $r \leq 0$ mm, i.e. the holes executed at 15.000 rpm. Subsequent measurements executed on the electro-polished cut surface of the unindented disk showed accurate and repeatable results using 15.000 rpm and a 0.05 mm/s feed rate. So, the previous measurements erroneously executed using 30.000 rpm were not considered for the subsequent surface superposition verification presented in the Chapter 11.

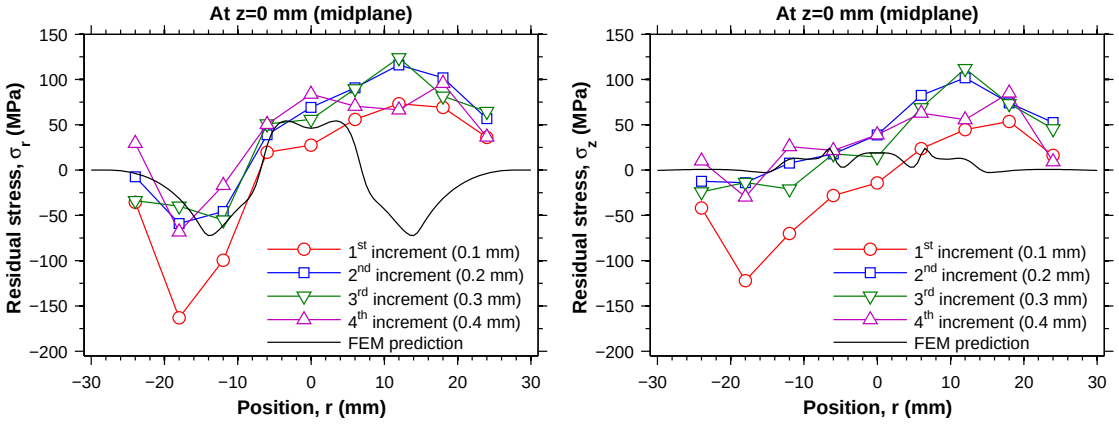

Figure 9.4 – *Measured (a) radial and (b) axial stresses in the 316L indented half disk along the mid-thickness line for every increments together with the FE prediction.*

Then, using the same experimental setup, several measurements were executed on the electro-polished cut surface of the aluminum 2024-T351 indented half disk. In detail, 9 holes were executed along the mid-thickness line every 6 mm in the same conditions (rotational speed, drill diameter, etc.). Further 10 measurements were executed in between the previous executed holes using a smaller drill bit (0.79 mm or 1/32") and rotational speed of 10.000 rpm, instead increments and final depth were the same as before.

Figure 9.5(a) shows the radial stresses along the mid-thickness line plotted for each increments for 1.59 mm hole diameter measurements and Figure 9.6 for 0.79 mm hole diameter ones, and Figure 9.6(a) and 9.6(b) show the axial residual stress for the two different hole diameter measurements respectively, plotted together with the FE prediction. The measured stresses for both set of measurements are very low and there is no much difference between each increments. Further the difference

between the measurements executed using different drill diameter are low.

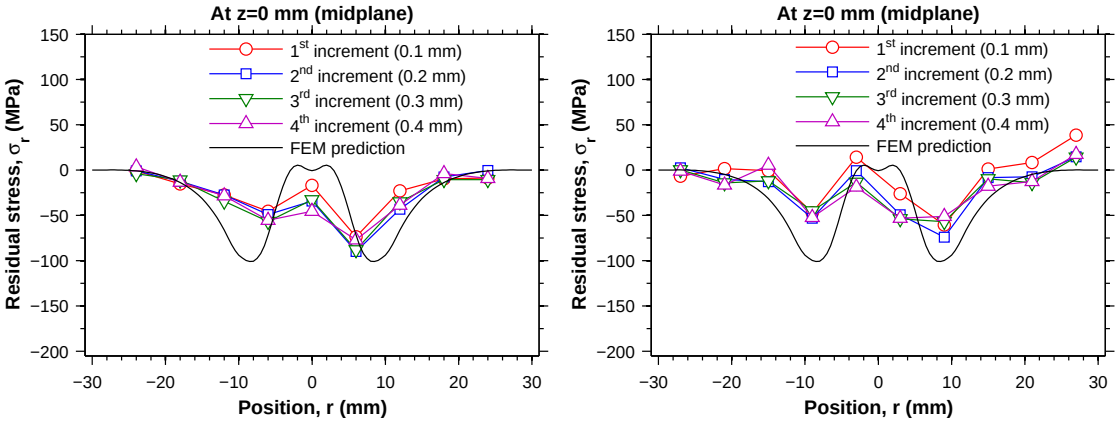

Figure 9.5 – *Measured radial stresses (a) with 1.59 mm drill and (b) with 0.79 mm drill in the aluminum 2024-T351 indented half disk along the mid-thickness line plotted for every increments.*

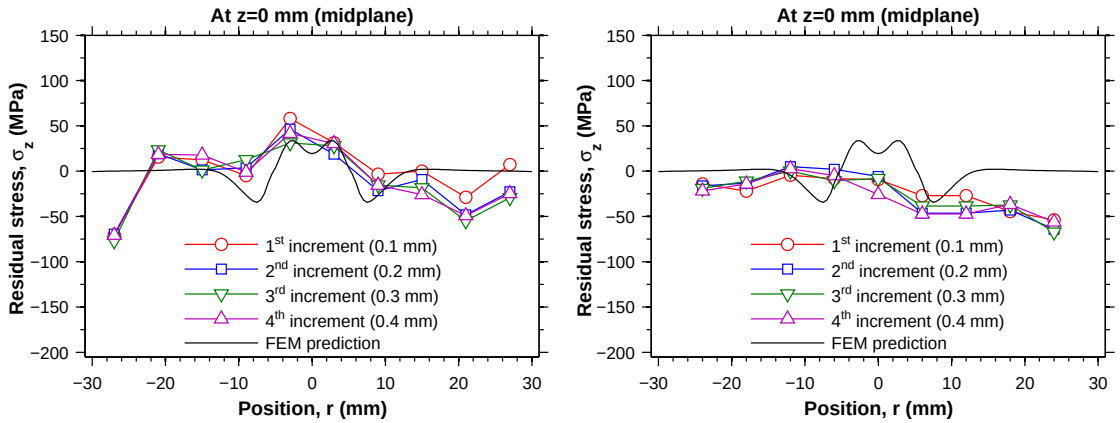

Figure 9.6 – *Measured axial stresses (a) with 1.59 mm drill and (b) with 0.79 mm drill in the aluminum 2024-T351 indented half disk along the mid-thickness line plotted for every increments.*

Chapter 10

Results: Multiple Cuts

In this section it will be presented the application of the multiple cut theory to the HSLA-100 quenched plate and to the 316L indented disk, which contour method applications were described in Section 7.1 and 7.2 respectively.

10.1 RECONSTRUCTION

The multiple cut theory, as described in Section 2.1, allows the contour method to measure multiple stress components by executing multiple cuts. First, the contour method is applied to a part by cutting it in two, in order to measure the residual stress normal to the cut surface. Then, the contour method is applied another time one of the two halves by cutting it in two along a plane perpendicular to the first cut plane. In this way the residual stresses normal to the second cut plane and relaxed by the execution of the first cut can measured. In order to obtain the original residual stresses (before the execution of the first cut) normal to second cut plane the multiple cut theory will be applied. By simply superimposing the stresses obtained from the application of the contour method to the second cut plane (step E in Figure 2.2 at page 11) with the change of the same stress component obtained from the application of the contour method to the first cut plane (step C in Figure 2.2 at page 11), it is possible to obtain the original residual stress (before the execution of the first cut) in the second cut plane.

In the following subsection this reconstruction theory will be applied to the HSLA-100 quenched plate and to the 316L stainless steel indented disk, which applications of the contour method to the two cut plane were described in Chapter 7.

10.1.1 HSLA-100 quenched plate

In Figure 10.1 it is showed the reconstruction process of the σ_z on the second cut plane of the HSLA-100 quenched plate. Figure 10.1(a) shows the change of σ_z ob-

tained after the first step of the FE analysis, described in Section 7.1. Figure 10.1(b) (step C in Figure 2.2) shows the σ_z residual stresses on the second cut plane from Figure 7.1 after the second step of FE analysis (step B=E in Figure 2.2). This stress map is very similar to the previous map (Figure 7.7), but in the left edge the effect of the first cut is evident (the right edge shows the effect or the original removal of the test specimen from a large quenched plate).

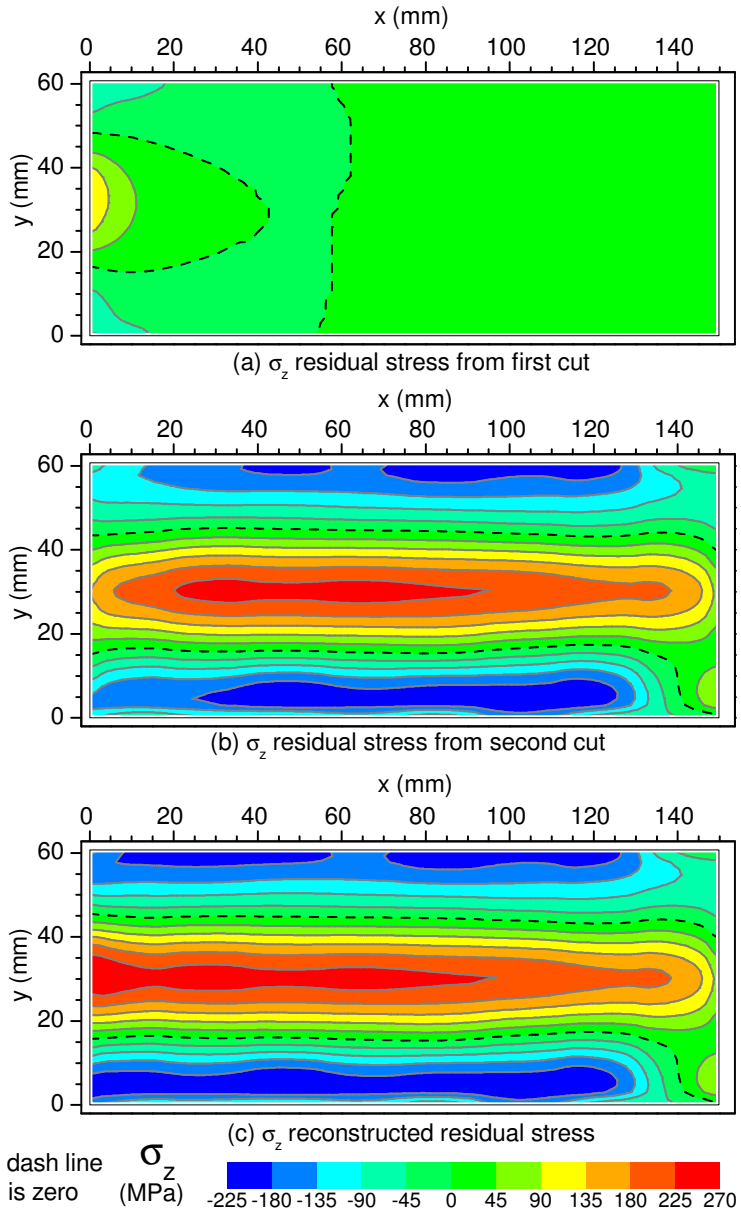

Figure 10.1 – *Residual stresses in HSLA-100 specimen measured by the multi-component contour method on the second cut plane using the result from the first cut: (a) change of σ_z after the first cut (step C in Figure 2.2); (b) σ_z after the second cut (step B=E in Figure 2.2), and (c) reconstructed original σ_z residual stresses (step A=B+C in Figure 2.2).*

By superimpose the change of the stresses in Figure 7.8(a) with the σ_z in Figure 10.1(b), the reconstructed original σ_z residual stress map is obtained on the second cut plane shown in Figure 10.1(c) (step A=B+C in Figure 2.2). Based on the left side of the results, it appears that the reconstruction has removed the effect of the first cut. By comparing the maps of σ_x in Figure 7.7 at page 53 with the one of σ_z in Figure 10.1(c), the approximately biaxial residual stress field typical of quenched plate is evident.

The reconstruction process is further illustrated by examining the stresses on the edge of the second cut where the stresses were most affected by the first cut. Figure 10.2 shows the through-thickness variation of σ_x for z =76.2 mm in Figure 7.7 at page 53 and of the σ_z stresses on the left edge of Figure 10.1, that correspond to the common line of the two cut planes (line $a-b$ in Figure 7.1). This Figure shows that the contributions of the σ_z stresses calculated in step C and E to reconstruct the original σ_z stresses are approximately of the same size in this case. Further, it is also evident that the profile of the original residual stress σ_x and σ_z are very similar, how it is expected for a quenched plate. The difference between these stresses is about less than 40 MPa along the though-thickness direction, except of the right edge (y =60.75 mm) where the difference is about 80 MPa. Because this line is the edge of the second cut, contour method stresses are expected to be less accurate there because the assumption of a flat cut is not perfect on the edge. This explains some of the difference. Also, error accumulation from the two cuts would indicate that uncertainties should be larger for reconstructed stresses.

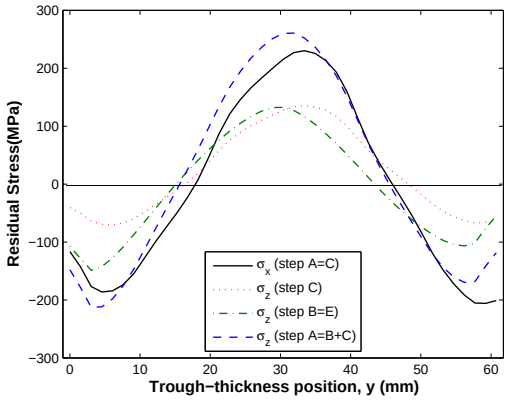

Figure 10.2 – *Through-thickness variation along the line a-b in Figure 7.1 of σ_x and σ_z residual stresses in HSLA-100 specimen.*

10.1.2 316L stainless steel disk

In Figure 10.3 it is showed the reconstruction process of the σ_θ on the second cut plane of the 316L stainless steel indented disk B. Figure 10.3(a) shows the change of σ_θ obtained after the first step of the FE analysis for the indented disk B, described in Section 7.2 (step C in Figure 2.2). Figure 10.3(b) shows the σ_θ residual stresses on the second cut plane of the indented disk B from Figure 7.16 after the second step of FE analysis (step B=E in Figure 2.2). This stress map is very different to the map of the residual hoop stress on the first cut plane for both indented disk A and B, (see Figure 7.19).

By superimpose the change of the σ_θ stresses in Figure 10.3(a) with the σ_θ in Figure 10.3(b), the reconstructed original σ_θ residual stress map is obtained on the second cut plane and showed in Figure 10.3(c) (step A=B+C in Figure 2.2). Based on the left side of the results, it appears that the reconstruction has removed the effect of the first cut. By comparing the maps of σ_θ in Figure 10.3(c) with the one in Figure 7.19 at page 62 and considering that the second cut plane has only half width of the first, it is evident that the agreement is excellent. In particular the reconstructed stress are very similar to the left half of both stress maps in Figure 7.19.

The reconstruction process is further illustrated in Figure 10.4(a) by examining the stresses along the mid-thickness line on the second cut plane. The black line represents the σ_θ hoop stresses on the second cut plane obtained from the first FE calculation, described in Subsection 7.2.2. The red line represents σ_θ hoop stresses on the second cut plane obtained from the second FE calculation, that are affected by the execution of the first cut. Then, the blue line is the original σ_θ hoop stresses (before the execution of the first cut) on the second cut plane reconstructed by simply adding the previous two curves. The major contribution to the reconstructed stresses is given by black line, i.e. the first cut FE calculation, in contrast to the case of the HSLA-100 quenched plate where the contributions to reconstruction were of the same size.

Figure 10.4(b) shows the comparison of the reconstructed hoop stresses on the second cut plane (blue line) with the σ_θ hoop stress on the first cut plane, obtained with the traditional contour method analysis on the first cut (red line), the FE prediction (black line) and the neutron diffraction measurement (green line). Since the residual stress field produced by the indentation process should be axi-symmetric, the reconstructed stresses should be close to the stress measured with the contour method on the first cut plane and also to the FE prediction and neutron diffraction measurements. The agreement of the reconstructed stresses with the FE prediction

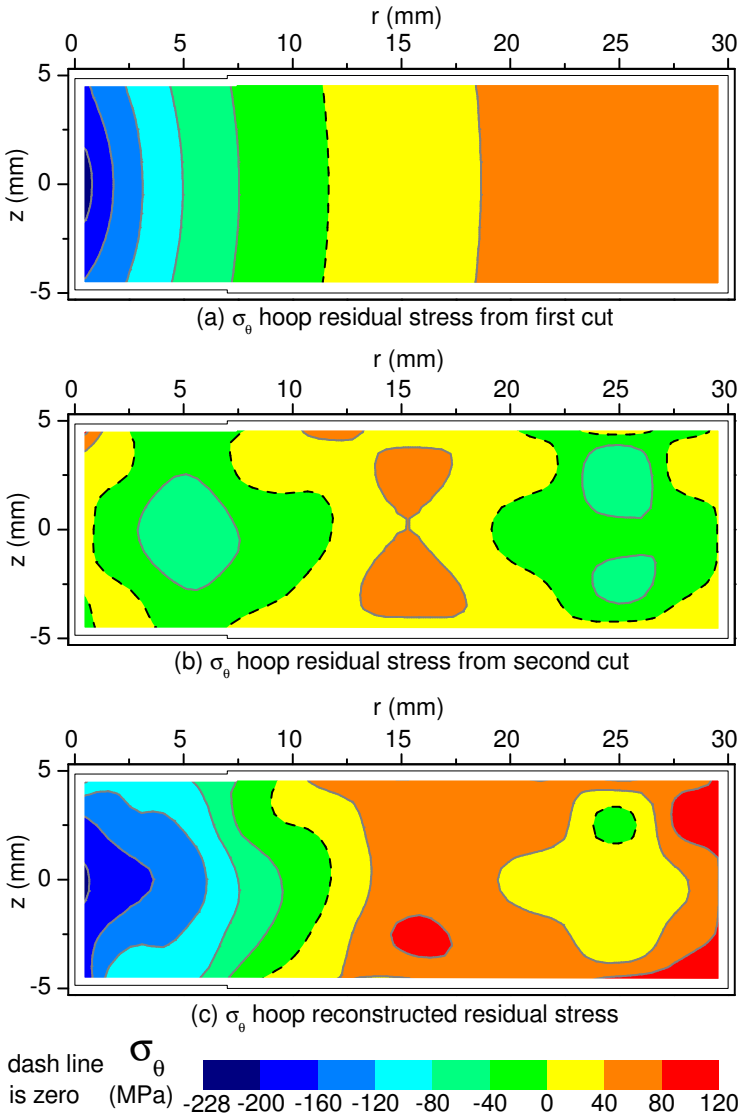

Figure 10.3 – *Residual stresses in 316L stainless steel disk measured by the multi-component contour method on the second cut plane using the result from the first cut: (a) change of σ_θ after the first cut (step C in Figure 2.2); (b) σ_θ after the second cut (step B=E in Figure 2.2), and (c) reconstructed original σ_θ residual stresses (step A=B+C in Figure 2.2).*

and the contour method result on the first cut plane is excellent with difference between these stresses less than 30 MPa.

10.2 DISCUSSION

As presented, the multiple stress components contour method measures the stress components normal to multiple cut surfaces, which is fine for many measurement applications because the normal stresses are often the largest and the main contrib-

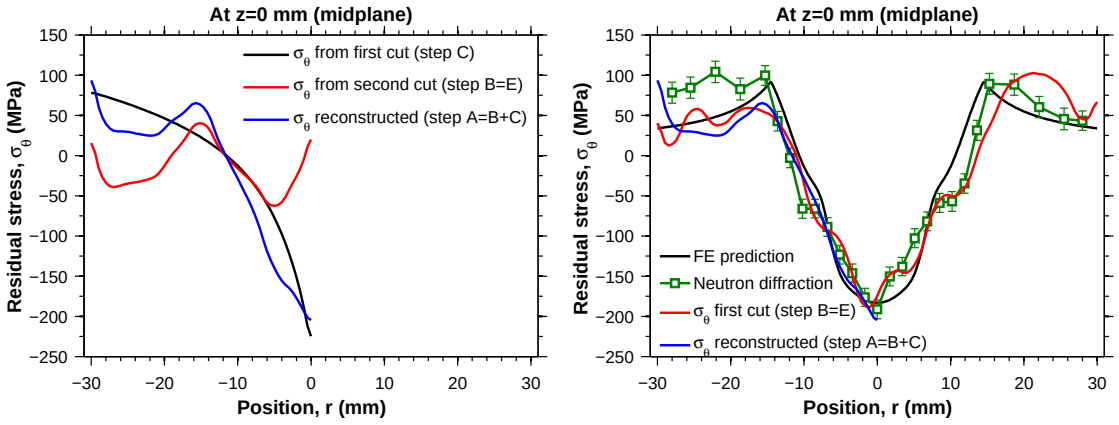

(a) (b)

Figure 10.4 – *Variation along the mid-thickness line on the second cut plane of σ_θ residual stresses in 316L stainless steel disk: (a) reconstruction process of and (b) comparison with FE prediction and contour method.*

utors to failure.

The experimental results of for the HSLA-100 quenched plate and the 316L stainless steel disk convincingly demonstrate the effectiveness of the simple process to reconstruct the original residual stresses on the plane of the second cut. For the HSLA-100 quenched plate, the difference between the original σ_x and σ_z residual stresses in the region where the first cut affected the stresses for the second but are very low after reconstruction, confirming the typical biaxial quenching stress. Some difference between the σ_x and σ_z residual stresses could be caused by different material properties along the x and z directions, in fact the yield stress is respectively 690 MPa and 685 MPa along the x and z direction. For the 316L stainless steel disk, the difference between the reconstructed stresses and the contour method result on the first cut plane are very low, less than 30 MPa, confirming the axi-symmetric stress distribution produced by the indentation process. Further, both stress profile are very close to the FE prediction and neutron diffraction measurements demonstrating the validity of the multiple component contour method and one more time of the conventional contour method.

Some of the HSLA-100 quenched plate results would have been better if a better arrangement was used to clamp the part during the EDM cutting. In both Figure 7.7 and Figure 7.8, the right of the figure corresponds to the end of the EDM cut, which started on the left of each figure. The stress gradients at the right side of those figures are a result of the part moving during the end of the cut and changing the cutting path. These experiments were performed some time ago, and the clamping arrangement in Figure 7.2 is no longer used. In that figure, the clamping direction is

the same as the cutting direction. Now, the clamping direction is the same direction as the wire axis, which is vertical in Figure 7.2. This has proven to provide better clamping and good data all the way to the end of the cut.

Chapter 11

Results: Surface Superposition

In this section it will be presented the application of the surface superposition theory to the 316L stainless steel indented disk and the aluminum 2024-T351 one, which contour method applications were described in Section 7.2 and the ESPI hole drilling application was described in Chapter 9.

11.1 RECONSTRUCTION

The surface superposition theory, as described in Section 2.3, allows the contour method to measure multiple stress components by using a different measurement technique. First, the contour method is applied to a part by cutting it in two. Then, the remaining in-plane residual stresses on the cut plane are measured by means of a technique that is able to measure the residual stresses close to the surface as the x-ray diffraction, hole drilling method, ESPI hole drilling etc. then, by simply superimposing the stresses measured with the surface technique (step B in Figure 2.2 with the change of the same stress component obtained from the application of the contour method (step C in Figure 2.2 at page 11), it is possible to obtain the other residual stress components in the cut plane.

First, an x-ray diffraction test was executed, described in Chapter 8, in order to measure in the 316L stainless steel indented disk the in-plane remaining stresses on the cut surface, after electro-polishing the surface to remove the EDM affected layer. But unfortunately the experiment was not successful because the material exhibited a big grain size and the presence of different grain size sets. So the diffracted pattern had many peaks making difficult the resolution.

Subsequently, the remaining stresses were successfully measured using ESPI hole drilling on the 316L stainless steel indented disk and on the aluminum 2024-T351 one, which experiments were described in Chapter 9.

In the following subsection this surface superposition theory will be applied to the 316L stainless steel indented disk, which applications of the contour method

were described in Chapter 7.

11.1.1 316L stainless steel disk

Figure 11.1 shows the application of the surface superposition theory to 316L stainless steel indented disk B. In detail, Figure 11.1(a) show the reconstruction process for the radial stresses and Figure 11.1(b) for the axial stresses. The red line is the change of σ_r obtained after the FE analysis for the indented disk B, described in Section 7.2 (step C in Figure 2.2). The blue line is the σ_r residual stresses on the cut plane of the indented disk B measured by ESPI hole drilling. By superimposing those stresses the reconstructed original σ_r residual stresses are obtained on the cut plane and plotted with a green line (step A=B+C in Figure 2.2). For comparison, Figure 11.1 shows also the FE prediction of the σ_r residual stress on the same location of the measurements. As described in Section 9.2 it was considered only the measurements executed at 15.000 rpm.

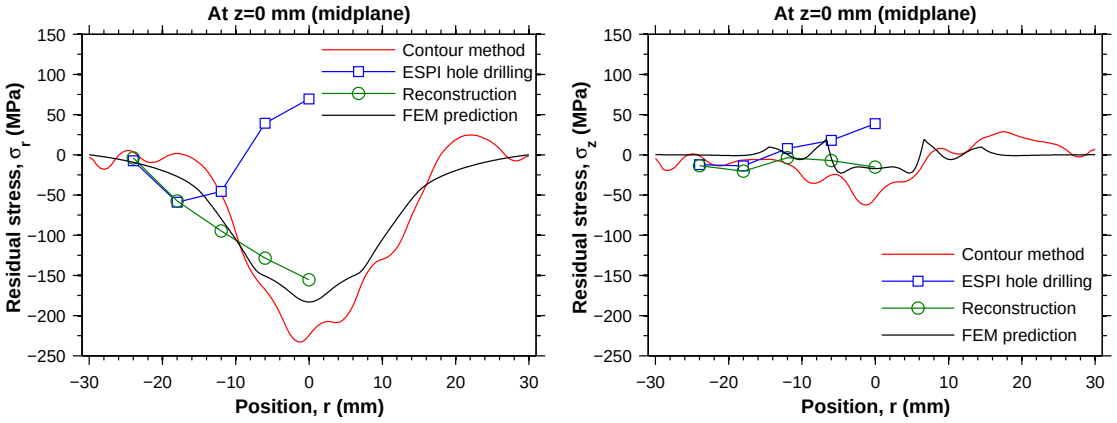

(a) (b)

Figure 11.1 – *Surface superposition theory application to the 316L stainless steel indented disk: (a) σ_r radial stress and (b) σ_z axial stress, where red line is the change of stresses after the cut (step C in Figure 2.2) measured with contour method; the blue lines the remaining stresses after the cut (step B in Figure 2.2) measured with ESPI hole drilling, and green lines the reconstructed original residual stresses (step A=B+C in Figure 2.2). The black lines are the FE prediction.*

Furthermore, Figure 11.2 shows the comparison between the reconstructed stresses, the FE prediction and the neutron diffraction results for the radial and axial stress components respectively. The agreement between the neutron diffraction, reconstructed stress and FE prediction is excellent confirming the effectiveness of the surface superposition principle.

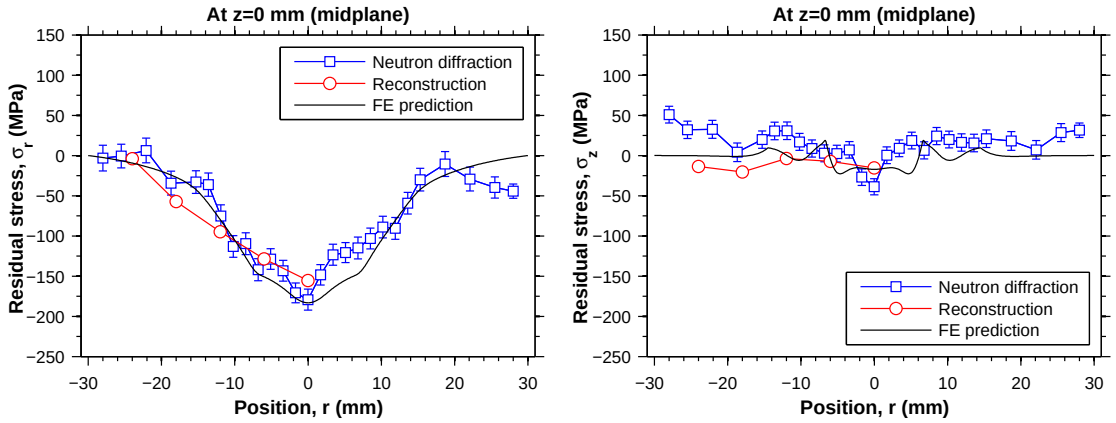

(a) (b)

Figure 11.2 – *Comparison between reconstructed stresses, FE prediction and neutron diffraction result for (a) radial and (b) axial stress components.*

11.1.2 Aluminum 2024-T351 disk

As described above the same superposition was applied to the aluminium 2024-T351 indented disk and showed in Figure 11.3. In detail, Figure 11.3(a) show the reconstruction process for the radial stresses and Figure 11.3(b) for the axial stresses. The ESPI hole drilling result, as described in Chapter 9, were executed with two different drill diameter (1/16" and 1/32").

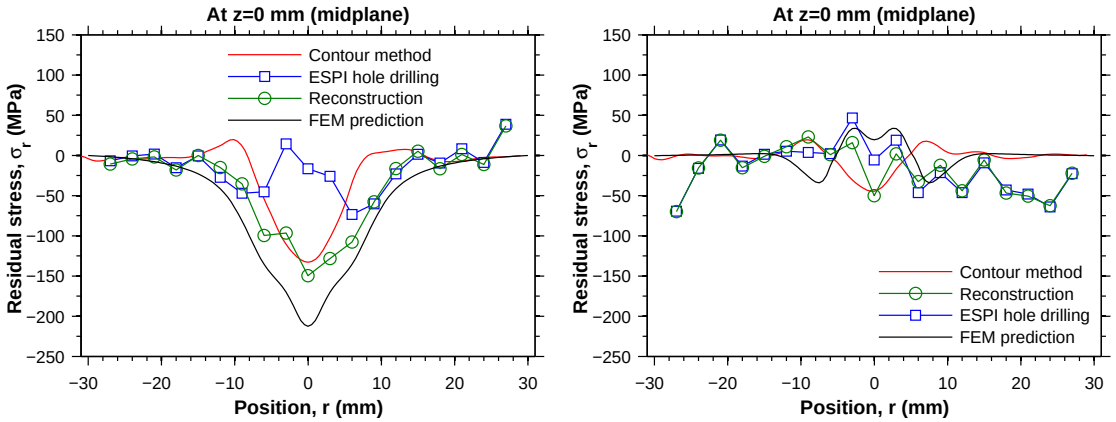

(a) (b)

Figure 11.3 – *Surface superposition theory application to the aluminum 2024-T351 indented disk: (a) σ_r radial stress and (b) σ_z axial stress, where red line is the change of stresses after the cut (step C in Figure 2.2) measured with contour method; the blue lines the remaining stresses after the cut (step B in Figure 2.2) measured with ESPI hole drilling, and green lines the reconstructed original residual stresses (step A=B+C in Figure 2.2). The black lines are the FE prediction.*

11.2 DISCUSSION

The surface superposition results obtained for the 316L stainless steel disk are reasonable and the reconstructed stresses are in good agreement with the FE prediction, particularly for the axial stress component. Even if the results were only obtained for half of the mid-thickness line, because for the other half a wrong rotational speed of the drill was used, the experimental tests validate the theory.

For the aluminium disk the results are even better. They are quite symmetric to the disk axis and they have the same trend as the FE prediction. There are bout 50 MPa of difference between the lowest reconstructed radial stress and the correspondent FE predicted stress. These difference are probably caused by some difference in the hardening behavior between the in-plane, that was modeled, and the through-thickness direction of the aluminum plate.

A specimen with higher magnitude stresses might provide a more convincing validation of this theory and should be attempted in the future. However, higher stress specimens such as welds are difficult to model. Therefore, the validation would have to come from independent measurements.

Chapter 12

Conclusion

In this thesis two new theoretical developments of the contour method that allow to measure multiple residual stress components are presented.

By making multiple cuts, the multiple cut theory measure the residual stresses normal to these cut planes. FE calculation were executed in order to validate this theory. These calculation further demonstrate the effectiveness of the theory in case of absence of shear stresses on the first cut plane. Instead in the case of presence of shear stresses on the first cut plane, the reconstructed stresses on the second cut plane are affected by errors of about 6% of the peak stress for the test case examined.

The surface superposition theory allow to measure multiple stress components by using different techniques. It has been numerically validate by means of the same FE calculation used for the multiple cut theory validation. The theory gave correct result in case of no shear stresses on the plane of the cut. Instead, in case of shear stresses on the cut plane the reconstructed stresses obtained using surface stresses measured on only one of the halves can be very different from the original residual stress. But, by averaging the surface stresses measured on the two halves of the part (step B) and then superimposing with the change of the same stress components (step C) the correct reconstructed stresses are obtained. Therefore, if shear stresses might be present on the cut plane, the surface stresses after the cut must be measured on both pieces.

In order to experimentally validate these theories, the design, fabrication of a new residual stress test specimen was presented. Two materials were chosen: a 316L stainless steel and an aluminium 2024-T351. Both materials were experimentally characterized in order to know the hardening behavior. The residual stress were introduced in the specimen by means of a controlled indentation process that allows to recreate the same residual stress field on specimens of the same dimensions and material.

In order to predict the residual stress field produced by indentation, FE simula-

tions were executed. A combined hardening model, calibrated on the experimental curve, was used for each material.

Finite element models provide a good known stress prediction for indented disks, but only if cyclic behavior of materials correctly calibrated and modeled. Cyclic data is needed and simple isotropic or kinematic models are insufficient. The residual stress produced by indentation were experimentally measured with neutron diffraction. Radial, hoop and axial residual stresses were measured along the cross section of the indented disk. The results match pretty well with the FE prediction with error less than 37 MPa.

Then the hoop residual stress along the cross section of the same disk were measured with the contour method. The stress map obtained is in excellent agreement with the previous neutron diffraction test (error $\pm$32 MPa) and the FE prediction (error $\pm$40 MPa). Furthermore, the residual stress were measured with the contour method on another 316L SS disk, indented in the same condition. Also for this disk the difference with the FE prediction is less than 40 MPa. The stress measured with the contour method on the two disk match in a excellent way with a rms error of 19 MPa, confirming the effectiveness of the indentation process to produce repeatable residual stress field on the disks. Also, for the first time, the contour method repeatability was demonstrated on nominally identical specimens and found to be within the estimated uncertainty levels for a single test. Then, one of the two disk was furthermore cut another time, and the contour method was applied again to this plane.

A contour method test was also executed on the aluminium 2024-T351 indented disk. The measured residual stress has the same trend as the FE prediction, but difference up to 75 MPa are observed, probably because of a different hardening behavior of the material in the though-thickness direction respect to the two in-plane directions.

Finite element models provide a good known stress prediction for indented disks, but only if anisotropic and cyclic behavior of materials correctly calibrated and modeled. Cyclic data is needed and simple isotropic or kinematic models are insufficient.

Further a contour method test was executed on a HSLA-100 quenched plate along two perpendicular plane, in order to validate the multiple cut theory.

Slitting tests were executed on both material disks in order to have a further experimental validation of the residual stress. The results confirmed in both cases what measured before with neutron diffraction and contour method and FE predicted, but with some very noticeable difference for the aluminum disk.

The most difficult part of validating the surface superposition theory turned

out to be the surface stress measurements with the common x-ray and hole-drilling methods.

In order to validate the surface superposition theory, the remaining residual stresses were measured on the cut plane of the 316L ss disk by means of x-ray diffraction, but unfortunately this test had not success because of the big grain size of the material.

For the same purpose, the remaining residual stresses were measured with ESPI hole drilling on the cut plane of the 316L ss and aluminium 2024-T351 disks. Some poor results for certain drilling conditions had to be discarded. The stresses measured under good drilling conditions were superimposed with the change of the same stress components obtained from the contour method tests. The reconstructed stress confirm the validity of the surface superposition theory with a difference between the reconstructed stress and the residual stress measured with the neutron diffraction and FE predicted less than 25 MPa for the 316L ss disk. For the aluminum 2024-T351 the difference with the FE predicted stress are less than 50 MPa. Hole drilling stress measurements can be very sensitive to drilling conditions, which should be validated for a specific material.

The multiple cut theory was validated by superimpose the residual stress measured with the contour method on the two normal cut planes of the HSLA-100 quenched plate and the 316L stainless steel disk. The results are in both case excellent. In the first case there is not a comparative measurement result, but an equi-biaxial residual stress state was measured as it is supposed to be for a quenched plate. For the 316L ss disk the agreement with the other experimental measurements and FE prediction is excellent with errors less than 20 MPa.

A specimen with higher magnitude transverse stresses might provide additional confidence in the theory validations, but would probably require comparison only with independent measurements since processes producing higher stresses are difficult to model.

All the experimental test executed demonstrated the validity of the multiple cut and the surface superposition theories for measuring multiple stress components for contour method. A new residual stress test specimen was presented with a good repeatability of the residual stress field produced by the indentation process. Further the contour method was validated one more time confirming its good accuracy and its great repeatability.

Appendix A

FORTRAN subroutines

A.1 INITIAL STRESSES SIGINI

In order to define the initial residual stress field, that must be self-equilibrated, the following ABAQUS User subroutine was written.

```
      SUBROUTINE sigini(SIGMA,COORDS,NTENS,NCRDS,NOEL,NPT,LAYER,KSPT,
     1    LREBAR,REBARN)
      INCLUDE 'ABA_PARAM.INC'
      DIMENSION SIGMA(NTENS),COORDS(NCRDS)
      CHARACTER*80 REBARN
C RESIDUAL STRESS DISTRIBUTIONS
C Set Beam Dimensions
      a=0.5
      L=5
      h=1
      x=COORDS(1)
      y=COORDS(2)
      A1=(L**4*(-5*a**2-a**3+L**2+a*L**2))/(L**2-a**2)**3
      B=(L**4*(-4*a-a**2+L**2))/(-L**2+a**2)**3
      C=(2*L**2*(-5*a**2-a**3+L**2+a*L**2))/(-L**2+a**2)**3
      D=(2*L**2*(4*a+a**2-L**2))/(-L**2+a**2)**3
      E=(5*a**2+a**3-L**2-a*L**2)/(-L**2+a**2)**3
      F=(-4*a-a**2+L**2)/(-L**2+a**2)**3
      SELECT CASE (1)
C Case of only normal stress in the middle section 1
      CASE (1)
      IF (abs(x)<=a) THEN
          SIGMA(1)=(6/h**2*y**2-6/h*y+1)
          SIGMA(2)=0
          SIGMA(3)=0
      ELSE IF (abs(x)>a .AND. abs(x)<=L) THEN
          SIGMA(1)=(1-5/(L-a)**4*(abs(x)-a)**4+4/(L-a)**5*(abs(x)-a)**5)
     1             *(6/h**2*y**2-6/h*y+1)
          SIGMA(2)=(60/(L-a)**4*(abs(x)-a)**2-80/(L-a)**5*(abs(x)-a)**3)
     1             *(-0.5/h**2*y**4+1/h*y**3-0.5*y**2)
```

```
          SIGMA(3)=sign(1.0,x)*(20/(L-a)**4*(abs(x)-a)**3-20/(L-a)**5*
     1              (abs(x)-a)**4)*(2/h**2*y**3-3/h*y**2+y)
      END IF
C Case of normal and shear stress in the middle section 2
      CASE (2)
      SIGMA(1)=(A1+B*x+C*x**2+D*x**3+E*x**4+F*x**5)
     1        *(6/h**2*y**2-6/h*y+1)
      SIGMA(2)=(-2*C-6*D*x-12*E*x**2-20*F*x**3)
     1        *(-0.5/h**2*y**4+1/h*y**3-0.5*y**2)
      SIGMA(3)=(-B-2*C*x-3*D*x**2-4*E*x**3-5*F*x**4)
     1        *(2/h**2*y**3-3/h*y**2+y)
      END SELECT
      RETURN
      END
```

Appendix B

MATLAB scripts

B.1 CONTOUR DATA REDUCTION

B.1.1 Spline smoothing

Here is presented the MATLAB script used to reduce the data from contour measurement and create a file with the displacement boundary condition for the subsequent FE calculation.

```
%% ELIMINATE BAD POINTS HALF1
cmm_clean

%% ELIMINATE BAD POINTS HALF2
cmm_clean

%% IMPORT THE POINT CLOUDS ALIGN AND FLIP DATA
% open LANL_A1.txt and LANL_A2.txt for the cut data
clear
[x1,y1,z1]=textread(uigetfile('*.txt','Select the data file'));
[x2,y2,z2]=textread(uigetfile('*.txt','Select the data file'));

x01=0.3; y01=0.3;                % traslation
x02=0.3; y02=0.3;
L1=60; W1=10;            % dimension 1 half
L2=0; W2=0;                  % dimension 2 half

X1=x1-x01;
Y1=y1-y01; % rotating and traslating
X2=-(x2-x02)+L1;
Y2=y2-y02;% rotating, traslating and flip

bond1={[0 L1 L1 0 0] [0 0 W1 W1 0]};
bond2={[0 L2 L2 0 0] [0 0 W2 W2 0]};
createfigure(X1, Y1, X2, Y2, bond1{1}, bond1{2});daspect([1 1 1]);
%clear x1 x2 y1 y2 x01 x02 y01 y02 theta1 theta2 L2 W2
%% Save data
dlmwrite('C1.txt',[X1 Y1 z1],'delimiter',' ','precision',10);
```

```
dlmwrite('C2.txt',[X2 Y2 z2],'delimiter',' ','precision',10);

%% INTERPOLATE THE DATA WITH DELAUNAY TRIANGULATION AND AVERAGE
% open A1.txt and A2.txt
[X1,Y1,z1]=textread(uigetfile('*.txt','Select the data file'));
[X2,Y2,z2]=textread(uigetfile('*.txt','Select the data file'));
createfigure(X1, Y1, X2, Y2, bond1{1}, bond1{2});daspect([1 1 1]);
p1=0.1;
p2=0.1;
x=[0:0.1:60]';
y=[0:0.1:10]';

x11=[0:0.1:60]';
y11=[0:0.1:10]';

[X,Y] = meshgrid(x, y);
[X11,Y11] = meshgrid(x11, y11);
Z1=griddata(X1,Y1,z1,X,Y,'nearest'); % linear
Z2=griddata(X2,Y2,z2,X,Y,'nearest'); % linear
Zt=(Z1+Z2)/2;  % average surface
clear z1 z2

%% EXTRAPOLATING DATA AT NaN LOCATIONS
% Run Linear extrapolation.m with n=55 and m=15
Zt=Linearextr(10,10,X,Y,Z1,Z2);
% n & m number of points for x-direction & y-direction linear extrapolation
%%
p=mean(Zt(:,102:502),2); %102:502
%%
for i=1:numel(Zt(1,:))
Zt(:,i)=Zt(:,i)-p;
end
%% SMOOTHING WITH B-SPLINE
% open cut2.txt
clear xn yn knotsx knotsy sp sp1 diff rms contour zf2
A=load(uigetfile('*.txt','Select the data file'));
nf=A(:,1);
xf=A(:,2);
yf=A(:,3);
zf=A(:,4);
x1=[0:L1/100:L1]';
y1=[0:W1/40:W1]';
for i=4%1:25
kx=3;
ky=3;
yn(i)=i;
xn(i)=round(L1/W1)*yn(i);
knotsx=augknt([0:L1/xn(i):L1],(kx));
knotsy=augknt([0:W1/yn(i):W1],(ky));
```

```
sp=spap2({knotsy,knotsx},[ky kx],{y, x},Zt);
sp1=fnval( sp, {y, x} );
sp2=fnval( sp, {y11, x11});
diff=sp1-Zt;
rms(i)=norm(diff)/sqrt(numel(Zt));
%end
for j=1:size(xf)
   zf2(j)=(-fnval( sp, {yf(j), xf(j)+30} ))';
end
file=num2str(i);
Heading='*Boundary';
contour(:,1)=nf; contour(:,2:3)=3; contour(:,4)=zf2;
dlmwrite(['contour' file '.txt'],Heading,'delimiter','');
dlmwrite(['contour' file '.txt'],contour,...
'delimiter',',','precision',10,'-append');
end
%% PLOT SMOOTHING DATA AND ORIGINAL DATA
figure1 = figure;
axes1 = axes('Parent',figure1,'XLim',[0 max(x)],...
    'YLim',[0 max(y)],'ZLim',[min(min(Zt)) max(max(Zt))]);
view(axes1,[-37.5 30]);
grid(axes1,'on');
hold(axes1,'all');
surf1 = surf(X,Y,Zt,'Parent',axes1);
%surf2 = surf(x1,y1,Z_smooth,'Parent',axes1);
surf3 = surf(X,Y,sp1,'Parent',axes1);
surf4 = surf(X11,Y11,sp2,'Parent',axes1);
surf5 = surf(X,Y,diff,'Parent',axes1);
daspect([1000 1000 1]);

%%
for i=1:25
k(:,:,i)=dlmread(['uncert_' int2str(i) '.txt']);
end
cut=dlmread('cut.txt');
for n=1:numel(k(:,1,1));
    for m=1:numel(cut(:,1));
        if k(n,1,1)==cut(m,1)
            k0(m,1,:)=k(n,1,:);
            k0(m,2,:)=k(n,4,:);
        end
    end
end
%%
for n=2:size(k0,3)
    RMS1(n-1,1)=norm(std(k0(:,:,n-1:n),0,3))/sqrt(numel(k0(:,:,1)));
end
for n=2:size(k0,3)-1
    RMS3(n-1,1)=norm(std(k0(:,:,n-1:n+1),0,3))/sqrt(numel(k0(:,:,1)));
```

```
    % rms CONSIDERING 3 POINTS

end
%%
knots=1:25;
knots1=2:25;
knots3=2:24;
% figure2 = figure;
% axes2 = axes('Parent',figure2,'XLim',[0 max(x)],...
%     'YLim',[0 max(y)],'ZLim',[min(min(error)) max(max(error))]);
% view(axes2,[-37.5 30]);
% grid(axes2,'on');
% hold(axes2,'all');
% surf2 = surf(X,Y,error,'Parent',axes2);
```

`mesh_indentation.inp` is the file of the FE model.

B.1.2 Linear extrapolation

This is the MATLAB function for the linear extrapolation of the contour data in the region near the edges.

```
function Zt=Linearextr(n,m,X,Y,Z1,Z2)
% LINEAR EXSTRAPOLATION OF DATA:
% X(i,j) and Y(i,j) (location of the triangulation grid
% for the two surfaces)
% Z1(i,j) and Z2(i,J) values of the two surfaces at the X(i,j)
% and Y(i,j) location
% the file gives as result the average of two surfaces
% after linear extrapolation
% change n and m to perform linear extrapolation
%(n and m are the number of points to consider in the
% linear extrapolation)

Zt1=Z1; %first surface
Zt2=Z2; %second surface

% EXTRAPOLATING DATA AT NaN LOCATIONS
xm=round(size(X,1)/2);
ym=round(size(Y,2)/2); % find the center point coordinates

% exstrapolation 1st quadrant
for j=xm:-1:1
    for i=ym:size(X,2)
        if isnan(Zt1(j,i)) & i>ym+n-1
            %Zt1(j,i)=Zt1(j,i-1);%
            Zt1(j,i)=polyval(polyfit(X(j,i-n:i-1),Zt1(j,i-n:i-1),1),X(j,i));
        else
            if j>1
```

```
                if isnan(Zt1(j-1,i)) & j<xm-n+1
                    continue
                end
            end
        end
    end
end
% exstrapolation 2nd quadrant
for j=xm:-1:1
    for i=ym:-1:1
        if isnan(Zt1(j,i)) & i<ym-n+1
            %Zt1(j,i)=Zt1(j,i+1);
            Zt1(j,i)=polyval(polyfit(X(j,i+1:i+n),Zt1(j,i+1:i+n),1),X(j,i));
        else
            if j>1
                if isnan(Zt1(j-1,i)) & j<xm-n+1
                    continue
                end
            end
        end
    end
end
% exstrapolation 3rd quadrant
for j=xm:size(X,1)
    for i=ym:-1:1
        if isnan(Zt1(j,i)) & i<ym-n+1
            %Zt1(j,i)=Zt1(j,i+1);
            Zt1(j,i)=polyval(polyfit(X(j,i+1:i+n),Zt1(j,i+1:i+n),1),X(j,i));
        else
            if j<size(X,1)
                if isnan(Zt1(j+1,i)) & j>xm+n-1
                    continue
                end
            end
        end
    end
end
% exstrapolation 4th quadrant
for j=xm:size(X,1)
    for i=ym:size(X,2)
         if isnan(Zt1(j,i)) & i>ym+n-1
             %Zt1(j,i)=Zt1(j,i-1);
             Zt1(j,i)=polyval(polyfit(X(j,i-n:i-1),Zt1(j,i-n:i-1),1),X(j,i));
        else
            if j<size(X,1)
                if isnan(Zt1(j+1,i)) & j>xm+n-1
                    continue
                end
            end
```

```
        end
    end
end
% 2nd surface
% exstrapolation 1st quadrant
for j=xm:-1:1
    for i=ym:size(X,2)
        if isnan(Zt2(j,i)) & i>ym+n-1
            %Zt2(j,i)=Zt2(j,i-1);
            Zt2(j,i)=polyval(polyfit(X(j,i-n:i-1),Zt2(j,i-n:i-1),1),X(j,i));
        else
            if j>1
                if isnan(Zt2(j-1,i)) & j<xm-n+1
                    continue
                end
            end
        end
    end
end
% exstrapolation 2nd quadrant
for j=xm:-1:1
    for i=ym:-1:1
        if isnan(Zt2(j,i)) & i<ym-n+1
            %Zt2(j,i)=Zt2(j,i+1);
            Zt2(j,i)=polyval(polyfit(X(j,i+1:i+n),Zt2(j,i+1:i+n),1),X(j,i));
        else
            if j>1
                if isnan(Zt2(j-1,i)) & j<xm-n+1
                    continue
                end
            end
        end
    end
end
% exstrapolation 3rd quadrant
for j=xm:size(X,1)
    for i=ym:-1:1
        if isnan(Zt2(j,i)) & i<ym-n+1
            %Zt2(j,i)=Zt2(j,i+1);
            Zt2(j,i)=polyval(polyfit(X(j,i+1:i+n),Zt2(j,i+1:i+n),1),X(j,i));
        else
            if j<size(X,1)
                if isnan(Zt2(j+1,i)) & j>xm+n-1
                    continue
                end
            end
        end
    end
end
```

```
% exstrapolation 4th quadrant
for j=xm:size(X,1)
    for i=ym:size(X,2)
         if isnan(Zt2(j,i)) & i>ym+n-1
             %Zt2(j,i)=Zt2(j,i-1);
             Zt2(j,i)=polyval(polyfit(X(j,i-n:i-1),Zt2(j,i-n:i-1),1),X(j,i));
        else
            if j<size(X,1)
                if isnan(Zt2(j+1,i)) & j>xm+n-1
                    continue
                end
            end
        end
    end
end
%
%
%
% Extrapolation in y-direction 1st surface
% exstrapolation 1st quadrant
for j=xm:-1:1
    for i=ym:size(X,2)
        if j>1
                if isnan(Zt1(j-1,i)) & j<xm-m+1
                    Zt1(j-1,i)=polyval(polyfit(Y(j+m-1:-1:j,i),...
                    Zt1(j+m-1:-1:j,i),1),Y(j-1,i));
                end
        end
    end
end
% exstrapolation 2nd quadrant
for j=xm:-1:1
    for i=ym:-1:1
        if j>1
                if isnan(Zt1(j-1,i)) & j<xm-m+1
                    Zt1(j-1,i)=polyval(polyfit(Y(j+m-1:-1:j,i),...
                    Zt1(j+m-1:-1:j,i),1),Y(j-1,i));
                end
        end
    end
end
% exstrapolation 3rd quadrant
for j=xm:size(X,1)
    for i=ym:-1:1
       if j<size(X,1)
                if isnan(Zt1(j+1,i)) & j>xm+m-1
                    Zt1(j+1,i)=polyval(polyfit(Y(j-m+1:j,i),...
                    Zt1(j-m+1:j,i),1),Y(j+1,i));
                end
```

```
        end
    end
end
% exstrapolation 4th quadrant
for j=xm:size(X,1)
    for i=ym:size(X,2)
         if j<size(X,1)
                if isnan(Zt1(j+1,i)) & j>xm+m-1
                    Zt1(j+1,i)=polyval(polyfit(Y(j-m+1:j,i),...
                    Zt1(j-m+1:j,i),1),Y(j+1,i));
                end
        end
    end
end
% exstrapolation 1st quadrant 2bd surface
for j=xm:-1:1
    for i=ym:size(X,2)
        if j>1
                if isnan(Zt2(j-1,i)) & j<xm-m+1
                    Zt2(j-1,i)=polyval(polyfit(Y(j+m-1:-1:j,i),...
                    Zt2(j+m-1:-1:j,i),1),Y(j-1,i));
                end
        end
    end
end
% exstrapolation 2nd quadrant
for j=xm:-1:1
    for i=ym:-1:1
        if j>1
                if isnan(Zt2(j-1,i)) & j<xm-m+1
                    Zt2(j-1,i)=polyval(polyfit(Y(j+m-1:-1:j,i),...
                    Zt2(j+m-1:-1:j,i),1),Y(j-1,i));
                end
        end
    end
end
% exstrapolation 3rd quadrant
for j=xm:size(X,1)
    for i=ym:-1:1
        if j<size(X,1)
                if isnan(Zt2(j+1,i)) & j>xm+m-1
                    Zt2(j+1,i)=polyval(polyfit(Y(j-m+1:j,i),...
                    Zt2(j-m+1:j,i),1),Y(j+1,i));
                end
        end
    end
end
% exstrapolation 4th quadrant
for j=xm:size(X,1)
```

```
    for i=ym:size(X,2)
         if j<size(X,1)
                if isnan(Zt2(j+1,i)) & j>xm+m-1
                    Zt2(j+1,i)=polyval(polyfit(Y(j-m+1:j,i),...
                    Zt2(j-m+1:j,i),1),Y(j+1,i));
                end
        end
    end
end
%
Zt=(Zt1+Zt2)/2;  % average surface
```

Appendix C

ABAQUS scripts

Sample files for the finite element analysis are presented here to help others that may want to use this procedure. The sample files are presented in sufficient detail to allow understanding of the procedure. To conserve space some of the details are omitted, such as the node and element definitions.

C.1 INDENTATION PREDICTION

C.1.1 316L stainless steel disk

Here is presented the ABAQUS input file used to simulate the indentation of the 316L stainless steel disk.

```
*Heading
*Preprint, echo=NO, model=NO, history=no, contact=NO
**
*INCLUDE,INPUT=mesh_indentation.inp
**
*Material, name=SS316L
*Elastic
193000., 0.3
*Plastic, hardening=COMBINED, data type=parameters
183.84,28722,230.71
*cyclic hardening, parameters
183.84, 100, 12
*Material, name=TSA2
*Elastic
204000, 0.3
**
*Surface Interaction, name=no_friction
1.,
*Friction
0.,
*Surface Behavior, pressure-overclosure=HARD
**
```

```
*Boundary
symmetry_axis, YASYMM
symmetry_plane, YSYMM
**
*Contact Pair,interaction=no_friction,small sliding,type=SURFACE TO SURFACE
disk_surface, indenter_surface
** ----------------------------------------------------------------
**
** STEP: Load
**
*Step, name=Load, nlgeom=YES
*Static
1, 535, 0.5, 50
**
*Boundary
head, 2, 2, -0.0867
** 0.107
*Restart, write, frequency=0
**
*Output, field
*Node Output
U,RF,CF
*Element Output
S,E,NE,LE,EE,PE,ER, PEEQ
*El print, pos=averaged at nodes, elset=cut
S11,S22, S33, S12, INV3, EE11, EE22, EE33, Temp
*Output, history
*Node Output, nset=head
RF2, U2
*Element Output, elset=center
ER
*Element Output, elset=concentration
ER
*Node Output, nset=disk_surface
RF2, U2
**contact Output, nset=disk_surface
**CFN2
**
*End Step
** ----------------------------------------------------------------
**
** STEP: unload
**
*Step, name=unload, nlgeom=YES
*Static
1, 510., 0.5, 50
**
*Boundary
head, 2, 2, 0
```

```
**
*End Step
```

`mesh_indentation.inp` is the file of the FE model.

C.1.2 Aluminium 2024-T351 disk

Here is presented the ABAQUS input file used to simulate the indentation of the aluminium 2024-T351 stainless steel disk.

```
*Heading
*Preprint, echo=NO, model=NO, history=NO, contact=NO
**
*INCLUDE,INPUT=mesh_indentation.inp
**
*Material, name=SS316L
*Elastic
73200, 0.33
*Plastic, hardening=combined, data type=parameters
219.90, 67145, 411.99
*cyclic hardening, parameters
219.90, 200, 7
*Material, name=TSA2
*Elastic
204000, 0.3
**
*Surface Interaction, name=no_friction
1.,
*Friction
0.,
*Surface Behavior, pressure-overclosure=HARD
**
*Boundary
symmetry_axis, YASYMM
symmetry_plane, YSYMM
**
*Contact Pair,interaction=no_friction,small sliding,type=SURFACE TO SURFACE
disk_surface, indenter_surface
** ----------------------------------------------------------------
**
** STEP: Load
**
*Step, name=Load, nlgeom=YES
*Static
1, 663, 0.5, 50
**
*Boundary
head, 2, 2, -0.11
**
```

```
*Restart, write, frequency=0
**
*Output, field
*Node Output
U,RF,CF
*Element Output
S,E,NE,LE,EE,PE,ER
*El print, pos=averaged at nodes, elset=cut
S11,S22, S33, S12, S13, S23, EE11, EE22, EE33
*Output, history
*Node Output, nset=head
RF2, U2
*Node Output, nset=disk_surface
CF2,RF2, U2
*Element Output, elset=center
PEEQ,ER
*Element Output, elset=concentration
PEEQ,ER
**contact Output, nset=disk_surface
**CFN2
**
*End Step
** ----------------------------------------------------------------
**
** STEP: unload
**
*Step, name=unload, nlgeom=YES
*Static
1, 563., 0.5, 50
**
*Boundary
head, 2, 2, 0
**
*End Step
```

`mesh_indentation.inp` is the file of the FE model.

C.2 HSLA-100 QUENCHED PLATE

Here is presented the ABAQUS input file used for the application of the multiple component contour method from multiple cuts to the HSLA-100 quenched plate.

```
*HEADING
HSLA-100 plate
**
*PREPRINT,MODEL=NO,ECHO=NO,HISTORY=NO
** Import mesh:
*INCLUDE,INPUT=HSLAmesh.inp
```

```
** HSLAmesh.inp is the input file with node and element definitions
**
*SOLID SECTION, ELSET=BLOCK, MATERIAL=HSLA100
          1.,
**
*MATERIAL, NAME=HSLA100
**
*ELASTIC, TYPE=ISO
197000, 0.29
**
*STEP, NAME=First_Cut
*STATIC
**
*BOUNDARY, OP=NEW
corn1,1,2,         0.
corn2, 2,,          0.
*INCLUDE,INPUT=contour1.txt
** These are the displacement applied
** on the nodes of the first cut surface
**
*OUTPUT,FIELD
*ELEMENT OUTPUT
S
*NODE OUTPUT
U
*EL PRINT, POS=AVERAGED AT NODES, ELSET=cut1
S11,S22, S33, S12, S13, S23
*EL PRINT, POS=AVERAGED AT NODES, ELSET=cut2
S11,S22, S33, S12, S13, S23
*EL PRINT, POS=AVERAGED AT NODES, ELSET=ligament
S11,S22, S33, S12, S13, S23
*end step
**
*STEP, NAME=Second_cut
*STATIC
*MODEL CHANGE, REMOVE
half
** Command for removing half of the model
*BOUNDARY, OP=NEW
corn3,2,3,         0.
corn4, 2,,          0.
*INCLUDE,INPUT=contour2.txt
** These are the displacement applied
** on the nodes of the second cut surface
**
*END STEP
**
```

`HSLAmesh.inp` is the file of the FE model. `contour1.txt` is the contour in term of

boundary conditions for the first cut plane. `contour2.txt` is the contour in term of boundary conditions for the second cut plane.

C.3 316L SS DISK

This is the ABAQUS input file used for the uncertainty analysis of the contour method result for the 316L stainless steel indented disk.

```
*HEADING
Intended 316L disk
*PREPRINT,MODEL=NO,ECHO=NO,HISTORY=NO
**
** Import mesh:
*INCLUDE,INPUT=316Lmesh.inp
**
*SOLID SECTION, ELSET=BLOCK, MATERIAL=SS316L
1.,
**
**
*MATERIAL, NAME=SS316L
**
*ELASTIC, TYPE=ISO
193000,0.29
**
*BOUNDARY
corn1,1,2,0.
corn2,1, ,0.
**
*STEP, perturbation, name=Forcing_Back
*STATIC
**
**
*load case, name=Uncert1
*INCLUDE,INPUT=contour1.txt
*end load case
**
*load case, name=Uncert2
*INCLUDE,INPUT=contour2.txt
*end load case
**

Put all the needed load case

*load case, name=UncertN
*INCLUDE,INPUT=contourN.txt
*end load case
**
**
```

```
*OUTPUT,FIELD
*ELEMENT OUTPUT
S
*NODE OUTPUT
U
**
**NODE PRINT, Nset=cut
**Coord
*EL PRINT, POS=AVERAGED AT NODES, ELSET=cut
S11,S22, S33, S12, S13, S23
**
*end step
```

`316Lmesh.inp` is the file of the FE model. `contour1.txt`, `contour2.txt` and `contourN.txt` are the contours in term of boundary conditions for the cut plane obtained with a increasing number of knots point for the spline fitting.

Bibliography

[1] Prime, M. B., "Cross-Sectional Mapping of Residual Stresses by Measuring the Surface Contour After a Cut," *Journal of Engineering Materials and Technology*, vol. 123, no. 2, pp. 162–168, April 2001.

[2] Prime, M. B., Sebring, R. J., Edwards, J. M., Hughes, D. J., and Webster, P. J., "Laser Surface-Contouring and Spline Data-smoothing for Residual Stress Measurement," *Experimental Mechanics*, vol. 44, no. 2, pp. 176–184, April 2004.

[3] Prime, M. B., "A System and Method for Measuring Residual Stress," U.S. Patent 6 470 756, October 29, 2002.

[4] The Contour Method for Measuring Residual Stress. Los Alamos National Laboratory. Los Alamos, New Mexico 87545, USA. [Online]. Available: http://www.lanl.gov/contour/

[5] Lu, J., James, M., , and Roy, G., *Handbook of Measurement of Residual Stresses*. Lilburn, Georgia, USA: The Fairmont Press, Inc., 1996.

[6] Krawitz, A. D. and Winholtz, R. A., "Use of Position-Dependent Stress-Free Standards for Diffraction Stress Measurements," *Materials Science & Engineering A*, vol. 185, no. 1–2, pp. 123–130, September 1994.

[7] Withers, P. J. and Bhadeshia, H. K. D. H., "Overview — Residual Stress Part I — Measurement Techniques," *Materials Science and Technology*, vol. 17, no. 2, pp. 335–365, 2001.

[8] Smith, D. J., Bouchard, P. J., and George, D., "Measurement and Prediction of Residual Stresses in Thick-section Steel Welds," *Journal of Strain Analysis for Engineering Design*, vol. 35, no. 4, pp. 287–305, 2000.

[9] Prime, M. B., Newborn, M. A., and Balog, J. A., "Quenching and Cold-work Residual Stresses in Aluminum Hand Forging: Contour Method Measurement and FEM Prediction," *Materials Science Forum*, vol. 426–432, pp. 435–440, 2003.

[10] DeWald, A. T. and Hill, M. R., "Multi-Axial Contour Method for Mapping Residual Stresses in Continuously Processed Bodies," *Experimental Mechanics*, vol. 46, no. 4, pp. 473–490, August 2006.

[11] Pagliaro, P., Prime, M. B., and Zuccarello, B., "Multi Stress Components From Multiple Cuts For the Contour Method," in *Proceedings of the XXXV*

AIAS Conference. Universitá Politecnica delle Marche, Ancona, Italy: Associazione Italiana per l'Analisi delle Sollecitazioni, September 13–16 2006. [Online]. Available: http://pcm.dmti.unifi.it/aias/AIAS2006/CD%20AIAS%202006/lavori/Pagliaro%20_paper13-6.pdf

[12] Mahmoudi, A. H., Stefanescu, D., Hossain, S., Truman, C. E., Smith, D. J., and Withers, P. J., "Measurement and Prediction of the Residual Stress Field Generated by Side-Punching," *Journal of Engineering Materials and Technology*, vol. 128, pp. 451–459, July 2006.

[13] Bueckner, H. F., "The Propagation of Cracks and the Energy of Elastic Deformation," *Transaction ASME*, vol. 80, pp. 1225–1230, 1958.

[14] Timoshenko, S. P. and Goodier, J. N., *Theory of Elasticity*, 3rd ed. New York: McGraw-Hill, 1970.

[15] Lu, J., James, M., and Roy, G., *Handbook of Measurement of Residual Stresses*. Lilburn, Georgia, USA: The Fairmont Press, Inc., 1996.

[16] Flaman, M. T. and Herring, J. A., "Comparison of Four Hole-Producing Techniques for the Center-Hole Residual Stress Measurement Method." *Experimental Techniques*, vol. 9, no. 8, pp. 30–32, 1985.

[17] Nobre, J. P., Kornmeier, M., Dias, A. M., and Scholtes, B., "Use of the Hole-Drilling Method for Measuring Residual Stresses in Highly Stressed Shot-Peened Surfaces," *Experimental Mechanics*, vol. 40, no. 3, pp. 289–297, 2000.

[18] Sommer, C. and Sommer, S., *Wire EDM Handbook*. Houston, TX: Advance Publishing,Inc., 1997.

[19] Cheng, W., Finnie, I., Gremaud, M., and Prime, M. B., "Measurement of Near Surface Residual Stresses using Electric Discharge Wire Machining," *Journal of Engineering Materials and Technology, Transactions of the ASME*, vol. 116, no. 1, pp. 1–7, 1994.

[20] Prime, M. B., Sebring, R. J., Edwards, J. M., Baumann, J. A., and Lederich, R. J., "Contour-Method Determination of Parent-Part Residual Stresses Using a Partially Relaxed FSW Test Specimen," in *Proceedings of the 2004 SEM Annual X International Congress & Exposition on Experimental and Applied Mechanics*. Costa Mesa, California, USA: Society for Experimental Mechanics, June 7–10 2004, CD-ROM paper 144.

[21] Prime, M. B., Gnäupel-Herold, T., Baumann, J. A., Lederich, R. J., Bowden, D. M., and Sebring, R. J., "Residual Stress Measurements in a Thick, Dissimilar Aluminum Alloy Friction Stir Weld," *Acta Materialia*, vol. 54, no. 15, pp. 4013–4021, 2006.

[22] Kelleher, J., Prime, M. B., Buttle, D., Mummery, P. M., Webster, P. J., Shackleton, J., and Withers, P. J., "The Measurement of Residual Stress in Railway Rails by Diffraction and Other Methods," *Journal of Neutron Research*, vol. 11, no. 4, pp. 187–193, 2003.

[23] Rangaswamy, P., Griffith, M. L., Prime, M. B., Holden, T. M., Rogge, R. B., Edwards, J. M., and Sebring, R. J., "Residual Stresses in LENS Components Using Neutron Diffraction and Contour Method," *Materials Science and Engineering A*, vol. 399, no. 1–2, pp. 72–83, 2005.

[24] Prime, M. B., "Residual Stresses Measured in Quenched HSLA–100 Steel Plate," in *Proceedings of the 2005 SEM Annual Conference and Exposition on Experimental and Applied Mechanics*. Portland, OR, USA: Society for Experimental Mechanics, June 7–9 2005, CD-ROM paper 52.

[25] Martineau, R. L., Prime, M. B., and Duffey, T., "Penetration of HSLA-100 Steel with Tungsten Carbide Spheres at Striking Velocities between 0.8 and 2.5 km/s," *International Journal of Impact Engineering*, vol. 30, no. 5, pp. 505–520, 2004.

[26] *ABAQUS User's Manual, Version 6.6*, ABAQUS Inc., Pawtucket, RI, 2006.

[27] Bleys, P., Kruth, J.-P., Lauwers, B., Schacht, B., Balasubramanian, V., Froyen, L., and Humbeeck, J. V., "Surface and Sub-Surface Quality of Steel after EDM," *Advanced Engineering Materials*, vol. 8, no. 1–2, pp. 15–25, August 2006.

[28] Lemaitre, J. and Chaboche, J.-L., *Mechanics of solid materials*. Cambridge: Cambridge University Press, 1990.

[29] Choteau, M., Quaegebeur, P., and Degallaix, S., "Modelling of Bauschinger Effect by Various Constitutive Relations Derived from Thermodynamical Formulation," *Mechanics of Materials*, vol. 37, pp. 1143–1152, 2005.

[30] Prime, M. B., "Residual Stress Measurement by Successive Extension of a Slot: The Crack Compliance Method," *Applied Mechanics Reviews*, vol. 52, no. 2, pp. 75–96, 1999.

[31] Schajer, G. S. and Prime, M. B., "Use of Inverse Solutions for Residual Stress Measurements," *Journal of Engineering Materials and Technology, Transactions of the ASME*, vol. 129, no. 3, pp. 375–382, 2006.

[32] *ABAQUS Theory Manual, Version 6.6*, ABAQUS Inc., Pawtucket, RI, 2006.

[33] Von Dreele, R. B., "Quantitative Texture Analysis by Rietveld Refinement," *Journal of Applied Crystallography*, vol. 30, pp. 517–525, 1997.

[34] Larson, A. C. and Von Dreele, R. B., "General Structure Analysis System (GSAS)," Los Alamos National Laboratory, Los Alamos, NM, Tech. Rep. Los Alamos Report No. LAUR 8-748, 1986.

[35] Cheng, W. and Finnie, I., "Method for Measurement of Axisymmetric Axial Residual Stresses in Circumferentially Welded Thin-walled Cylinders," *Journal of Engineering Materials and Technology, Transactions of the ASME*, vol. 107, no. 3, pp. 181–185, 1985.

[36] Schajer, G. S., "Application of finite element calculations to residual stress measurements." *Journal of Engineering Materials and Technology, Transactions of the ASME*, vol. 103, no. 2, pp. 157–163, 1981.

[37] Prime, M. B., "Measuring Residual Stress and the Resulting Stress Intensity Factor in Compact Tension Specimens," *Fatigue and Fracture of Engineering Materials and Structures*, vol. 22, no. 3, pp. 195–204, 1999.

[38] Prime, M. B. and Hill, M. R., "Uncertainty, Model Error, and Order Selection for Series-Expanded, Residual-Stress Inverse Solutions," *Journal of Engineering Materials and Technology, Transactions of the ASME*, vol. 128, no. 2, pp. 175–185, 2006.

[39] Prime, M. B. and Hill, M. R., "Residual stress, stress relief, and inhomogeneity in aluminum plate," *Scripta Materialia*, vol. 46, no. 1, pp. 77–82, January 4 2002.

[40] Lee, M. J. and Hill, M. R., "Effect of Strain Gage Length When Determining Residual Stress by Slitting," *Journal of Engineering Materials and Technology, Transactions of the ASME*, vol. 129, no. 1, pp. 143–150, 2007.

[41] Rankin, J. E. and Hill, M. R., "Measurement of Thickness-average Residual Stress Near the Edge of a Thin Laser Peened Strip," *Journal of Engineering Materials and Technology, Transactions of the ASME*, vol. 125, no. 3, pp. 283–293, 2003.

[42] Nowell, D., "Strain Changes Caused by Finite Width Slots, with Particular Reference to Residual Stress Measurement," *Journal of Strain Analysis for Engineering Design*, vol. 34, no. 4, pp. 285–294, 1999.

[43] Prime, M. B. and Pagliaro, P., "Uncertainty, Model Error, and Improving the Accuracy of Residual Stress Inverse Solutions," in *Proceedings of the 2006 SEM Annual Conference and Exposition on Experimental and Applied Mechanics*. Saint Louis, Missouri USA: Society for Experimental Mechanics, June 4–7 2006, CD-ROM paper 176.

[44] Talyscan 250. Taylor Hobson Precision. 2 New Star Road, Leicester, Le4 9JQ, England. [Online]. Available: http://www.taylor-hobson.com/pdf/uk/TSCAN250.PDF

[45] Cullity, B. D., *Elements of X-ray Diffraction*. Massachusetts: Addison Wesley, 1978.

[46] Barret, C. S. and Massalski, T. B., *Structure of Metals*. New York: McGraw Hill, 1966.

[47] Klug, H. P. and Alexander, L. E., *X-ray Diffraction Procedures*. New York: Wiley, 1967.

[48] Bacon, G. E., *Neutron Diffraction*. Oxford, England: Clarendon Press, 1975.

[49] Noyan, I. C. and Cohen, J. B., *Residual Stress, Measurement by Diffraction and Interpretation.* New York: Springer–Verlag, 1987.

[50] for Experimental Mechanics, S., *Handbook of Measurement of Residual Stresses*, Lu, J., Ed. Lilburn, GA: The fairmont Press, Inc., 1996.

[51] Krause, H. and Haase, A., *X-Ray Diffraction System PTS for Powder, Texture and Stress Analysis.* Oberursel: DGM Informationsgesellschaft Verlag, 1986, ch. Experimental Techniques of Texture Analysis, pp. 405–408.

[52] *TEC Model 1600 x-ray stress analysis system with SaraTEC^{TM} Windows^{TM}*, software v.1.64 ed., Technology for Energy Corporation, 10737 Lexington Dive, Knoxville, TN 37932. [Online]. Available: www.tecstress.com

[53] Wiesner, D. J. and Pappas, N. R., "Residual Stress Analysis 2.0," Labview based software, ORNL, August 2006.

[54] Mathar, J., "Determination of Initial Stresses by Measuring the Deformations Around Drilled Holes," *Transactions of the ASME, Iron Steel*, vol. 56, no. 2, pp. 249–254, 1934.

[55] "Standard Test for Determining Residal Stresses by the Hole Drilling Strain-Gage Method," American Society for Testing and Materials, West Conshohocken, PA, Tech. Rep. ASTM E837-01, 2001.

[56] Antonov, A. A., "Inspecting the Level of Residual Stresses in Welded Joints by Laser Interferometry," *Welding Production (English translation of Svarochnoe Proizvodstvo)*, vol. 30, no. 9, pp. 29–31, 1983.

[57] McDonach, A., McKelvie, J., MacKenzie, P., and Walker, C. A., "Improved Moiré Interferometry and Applications in Fracture Mechanics, Residual Stress and Damaged Composites," *Experimental Techniques*, vol. 7, no. 6, pp. 20–24, 1983.

[58] Makino, A. and Nelson, D., "Residual-stress Determination by Single-axis Holographic Interferometry and Hole Drilling – Part I: Theory," *Experimental Mechanics*, vol. 34, no. 1, pp. 66–78, 1994.

[59] Steinzig, M., Hayman, G., and Prime, M., "Verification of a Technique for Holographic Residual Stress Measurement," vol. PVP-429, 2001, pp. 65–70.

[60] Diaz, F. V., Kaufmann, G. H., and Galizzi, G. E., "Determination of Residual Stresses Using Hole Drilling and Digital Speckle Pattern Interferometry with Automated Data Analysis," *Optics and Lasers in Engineering*, vol. 33, no. 1, pp. 39–48, 2000.

[61] Steinzig, M. and Ponslet, E., "Residual Stress Measurement using the Hole Drilling Method and Laser Speckle Interferometry: Part I," *Experimental Techniques*, vol. 27, no. 3, pp. 43–46, 2003.

[62] Ponslet, E. and Steinzig, M., "Residual Stress Measurement using the Hole Drilling Method and Laser Speckle Interferometry: Part II: Analysis Technique," *Experimental Techniques*, vol. 27, no. 4, pp. 17–21, 2003.

[63] Ponslet, E. and Steinzig, M., "Residual Stress Measurement using the Hole Drilling Method and Laser Speckle Interferometry: Part III: Analysis Technique," *Experimental Techniques*, vol. 27, no. 5, pp. 45–48, 2003.

[64] Steinzig, M. and Takahashi, T., "Residual Stress Measurement using the Hole Drilling Method and Laser Speckle Interferometry: Part IV: Measurement Accuracy," *Experimental Techniques*, vol. 27, no. 6, pp. 59–63, 2003.

[65] Ghiglia, D. C. and Pritt, M. D., *Two-dimensional Phase Unwrapping: Theory, Algorithms, and Software*. New York: John Wiley & Sons Inc., 1998.

[66] Butters, J. N. and Leendertz, J. A., "Speckle Pattern and Holographic Techniques in Engineering Metrology," *Optics and Laser Technology*, vol. 3, no. 1, pp. 26–30, 1971.

[67] Macovski, A., Ramsey, S. D., and Schaefer, L. F., "Time-lapse Interferometry and Contouring Using Television Systems," *Applied Optics*, vol. 10, no. 12, pp. 2722–2727, 1971.

[68] Jones, R. and Wykes, C., *Holographic and Speckle Interferometry*, 2nd ed. Cambridge: Cambridge University Press, 1989.

[69] Cloud, G., *Optical Methods of Engineering Analysis*. Cambridge: Cambridge University Press, 1995.

[70] Hytec Incorporated. 110 Eastgate Drive, Los Alamos, New Mexico 87544, USA. [Online]. Available: http://hytecinc.com/

[71] Schajer, G. S., "Measurement of non-uniform residual stresses using the hole-drilling method. part i. stress calculation procedures," *Journal of Engineering Materials and Technology, Transactions of the ASME*, vol. 110, no. 4, pp. 338–343, 1988.

[72] Schajer, G. S., "Measurement of non-uniform residual stresses using the hole-drilling method. part ii. practical application of the integral method," *Journal of Engineering Materials and Technology, Transactions of the ASME*, vol. 110, no. 4, pp. 344–349, 1988.